UNIVERSITY OF MODENA AND REGGIO EMILIA

International Doctoral Program

in Clinical and Experimental Medicine (CEM)

Curriculum: Medicinal and Pharmaceutical Sciences

XXXII cycle

DESIGN AND DEVELOPMENT OF NANOSTRUCTURED DRUG DELIVERY SYSTEMS BASED ON LIPIDS OR POLYSACCHARIDES FOR THE ADMINISTRATION OF ACTIVE COMPOUNDS THROUGH DIFFERENT ROUTES

PhD Candidate: Eleonora Truzzi

Supervisor: Prof. Eliana Grazia Leo

Ph.D. Program Coordinator: Prof. Giuseppe Biagini

"If you want to see a rainbow you have to learn to see the rain."
Paulo Coelho

"Life is not easy for any of us. But what of that? We must have perseverance and above all confidence in ourselves. We must believe that we are gifted for something and that this thing must be attained."
Marie Curie

This manuscript is dedicated to my family and all my friends who supported me, always holding my hand.

And in the end,

it is dedicated to myself.

INDEX

Abstract 1

Riassunto 2

Introduction 4

Aim of the thesis 11

Chapter 1 12

- Introduction 14
- Materials and methods 16
- Results 21
- Discussion 30
- Conclusions 35

Chapter 2 36

- Introduction 38
- Materials and methods 44
- Results 48
- Discussion 54
- Conclusions 56

Chapter 3 58

- Introduction 60
- Materials and methods 61
- Results and discussion 65
- Conclusions 75

Chapter 4 76

- Introduction 78
- First strategy: materials and methods 80
- First strategy: results 90
- First strategy: discussion 97
- First strategy: conclusions 100
- Second strategy: materials and methods 102
- Second strategy: results 108
- Second strategy: discussion 121
- Second strategy: conclusions 126

Conclusions 127

Acknowledgements 128

References 129

ABSTRACT

Drug delivery systems (DDS) are widely investigated as one of the main tools in medicine due to their potential to treat diseases. During the last two decades, great attention has been focused on nanostructured DDS able to selectively interact with pathogens, cells or tissues. Among all the exploitable materials in formulating DDS, lipids and oligosaccharides exhibit high biocompatibility, biodegradability, and suitability for the administration of drugs through several routes. The aim of this thesis was the development of specific nanostructured DDS designed to enhance efficacy and targeting of active compounds.

In the first project, self-assembled lipid nanoparticles (SALNs) were developed for the encapsulation of heparin-coated iron oxide nanoparticles (Fe@hepa) in order to obtain a nanotheranostic tool able to be absorbed orally through the lymphatic route. SALNs were fully characterized and tested in vitro on cell models (CaCo-2 cell line) for intestinal absorption. The results demonstrated the suitability of SALNs in efficiently delivering Fe@hepa into CaCo-2 cells without causing cytotoxicity.

In the second project, co-loaded liposomes with two first-line antituberculosis drugs, isoniazid (INH) and rifampicin (RIF), were developed for inhaled therapy. Liposomes were characterized in-depth by small-angle neutron scattering technique (SANS). The analysis highlighted that the RIF-INH co-loading elicited a stabilizing effect on the liposome structure, confirmed by the increment of the drug loading capacity.

In a pulmonary tuberculosis context, RIF-loaded solid lipid nanoparticles assemblies (SLNas) were also developed, fully characterized in vitro and administered in vivo on mice. SLNas were formulated with the employment of a newly synthesized mannosylated surfactant (SLNas/MS) for the active targeting to the alveolar macrophages (AM). After administration, SLNas/MS demonstrated the ability to reach the alveolar region and to be retained in the lungs without broad distribution in the body. Furthermore, fluorescence microscopy analysis was performed on AM (collected after the treatment) showing cell internalization of the particles. All the results suggested the suitability of SLNas/MS in efficiently targeting AM.

In the third project, two different strategies based on nanostructured DDS were investigated for an efficient and safe delivery of Geraniol (GER) via nose-to-brain for the treatment of Parkinson's Disease. In the first strategy, polymeric (NP) and lipid-based (SLN) nanoparticles were prepared. In order to obtain long-term stable formulations, the samples were freeze-dried and characterized regarding GER loading. The results indicated that no GER was retained in

the nanoparticles, probably due to its volatility during the freeze-drying process. Therefore, GER-ursodeoxycholic acid conjugate (GER-UDCA, a GER prodrug) was used instead of GER. NP and SLN were developed, characterized regarding drug content, in vitro release and morphology, and finally administered in vivo. The results demonstrated the suitability of GER-UDCA-loaded SLN for the in vivo administration, which guaranteed high concentrations of the prodrug up to 3 hours in the brain without causing any damage to the nasal mucosa.
For the second strategy, inclusion complexes between GER and cyclodextrins (CD) were prepared by using 2-hydroxypropyl-β-CD (HPβCD) and β-CD. The inclusion complexes were characterized in-depth and the results confirmed the real inclusion of GER into CD cavities. In vivo administration of both the inclusion complexes will be further investigated.

RIASSUNTO

I sistemi di veicolazione del farmaco sono largamente studiati come tra i più efficienti metodi per migliorare l'efficacia dei farmaci. Negli ultimi vent'anni un'enorme attenzione è stata focalizzata sui sistemi nanometrici di veicolazione che sono in grado di interagire selettivamente con organismi patogeni, cellule o tessuti. Tra i gli eccipienti utilizzabili nella preparazione di questi sistemi, lipidi e oligosaccaridi mostrano una elevata biocompatibilità, biodegradabilità e idoneità per la somministrazione di farmaci attraverso varie vie. Lo scopo della tesi è stato lo sviluppo di sistemi di veicolazione nanometrici progettati specificatamente per aumentare l'efficacia e il direzionamento di determinati composti attivi.
Nel primo progetto nanoparticelle lipidiche in grado di auto-assemblarsi (SALNs) sono state sviluppate per incorporare a loro volta nanoparticelle di ossido di ferro ricoperte da eparina (Fe@hepa) al fine di ottenere un sistema "teranostico" per via orale assorbibile mediante la circolazione linfatica. Le SALNs sono state caratterizzate e testate in vitro su modelli cellulari (CaCo-2) di assorbimento intestinale. I risultati hanno dimostrato la capacità delle SALNs di veicolare le Fe@hepa in cellule CaCo-2 senza indurre tossicità.
Nel secondo progetto, sono stati sviluppati liposomi co-caricati con due farmaci anti-tubercolosi di prima scelta, isoniazide (INH) e rifampicina (RIF) somministrabili per via inalatoria. I liposomi sono stati caratterizzati mediante la tecnica di scattering di neutroni a piccolo angolo (SANS). Le analisi hanno evidenziato che il co-caricamento di RIF e INH

induce una stabilizzazione sulla struttura dei liposomi, confermata con l'aumento del loro caricamento.

Nel contesto della tubercolosi polmonare, anche nanoparticelle solido-lipidiche in cluster (SLNas) sono state sviluppate, caratterizzate e somministrate in vivo su topi. SLNas sono state preparate mediante un tensioattivo mannosilato di neo-sintesi (SLNas/MS) per il direzionamento attivo ai macrofagi alveolari (AM). Dopo la somministrazione inalatoria, SLNas/MS hanno dimostrato di raggiungere gli alveoli e di localizzarsi nei polmoni senza diffondersi nel resto del corpo. Inoltre, è stata dimostrata l'internalizzazione delle particelle da parte dei AM (raccolti dopo il trattamento) mediante microscopia a fluorescenza. Tutti i risultati suggeriscono la reale capacità delle SLNas di agire sui AM.

Nel terzo progetto, sono state studiate due strategie basate su sistemi nanometrici per una efficiente e sicura veicolazione di geraniolo (GER) per il trattamento del Morbo di Parkinson mediante la via "nose-to-brain". Nella prima strategia nanoparticelle polimeriche (NP) e lipidiche (SLN) sono state preparate, liofilizzate per aumentarne la stabilità e ne è stato valutato il contenuto in GER-. I risultati hanno indicato che, durante la liofilizzazione, il GER non è trattenuto dalle particelle, probabilmente a causa della sua volatilità. Pertanto NP e SLN cariche del coniugato GER-acido ursodesossicolico (GER-UDCA, profarmaco di GER) sono state sviluppate e caratterizzate in termini di contenuto, rilascio in vitro, morfologia, e infine somministrate in vivo. I risultati hanno dimostrato che le SLN garantiscono alte concentrazioni fino a 3 ore del profarmaco nel cervello, senza recare nessun danno alla mucosa nasale. Per la seconda strategia, complessi di inclusione tra GER e ciclodestrine (GER-CD) sono stati preparati usando la 2-hydroxypropyl-β-CD (HPβCD) e la β-CD. I complessi GER-CD sono stati caratterizzati e i risultati hanno dimostrato la reale inclusione di GER nella cavità delle CD. La somministrazione in vivo dei complessi è attualmente in corso.

INTRODUCTION

It is well known that drugs produce pharmacological responses in the body based on their chemical-physical properties and interactions with specific receptors at the target site. However, unless the drug can be driven only in its target site, the efficiency of the therapy can be compromised by the insurgence of side-effects. Moreover, in some cases the drug can barely reach the site of action due to the presence of physiological barriers in the body.

Up until the 1940s, the conventional dosage forms essentially included injections, topical creams and oral formulations (solutions, suspensions, tablets and capsules). Such dosage forms cannot be considered faultless for the delivery of the drugs. In fact, parenteral delivery is highly invasive and generally requires a clinician intervention and the drug effects are usually short-lived. Even though oral administration is very convenient, many drugs (such as insulin), are not absorbed or are degraded by this route. Finally, topical creams are limited to topical effects.

During the 1950s and 1960s, the dosage forms became more advanced; however, drug delivery technologies were limited to sustained-release delivery through the oral route. Significant advances in drug delivery technologies were obtained in 1980s and 1990s, with the advent of dedicated drug delivery research companies and with advances in the molecular, biological and biotechnological field. In fact, the new biopharmaceutics (peptides, proteins, oligonucleotides, etc.) were not suitable for an oral administration, due to their instability and hydrophilicity. Moreover, new administration routes were taken into account and studied, in order to both minimize side-effects and maximize therapeutic effects. Such alternative administrations included intranasal, sublingual, pulmonary and vaginal routes [1].

Therefore, in those years an advanced drug delivery technology arose, generating the drug delivery systems (DDS). A DDS represents a sophisticated system which can incorporate one or more of advanced technologies able to modify pharmacokinetic properties of a drug: bioavailability, controlled release, bio-responsive release to reach a spatial and a temporal delivery. With DDS, a punctual drug targeting to the site of action could be achieved for the first time thanks to the employment of a specific targeting technology (active targeting), such as monoclonal antibodies, peptides, proteins and others exact compounds (an active targeting project is shown in Chapter 4). The developed DDS so far are composed by different materials and they exhibit different physicochemical properties. The correct choice of the DDS depends on the administration route, the target tissue and the physicochemical features of the drug to be delivered. Moreover, one of the most important factors to be considered is the DDS safety,

which includes at least two major entities: the safety of the systemically distributed drug and the biocompatibility of the DDS. Biocompatibility is an expression of the benignity of the relation between a material and its biological environment. Therefore, the biocompatibility of a DDS is highly anatomically dependent and related to the administration route. Over the past few decades, several DDS were developed by using different materials which can be divided in synthetic polymers, natural polymers and lipids. Natural polymers and lipids have gained recent attention in research due to their characteristics. Low toxicity, biocompatibility, biodegradability, improved bioavailability, high drug loading efficiency and controlled-release behavior properties of such materials boosted their application in the development of DDS [2–4].

1. Natural polymers: cyclodextrins

Natural polymers are produced from natural sources. In DDS, the most frequently used type are polysaccharides and proteins [3]. Cyclodextrins (CDs) can be classified as oligosaccharides since they are obtained by the enzymatic degradation of starch, a polymeric natural source. CDs were first discovered in the late 19th century by Antoine Villiers, during experiments of degradation and reduction of carbohydrates under the action of ferments. However, only about 15 years later, the unique property of CDs to form inclusion complexes was identified by Schardinger, considered as the "Founding Father". At that time the structures of these molecules were still undefined, and they were elucidated by X-ray crystallography in 1942: CDs are cyclic oligosaccharides composed by glucopyranose units linked through α-1,4 glycosidic bonds with a hydrophilic external surface and a hydrophobic internal cavity. The pharmaceutical application arose in the mid '70s when the non-toxicity of CDs became accepted and several manufacturers started to produce and market. From that moment, CDs were used to enhance the solubility of drugs replacing the often-used substances which can cause irritation (alcohols, surfactants, propylene glycol ...). Due to their ability to increase drug solubility, the stability, bioavailability and pharmacokinetic properties of drugs were enhanced, thus increasing drug efficiency. CDs became also attractive for their versatility and suitability in several administration routes, such as the oral, parenteral, rectal, sublingual [5].

1.1 CDs properties and inclusion complex formation

The most common natural CDs are composed by six (α-cyclodextrin), seven (β-cyclodextrin) or eight (γ-cyclodextrin) glycosyl units. These macromolecules are the first generation or parent

CDs. Chemical modification of CDs can alter their physical properties by improving solubility, stability against light or oxygen and helping in controlling the chemical activity of guest molecules. Natural CDs and their derivatives currently in use in pharmaceutical products are described in Table 1.

Table 1. Cyclodextrins currently in use in pharmaceutical products [6].

Cyclodextrin	Abbreviation	Cavity diameter (Å)	Molecular weight	Solubility in water at 25 °C (mg/mL)
α-cyclodextrin	αCD	4.7 – 5.3	972	145
β-cyclodextrin	βCD	6.0 – 6.5	1135	18.5
γ-cyclodextrin	γCD	7.0 – 8.3	1297	232
2-hydroxypropyl-β-Cyclodextrin	HPβCD	6.0 – 6.5	1541.6	>600
2-hydroxypropyl-γ-Cyclodextrin	HPγCD	7.0 – 8.3	1761.8	>500
Randomly methylated b-cyclodextrin	RMβCD	6.0 – 6.5	1312	>500
Sulfobutylether-β-cyclodextrin	SBEβCD	6.0 – 6.5	2163	>500

CDs have a truncated cone appearance with a cylinder-like shape due to the spatial arrangement characteristic of the functional groups of glucose units. The characteristic arrangement confers a hydrophobic feature to the interior of the cavity, while the presence of hydroxyl groups at the edges of the trunked cylinder makes them water soluble. As a result of their molecular shape, CDs exhibit the unique ability to intercalate a guest molecule inside its cavity and act as a molecular container. The interaction between the CDs and the guests leads to the formation of an inclusion complex due to hydrophobic interaction within the lipophilic portion of the guest molecule and CD internal cavity. The main driving force of complex formation is the release from CDs cavity of enthalpy-rich water molecules, which are displaced by more hydrophobic guests, resulting in a more stable lower energy state.

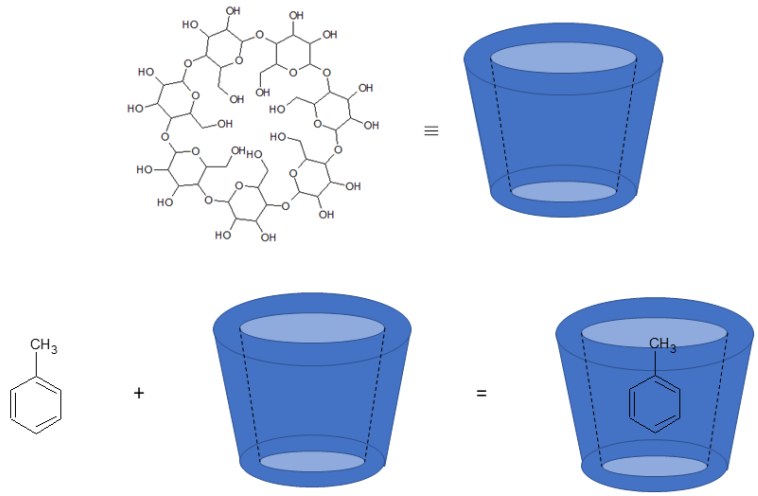

Figure 1. Cyclodextrins structure and inclusion complex formation.

The interaction between the guest and the host (CD) is not fixed or permanent but is a dynamic equilibrium. The binding strength depends mostly on host-guest fitting and on guest polarity. In fact, guest molecule much smaller than host cavity will pass easily through the cavity and the bond will be weak, while polar guest molecules will not be able to displace water molecules from the internal cavity.

1.2 CDs advantages and toxicity

Being each guest molecule individually surrounded by a CD, the complexation leads to advantageous changes in the chemical and physical properties of the guest. First of all, an improvement of the water solubility of complexed lipophilic compounds can be obtained due to the high hydrophilicity of the external surface of CDs. Moreover, guest molecules can be protected against degradation by microorganisms, light and oxygen-sensitive species. Finally, volatile liquids, such as essential oils and their components, can be fixed, converted into powders and their taste and smell can be masked. In particular, several studies demonstrated the increased stability of the oils after their inclusion in CDs complexes against air, light, moisture and heat [7,8]. Moreover, the entrapment of oils in CD cavity at molecular level protects the biological membranes from direct contact of the irritant compound. For these reasons, CDs and their derivatives are suitable for application in analytical chemistry, agriculture, pharmaceutical field, in food and toilet articles [9]. Moreover, αCD, βCD and HPβCD are listed in the European Pharmacopoeia (Ph.Eur.) and γCD is referenced in the Japanese Pharmaceutical Codex and will be soon included in the Ph.Eur.

In 2000-2004, αCD, βCD and γCD were introduced into the Generally Regarded as Safe (GRAS) list of the Food and Drug Administration (FDA) for use as a food additive. SBEβCD and HPβCD are mentioned in the FDA's list of Inactive Pharmaceutical Ingredients. CDs toxicological data and clinical safety are reported into the Annex of the European Commission Guideline in "Excipients in the labelling and package leaflet of medicinal products for human use". Overall, the use of CDs in medicinal products is not a risk for humans: below 20 mg/kg/day no serious adverse effects have to be expected for all administration routes. Above 200 mg/kg/day CDs may theoretically cause problems in the digestive system after oral administration, and mild renal toxicity after parenteral administration [10].

Regarding the intranasal administration, it has been shown that CDs, in general, and several modified CDs such as the more soluble derivative hydroxypropyl-beta-cyclodextrin (HP-β-CD) notably enhance intranasal absorption of drugs [11,12]. The effect of CDs on the respiratory cell layer permeability was investigated in vitro and shown to be concentration-dependent and variable according to the type of CDs, type of chemical modification, and degree of substitution [13]. HP-β-CD and natural-CDs are safest in terms of cytotoxicity [14], thus they were selected as potential carriers for GER in nose to brain experiments.

2. Lipids and lipid-based carriers

Lipids are esters of fatty acids, lipophilic hydrocarbon chains linked to a hydrophilic group, such as glycerol, polyglycerol or polyalcohol. In nanomedicine, lipids can be used as material to prepare several DDS, such as solid lipid nanoparticles (SLNs), nanostructured lipid carriers (NLCs) and liposomes. The first dosage form incorporating hydrophobic drugs in lipid droplets was developed in the '60s as a parenteral fat emulsion, currently widely used for parenteral application of poor water-soluble drugs [15].

2.1 Liposomes

In the same years, Bangham and Horne first noticed how phospholipids combine with water to immediately form a unique spherical structure now recognized as liposome [16]. The discovery of liposomes represented in that period a unique tool for the study of several cellular membrane functions. Only after several years, liposomes were considered as a therapeutic tool for the delivery of pharmacologically active compounds for the treatment of different diseases. Even almost 50 years later, liposomes represent one of the most studied drug delivery systems due to their incredible features. In fact, these vesicles composed by a lipid membrane surrounding an

aqueous internal core present several advantages, such as biocompatibility, biodegradability, non-toxicity, targetability, ability to load both hydrophilic and lipophilic compounds. Currently, among all the DDS studied and developed in the nanometric range, in clinical use liposomes are mainly present.

Liposomes are usually classified regarding the number of the lipid membranes and their size. They can be classified as small or large unilamellar (20-100/200 nm), oligolamellar (100-500 nm) or multilamellar (100-500 nm) systems [17].

The lipid membrane is composed by components of the cellular membrane, phospholipids and cholesterol, and for this reason liposomes have a high biocompatibility. The phospholipid amphiphilicity confers the ability to self-assembly and create the liposome structure. Several different phospholipids can be used for liposome production. All of them are composed by two hydrophobic fatty acid tails and a hydrophilic head with a phosphate group, which is linked to an alcohol. Depending on the type of alcohol, the fatty chain length and degree of unsaturation, the phospholipids can exhibit different physicochemical properties. Several phospholipids, both naturals and synthetics, are currently used to prepare liposomes which are in clinical use. For all these approved clinical products, the toxicity related to the administration of the drug has been demonstrated to be decreased due to the employment of liposomes as DDS [18].

Moreover, liposomes are currently used in cosmetics in order to overcome restrictions related to drugs or active compounds, such as the low permeation, stability, solubility, duration and high side effects or costs [19].

2.2 SLNs and NLCs

In the 90s, Müller *et al*. developed the first generation of SLNs [20]. These lipid-based nanoparticles presented some disadvantages, such as low drug loading. For this reason, the second generation of lipid nanoparticles, NLCs, was obtained. Such kind of carriers, exhibit high bioavailability and biocompatibility, controlled release, physical stability and protection of incorporated labile drugs. Both SLNs and NLCs demonstrated an excellent tolerability with several administration routes, such as oral, intravenous, pulmonary and transdermal administration. The great advantage of these nanocarriers is the possibility to obtain them with a "green" technique, without the employment of solvents, which are associated to toxicity [21].

SLNs are prepared by using one or more solid lipids, while NLCs are composed by both solid and oil lipids. For both the lipid-based carriers, the employment of surfactants is necessary in order to obtain a stable dispersion in water. The lipids commonly used to prepare lipid-based nanoparticles are mono-, di-, and triglycerides, fatty acids, waxes and steroids. The lipids and

surfactants employed to obtain SLNs and NLCs are GRAS and commonly used in marketed products [2,22] (Table 2).

Table 2. Ingredients used in SLNs fabrication [2].

SLN composition	Class	Example
Lipids	Glycerol esters	Glyceryl trimyristate
		Glyceryl tristearate
		Glyceryl tripalmitate
		Glyceryl trioleate
		Glyceryl tricaprate
		Glyceryl monostearate
		Glyceryl distearate
		Glyceryl behenate
		Glyceryl palmitostearate
		Hydrogenated coco-glycerides
		Hydrogenated palm kernel glycerides
		Hydrogenated castor oil
		Soybean oil
		Peanut oil
		Fully hydrogenated soybean oil
	Waxes	Cetyl palmitate
		Beeswax
		Carnauba wax
	Fatty acids	Myristic acid
		Stearic acid
		Palmitic acid
		Tetradecanoic acid
		Arachidic acid
Emulsifiers	Phospholipids	Egg lecithin
		Soya lecithin
		Hydrogenated soya lecithin
	Steroids	Cholesterol
		Cholesteryl oleate
	Non-ionic surfactants	Poloxamer 188
		Poloxamer 407
		Polysorbate 20
		Polysorbate 80
		Polyoxyethylene-20-cetyl ether
		Polyoxyethylene-20-isohexadecyl ether
		Polyoxyethylene-20-oleyl ether
		Sorbitan monooleate
		Polyethylene glycol (15)-hydroxystearate
		Polyethylene glycol monostearate
		Macrogol(25)-cetostearyl ether
		Polyvinyl alcohol
	Anionic surfactants	Sodium lauryl sulphate
Co-surfactants	Alcohols	1-Butanol
	Bile salts	Taurodeoxycholate
		Cholate
		Taurocholate

AIM OF THE THESIS

In the present thesis, different DDS composed by lipids or cyclodextrins have been designed on the basis of the drug and of the chosen administration route, and evaluated *in vitro* and/or *in vivo*.

Each chapter represents a different project in which an active compound is delivered by a definite DDS through a specific administration route.

Chapter 1

Self-Assembled Lipid Nanoparticles for Oral Delivery of Heparin-Coated Iron Oxide Nanoparticles for Theragnostic Purposes

Eleonora Truzzi [1], Chiara Bongio [2], Francesca Sacchetti [1], Eleonora Maretti [1], Monica Montanari [3], Valentina Iannuccelli [1], Elena Vismara [2] and Eliana Leo [1]

[1] Department of Life Sciences, University of Modena and Reggio Emilia, via Campi 103, 41125 Modena, Italy;

[2] Department of Chemistry, Materials and Chemical Engineering "G. Natta", via Mancinelli 7,

Politecnico di Milano, 20131 Milano, Italy;

[3] Department of Life Sciences, University of Modena and Reggio Emilia, via Campi 287, 41125 Modena, Italy;

Molecules **2017**, 22, 963; doi:10.3390/molecules22060963

ABBREVIATIONS

CLSM: confocal laser scanning microscopy

DL: drug loading

DMEM: Dulbecco's Modified Eagle's Medium

EDX: energy dispersive X-ray

EE: encapsulation efficiency

FBS: fetal bovine serum

Fe@hepa: heparin non-covalent coated iron oxide nanoparticles

MFH: magnetic fluid hyperthermia

MNPs: magnetic nanoparticles

MRI: magnetic resonance imaging

MTT: methyl thiazole tetrazolium test

P/S: penicillin–streptomycin

PBS: phosphate buffer saline

PCS: photon correlation spectroscopy

PDI: polydispersity index

SALNs: self-assembled lipid nanoparticles

SEM: scanning electron microscopy

SLNs: solid lipid nanoparticles

STEM: scanning transmission electron microscopy

TEM: transmission electron microscopy

1. INTRODUCTION

Currently, oral delivery is the most accepted route of drug administration, even though it is associated with poor drug bioavailability. One of the most promising strategies to overcome these limitations is the use of nanomedicine or nano-drug delivery systems [23]. As an example, solid lipid nanoparticles (SLNs) have attracted increasing attention owing to their biocompatibility and biodegradability. SLNs are composed of lipids in a solid state at room temperature and surfactants. They are produced using hot or cold homogenization without the employment of organic solvents and generally have low production costs. SLNs offer advantages such as good tolerability, high oral drug bioavailability and low acute and chronic toxicity [4,24]. Moreover, being composed of lipids, SLNs have shown good potential in achieving drug delivery into the systemic circulation through intestinal lymphatic absorption [25–27]. After oral administration, small and hydrophilic substances enter in the systemic circulation by a passive absorption mechanism through enterocytes. On the contrary, large and lipophilic compounds with a $\log P \geq 5$ (where P is the octanol/water partition coefficient), such as components of SLNs, are metabolically stable (in the intestinal lumen and within enterocytes) and can be considered good candidates for lymphatic transport to the systemic circulation [28]. Drug adsorption via the intestinal lymphatic system has several major advantages, including circumventing first-pass metabolism and targeting drugs to diseases that spread through the lymphatic system. For example, cancer cells use the lymph nodes as a reservoir to spread to the other areas of the body [29]. The main ways to deliver drugs to intestinal lymphatic vessels are through lymphatic capillaries, gut-associated lymphoid follicles that form Peyer's patch, and finally the intestinal walls via transcellular absorption. This last route is the lymphatic target of lipid-based nanoformulations because during transit across the enterocyte the lipids become associated with chylomicrons which are secreted into the mesenteric lymph duct [30–33]. SLNs have to satisfy certain requirements to achieve lymphatic delivery. It was observed that the uptake and fate of SLNs are influenced by particle size, surface hydrophobicity, type of lipids, and concentration of the emulsifier [23,27,34]. Also, the surface charge plays an important role: negatively-charged carriers have been reported to show higher lymphatic uptake than neutral or positively-charged particles [23,30,35]. SLNs promote lymphatic absorption and can also be exploited for theragnostic purposes, which to the best of our knowledge, have not been extensively investigated [36]. Theragnostic is the fusion of therapeutic and diagnostic approaches aiming to personalize and advance medicine. Magnetic nanoparticles (MNPs) represent a particularly appropriate tool based on their ability to be simultaneously functionalized and guided by external magnetic fields [37]. Some MNPs-based

therapeutic applications include magnetic fluid hyperthermia (MFH), magnetic resonance imaging (MRI) and magnetic drug targeting [38,39]. In this field, iron oxide (Fe_3O_4) MNPs provide a unique nanoplatform with tunable sizes and surface chemistry studied extensively for MRI and MFH applications [40]. Without a coating, MNPs have hydrophobic surfaces with a high area to volume ratio and a propensity to agglomerate. An appropriate surface coating allows MNPs to be and remain homogenously dispersed for longer times. Several materials have been used to modify the surface of MNPs, such as organic polymers (dextran, chitosan, polyethylene glycol), organic surfactants (sodium oleate and dodecylamine), and metals [37]. Vismara et al. proposed the use of heparin as a non-covalent coating for iron oxide nanoparticles (Fe@hepa) [41]. Heparin, a natural polysaccharide with many bioactive properties, is a heterogeneous, polydisperse, highly sulphated glycosaminoglycan composed of 1 → 4 linked disaccharide repeating units. Each unit consists of an α-D-glucosamine and either a hexuronic acid, α-L-idruronic or β-D-glucoronicacid unit, with O-sulphate groups at different positions of the disaccharide. Various studies have demonstrated that heparin and low-molecular-weight heparins, in addition to having anticoagulant properties, are anti-angiogenic agents and can be used as vectors to reach tumor sites due to their ability to bind over-expressed proteins [42–44]. Thanks to these features, the heparin coating specifically directs iron oxide nanoparticles to tumor environments in order to accomplish the theragnostic aim. Moreover, Vismara et al. demonstrated an increased stability in a water suspension of Fe@hepa nanoparticles with respect to naked iron oxide by conferring a negative charge due to the heparin coating [41]. However, the heparin surface shell is instable in physiologic environment where the presence of ions reduces the strength of the electrostatic bond between the positive iron oxide core and the negative heparin chain. Therefore, the purpose of the present work was to design a nano-theragnostic tool based on Fe@hepa nanoparticles for oral absorption through the lymphatic route. To the best of our knowledge, in the theragnostic field poor attention has been addressed to the study of this promising approach. In order to stabilize the heparin coating in physiological environments, and at the same time promote oral absorption through the lymphatic route, Fe@hepa were encapsulated in a biocompatible solid lipid shell to obtain self-assembled lipid nanoparticles (SALNs). SALNs were obtained by self-emulsification process and were characterized with regard to their size, encapsulation efficiency, in vitro cytotoxicity and ability to be internalized into the CaCo-2 cell line (colon rectal adenocarcinoma cell line of human origin) used as a model for an indirect indication of lymphatic uptake.

2. MATERIALS AND METHODS

2.1 Materials

Geleol™ (Glycerol Monostearate 40–55, type I) and Gelucire 50/13® Pellets (Stearoyl Macrogol-32 Glycerides) were a kind gift from Gattefossè (Saint-Priest, France). Fe@hepa (containing 9% w/w of heparin) were provided by the laboratory of Prof. E. Vismara and synthesised as previously described [41]. Azure II and Nile red were purchased from Sigma-Aldrich Italia (Milan, Italy). Potassium thiocyanate was purchased from Carlo Erba Reagenti (Milan, Italy). Hoechst 33342 stain was purchased from ThermoFisher (Monza, Italy). Dulbecco's Modified Eagle's Medium with high glucose (DMEM), L-glutamine, fetal bovine serum (FBS), penicillin–streptomycin (P/S), phosphate buffer saline (PBS), sodium pyruvate and other culture reagents were purchased from EuroClone (Milan, Italy).

A MilliQ water system (Millipore; Bedford, MA, USA) provided high purity water (18.2 MW) for these experiments.

All other chemical reagents were obtained commercially as reagent-grade products.

2.2 SALN formulation

SALNs were obtained by a self-assembling process using an original technique in which no organic solvents were employed (Figure 1). Briefly, a mixture of Geleol:Gelucire 1:1 w/w was melted at 65 °C after the addition of 50 μL of MilliQ water containing Fe@hepa (1 or 5 mg) and emulsified by ultrasound energy (Vibra-Cell, Sonic & Materials, Inc. 53 Church Hill Road, Newton, CT, USA) at 10 output Watt for 30 s. This water/oil (W/O) dispersion was rapidly solidified in ice bath and then added to 15 mL of MilliQ water, previously heated at 65 _C. To obtain the SALNs, the dispersion was homogenized for 3 min at 24,000 rpm by Ultra-Turrax (T-25 basic IkaLabortecnik, Staufen, Germany) and then cooled in ice for about 10 min to allow the SALN solidification. SALNs–Fe@hepa were purified by centrifugation at 2000 rpm for 5 min at 20 °C (Rotina 380R, Hettich, Kirchlengern, Germany) to remove the non-encapsulated Fe@hepa. The purified suspensions of SALNs were stored at +4 °C.

Unloaded SALNs were obtained omitting the addition of Fe@hepa in the 50 μL of MilliQ water, while labelled SALNs for cell internalization studies were obtained by adding Nile red (0.01%) in the melted Geleol™.

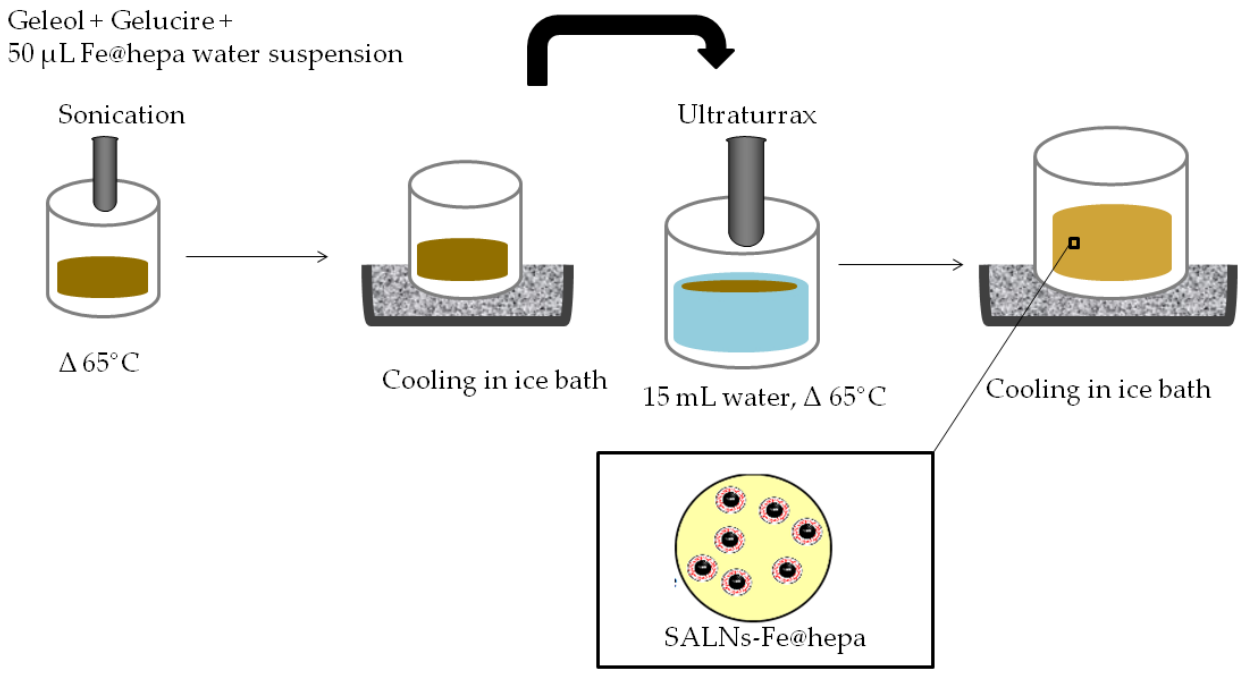

Figure 1. Scheme of self-assembling process used for SALN formulation.

2.3 SALN characterization

SALN size and polydispersity index (PDI) were determined by photon correlation spectroscopy (PCS) technique using a Zetasizer Nano ZS analyzer system (Zetasizer version 6.12; Malvern Instruments, Worcs, UK). The results were expressed as the average of three different measurements.

Particle surface charge (Z-Potential value) was measured by using the same apparatus, equipped with a 4 mW He–Ne laser (633 nm) and DTS software (Version 5.0, Malvern Instruments, Worcs, UK). Measurements were performed in triplicate and each measurement was averaged over at least 12 runs.

2.4 Morphological studies

SALN morphological features were analyzed by field-emission gun scanning electron microscopy (SEM-FEG, Nova 11 NanoSEM 450, Fei, Eindhoven, The Netherlands) using both the scanning electron microscopy (SEM) and the transmission electron microscopy (TEM) mode. For the SEM mode, a few drops of the SALNs suspension were placed on an aluminum stub (TAAB Laboratories Equipment Ltd., Aldermaston, Berks, UK) covered by a double side sticky tab (TAAB Laboratories Equipment Ltd., Aldermaston, Berks, UK) and, after drying, vacuum coated with gold–palladium in an argon atmosphere for 60 s (Sputter Coater Emitech

K550, Emitech LTD, Ashford, Kent, UK). For the TEM mode a scanning transmission electron microscopy (STEM) detector characterized by a low voltage electron beam (30 kV) was employed. TEM 200 mesh Formvar/Carbor Coppergrids (TAAB Laboratories Equipment Ltd., Berks, UK) were immersed in SALNs diluted suspension (1:10 v/v in water) and dried at room conditions (25 °C, 760 mmHg) before the analysis.

Elemental composition of Fe@hepa loaded or unloaded SALNs was determined by energy disperse X-ray (EDX) analysis with X-EDS Bruker QUANTAX-200 (Bruker Nano GmbH, Berlin, Germany) coupled with SEM-FEG. Elements can be identified qualitatively and semi-quantitatively as a function of the X-ray energy emitted by their electrons transferring from a higher energy shell to a lower energy one. The X-ray emissions from the Kα or Lα levels were measured for the following atoms: oxygen (Kα = 0.525 keV), carbon (Kα = 0.277 keV), silicon (Kα = 1.740 keV), aluminum (Kα = 1.487 keV) and iron (Kα = 6.404 keV, Lα = 0.705 keV).

2.5 Drug Loading and Encapsulation Efficiency

The determination of Fe@hepa loaded in SALNs was performed by indirect method analyzing the amount of non-encapsulated Fe@hepa by a spectrophotometric method based on the formation of highly-colored complexes iron-thiocyanate ion.

Briefly, after obtaining SALNs, the separation of the non-encapsulated Fe@hepa (free Fe@hepa) was carried out by centrifugation (see Section 2.2). The pellet was re-suspended in 200 μL of milliQ water and digested in 1 mL of HCl 37% w/w for 2 h at 60 °C. Subsequently, 1.5 mL of 0.1 M solution of potassium thiocyanate (KSCN) was added to form the red-colored $[FeKSCN]^{2+}$ iron complex. The amount of free Fe@hepa was determined by recording absorbance at 480 nm (Lambda 35 UV/VIS, Perkin-Elmer, Norwalk, CT, USA). The standard calibration curve for iron complex was performed under identical conditions with known amounts of naked Fe@hepa and using KSCN and HCl solution
as blank [45].

The encapsulation efficiency (EE%) and drug loading (DL μg/mg) were calculated by using the following equations:

$$EE\% = \frac{initial\ Fe@hepa\ (mg) - free\ Fe@hepa\ determined\ (mg)}{initial\ Fe@hepa\ (mg)}\ x\ 100$$

$$DL\ \left(\frac{\mu g}{mg}\right) = \frac{encapsulated\ Fe@hepa\ (\mu g)}{total\ mass\ of\ SALNs\ composition\ (mg)(lipids\ and\ Fe@hepa)}$$

where encapsulated Fe@hepa were calculated by subtracting the amount of free Fe@hepa determined from the initial amount added to the preparation. The experiments were conducted in triplicate and the results were expressed as average ± standard deviation (SD).

2.6 In vitro SALNs-Fe@hepa stability

In order to evaluate the in vitro stability of SALNs–Fe@hepa, the amount of Fe@hepa separated gradually at 4 °C for one month by spontaneous precipitation was quantified.
Practically at predetermined intervals (2, 4, 6, 8, 10, 20 and 30 days), the pellet deposited at the bottom of the vials of the SALNs-Fe@hepa suspension was determined. The pellet was recovered, re-suspended in 200 μL of milliQ water and digested in 1 mL of HCl 37% w/w for 2 h at 60 °C. After that, the solution was analyzed to determine the amount of iron in accordance with the method described above. The analyses were performed in triplicate.

2.7 Stability of heparin coating

In order to analyze the stability of the heparin coating in Fe@hepa before and after the formation of SALNs, the amount of heparin released in saline solution from naked Fe@hepa and SALNs-Fe@hepa was evaluated.
Briefly, a known amount of sample was incubated under magnetic stirring in 0.9% NaCl water solution at 37 °C for 1 h. Then, the suspension was centrifuged for 25 min at 9500 rpm at room temperature (Rotina 380R) in order to separate nanoparticles (naked Fe@hepa or SALNs–Fe@hepa) from the supernatant. The amount of heparin released in the supernatant was determined by using a modified Azure II colorimetric method [46]. Typically, aliquots (500 μL) of aqueous solution were reacted with 4.5 mL of the Azure solution (0.01 mg/mL) and assayed at 654 nm by vis-spectroscopy
(Lambda 35 UV/VIS). Quantification was achieved by comparing the absorbance of the samples to a regression curve determined from medium spiked with increasing amount of heparin. The experiments were conducted in triplicate.

2.8 In vitro Nile red release

Nile red released from SALNs was evaluated during 24 h. Labelled SALNs (40 mg) were incubated at 37 °C in 40 mL of phosphate buffer (20 mM, pH 7.4) or DMEM added with serum, under magnetic stirring. 1 mL of SALNs suspension was withdrawn from the system at time intervals of 30 min and replaced with 1 ml of fresh solvent to maintain constant volume. The

sample was centrifuged at 9500 rpm for 25 min and Nile red content was determined in the supernatant by vis-spectroscopy at 525 nm. The analysis was performed in triplicate.

2.9 Cell culture

CaCo-2 cell line were cultured as a monolayer in Dulbecco's Modified Eagle's Medium with high glucose (DMEM) containing L-glutamine 2 mM, penicillin 100 UI/mL, streptomycin 100 μg/mL, sodium pyruvate and 10% of fetal bovine serum (FBS) at 37 °C in a humidified atmosphere (5% CO2). Cells were sub-cultured when the confluence was $\geq$ 80%.

2.10 Cytotoxicity assay

CaCo-2 cells were seeded at a density of 60,000 cells/well in 24-well plate in complete DMEM medium for 48 h. Cells were then treated with Fe@hepa, unloaded SALNs and SALNs–Fe@hepa samples at different concentrations (0.8, 1.2, 1.6 and 2 mg/mL for SALNs, and respective Fe@hepa concentrations) for 2, 4, and 6 h. After incubation times the methyl thiazole tetrazolium test (MTT) was performed to assess cell viability. Optical densities were measured spectrophotometrically at 570 nm with a multiplate reader (TecanGenios Pro with Magellan 6 software). Cell viability was expressed as a percentage of cell survival respect to the control (untreated cells).
The experiment was performed in triplicate.

2.11 Quantification of SALNs–Fe@hepa on CaCo-2 cell model

The amount of Fe@hepa up-taken by the CaCo-2 cells after treatment with Fe@hepa and SALNs–Fe@hepa at different incubation times was quantified by adapting a method previously reported [47]. Cells were seeded in 6-well plate at density of 250,000 cells per well in complete DMEM medium for 48 h. Then, cells were incubated with 2 mg/mL of SALNs–Fe@hepa and a proportional amount of naked Fe@hepa (53 μg/mL) for 2, 4 and 6 h. At the end of the incubation time, cells were washed with PBS and the amount of iron associated to the cells was quantified using the method described in Section 2.5. The experiments were performed in triplicate. In order to compensate the matrix effect, the calibration curve for iron quantification was prepared incubating different known amounts of Fe@hepa in the presence of unloaded SALNs into CaCo-2 cells.

2.12 Confocal laser scanning microscopy studies of monolayers

The confocal laser scanning microscopy (CLSM) of fixed cells was performed with a Leica DM IRE2 microscope (Mannheim, Germany) and a Leica Confocal System equipped with a scanner multiband 3-channel Leica TCS SP2 with AOBS, laser diode blue COH (405 nm/25 mW), laser Ar (458 nm/5 mW) (476 nm/5 mW) (488 nm/20 mW) (496 nm/5 mW) (514 nm/20 mW), laser HeNe (543 nm/1.2 mW), laser HeNe (594 nm) (orange) and laser HeNe (633 nm/102 mW). CaCo-2 cells, seeded at a density of 100,000 cells per well in a chambered coverglass (Lab-Tek®, Thermo-scientific, Milan, Italy), were incubated with naked Fe@hepa (53 μg/mL), Nile red-labelled unloaded SALNs (2 mg/mL), and Nile red-labelled SALN–Fe@hepa (2 mg/mL). After 4 h of incubation, the treated cells were washed twice with PBS, fixed in paraformaldehyde (3% w/v) for 20 min at room temperature, stained with 2 μg/mL Hoechst 33342 dye and analyzed with CLSM.

2.13 Statistical analysis

Statistical analysis was performed using the one-way analysis of variance (ANOVA). The data are represented as mean ± SD. Difference was considered statistically significant at *p*-values less than 0.05.

3. RESULTS

3.1 SALN characterization

By using the original self-emulsification process, two SALNs–Fe@hepa samples were developed using 1 or 5 mg of Fe@hepa (namely SALNs–Fe@hepa1 and SALNs–Fe@hepa5, respectively). The particle size, PDI and Z-potential values obtained with PCS analysis are shown in Table 1. No differences in the particle size nor in the PDI values were observed, regardless of the amount of Fe@hepa used (all the samples were roughly of 180 nm with a PDI of 0.3), while the negative charge of the particle surface (Z-potential value) increased with the increase of the initial amount of Fe@hepa utilized in the preparation. The particle size was monitored for one month and no significant changes were observed (data not shown). The size and the Z-potential of naked Fe@hepa were previously reported [41] and were 92 nm and −61 mV, respectively.

Table 1. Size, polydispersity index (PDI) and Z-potential values of loaded and unloaded self-assembled lipid nanoparticles (SALNs). Fe@hepa1: iron oxide nanoparticles non-covalently coated with heparin (1 mg); Fe@hepa5: iron oxide nanoparticles non-covalently coated with heparin (5 mg).

	Size (nm)	PDI	Z-potential (mV)
Unloaded SALNs	182 ± 15	0.295 ± 0.015	−16.4 ± 4.7
SALNs-Fe@hepa1	183 ± 18	0.278 ± 0.008	−15.5 ± 5.8
SALNs-Fe@hepa5	186 ± 21	0.364 ± 0.013	−24.0 ± 5.5

3.2 Morphological studies

Morphological characterization of the samples was performed using the scanning electron microscopy analysis (SEM modality) to visualize the particles in solid form, while the scanning transmission electron microscopy analysis (STEM modality) was used to observe the samples as suspension. Both the analyses were performed in high-vacuum conditions. Figure 2A shows, as an example, the image of SALNs–Fe@hepa1 at high magnification (100,000x) using the SEM technique. Even if SALNs appeared aggregated in clusters, each single particle could be clearly recognized as a distinct solid structure with a roughly spherical morphology.

By STEM modality (Figure 2B), unloaded SALNs in suspension were hardly detectable due to their intrinsically low electron density that limits the resolution. However, even if the particles appeared as weak-contrast dark formations, their imperfectly spherical morphology was easily observable. Figure 2C,D shows the STEM images of loaded particles (SALNs–Fe@hepa5). At low magnification (Figure 2C), SALNs–Fe@hepa5 appeared irregular in the shape, as observed also for the unloaded particles, but with a darker inner structure. The high-contrast dark part in the core region of each particle could be assigned to the Fe@hepa clusters, while the clear part surrounding the core regions could be attributable to the lipid shell. At high magnification (Figure 2D) one single particle with a rough contour was observed. Within the particle, even if not perfectly in the center, dark small dots, due to clusters of Fe@hepa nanoparticles, were clearly visible. The clusters appeared surrounded by a weak-contrast dark part attributable to the lipid matrix, according to the images of the unloaded sample (Figure 2B). The particle sizes of SALNs–Fe@hepa5 as well as of the Fe@hepa nanoparticles were also consistent with PCS analysis results reported in Table 1 and in previous studies [41], respectively.

To confirm the composition of the particles observed by the electron microscopy analysis, the qualitative EDX analysis was performed by the single-point method. A single loaded nanoparticle, as observed in the image reported in Figure 2D, was analyzed in comparison with an individual unloaded nanoparticle and the qualitative composition was reported in the EDX spectra representing the plots of X-ray counts vs. elements. In spectrum relating to SALNs–Fe@hepa, the peak of iron was clearly visible (Figure 3A), while it was absent in unloaded

particles (Figure 3B), confirming the presence of Fe@hepa into the loaded SALNs. In the spectra, the presence of Al and Si were probably due to the support used for the analyses.

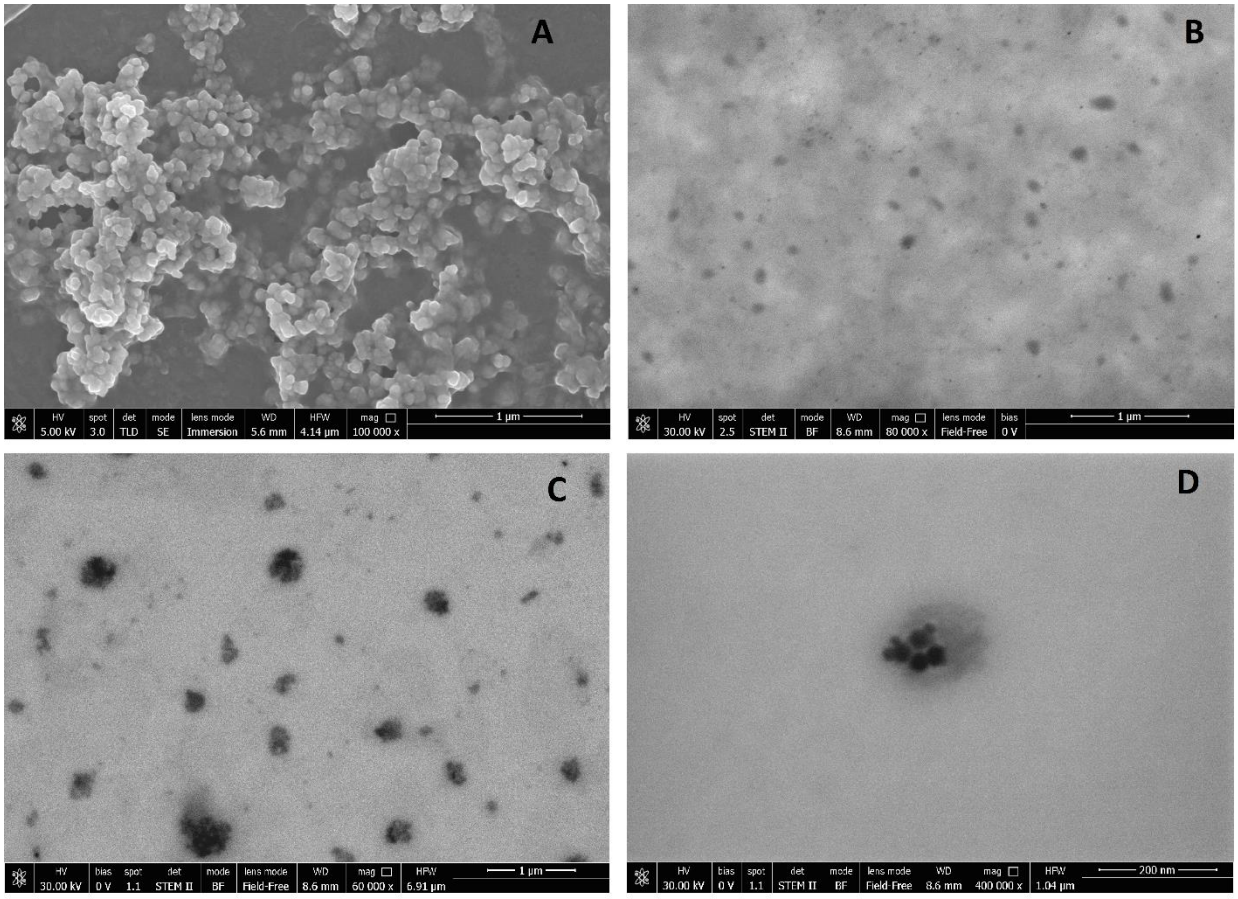

Figure 2. (A) SEM microphotograph of SALNs-Fe@hepa1 at high magnification (100,000 X); (B) Representative scanning transmission electron microscopy (STEM) image of unloaded SALNs; (C) Representative STEM image of SALNs-Fe@hepa5 at low magnification (60,000 X); (D) Representative STEM image of SALNs-Fe@hepa5 at high magnification (400,000 X).

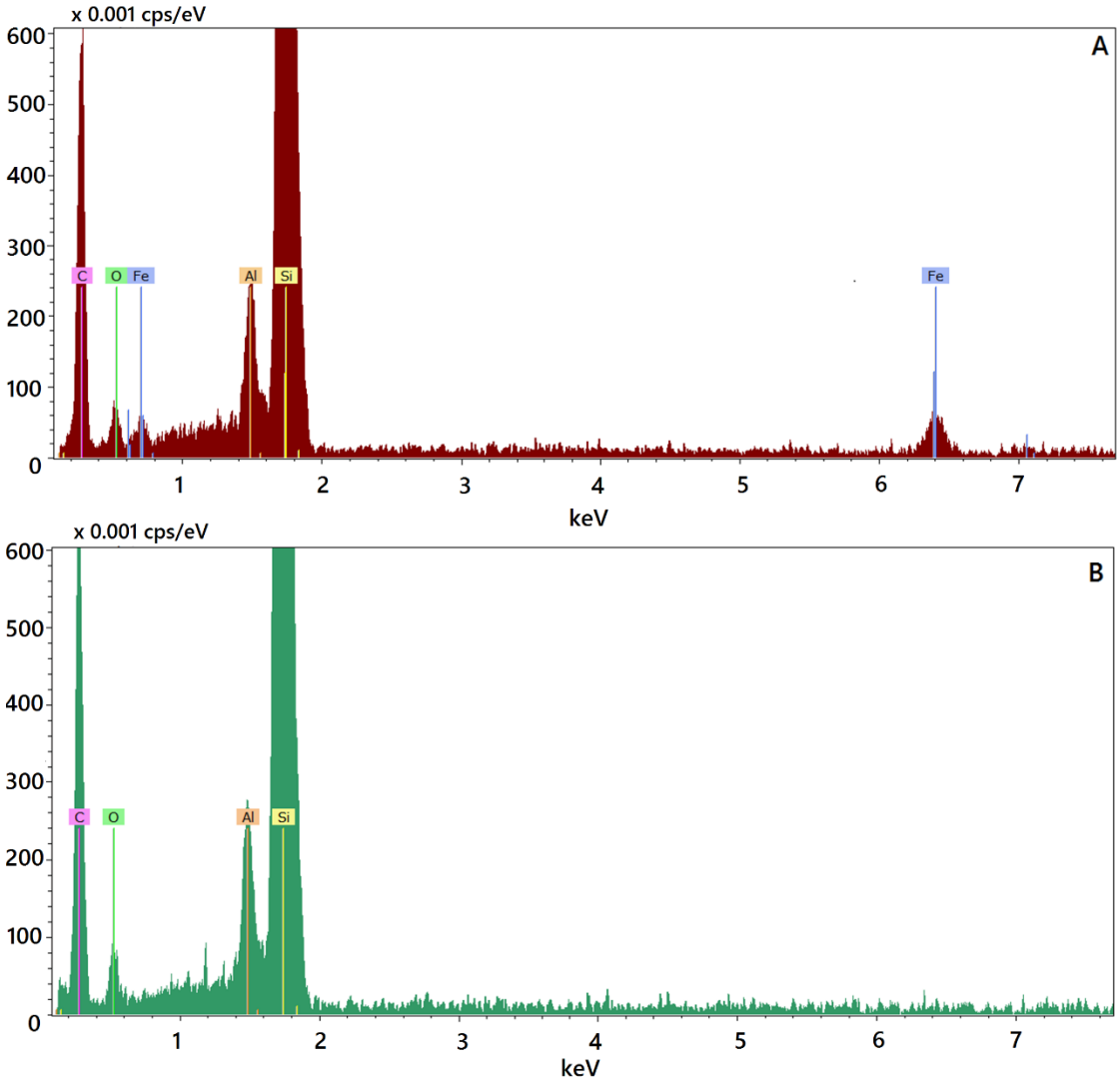

Figure 3. Energy dispersive X-ray (EDX) spectra referred to SALNs–Fe@hepa5 (A) and unloaded SALNs (B).

3.3 Drug Loading and Encapsulation Efficiency

The amount of Fe@hepa loaded inside SALNs was calculated by indirect method, i.e., analyzing the non-encapsulated amount of Fe@hepa. No significant differences were observed in the EE% between the samples ($p > 0.05$), while the DL increased five-fold in SALNs-Fe@hepa5 ($p < 0.001$) (Table 2).

Table 2. Encapsulation efficiency (EE%) and drug loading (DL) of SALNs–Fe@hepa.

	EE %	**DL (µg Fe@hepa/mg SALNs-Fe@hepa)**
SALNs-Fe@hepa1	86.6 ± 2.76	5.14 ± 0.01
SALNs-Fe@hepa5	91.5 ± 3.09	26.38 ± 0.70

3.4 In vitro SALNs-Fe@hepa stability

In order to verify the retention of Fe@hepa in SALNs stored as suspension at 4 °C, the spontaneous Fe@hepa sedimentation from SALNs–Fe@hepa was monitored for both the samples for one month after the preparation (t_0). At predetermined time interval, the amount of Fe@hepa separated from the suspension was measured by spectrophotometric method. These data were subtracted from the initial Fe@hepa loading and the results are reported in the graph (Figure 4). The data indicate that SALNs–Fe@hepa5 are more stable compared to the SALNs–Fe@hepa1. Indeed, for this sample, after 4 days, the loss of the cargo was only 4% compared to the initial content, indicating a good stability of the system. Then, a very slow sedimentation rate of free Fe@hepa is observed in the remaining time until a total loss of 6%. On the contrary, SALNs–Fe@hepa1 appeared quite instable in suspension, showing a fast initial loss of cargo corresponding to about 11% in 4 days followed by a slower phase of Fe@hepa release up to a total loss of 20% in one month. Therefore, given the weak stability in suspension of SALNs–Fe@hepa1, this sample was not taken into account in the further experiments.

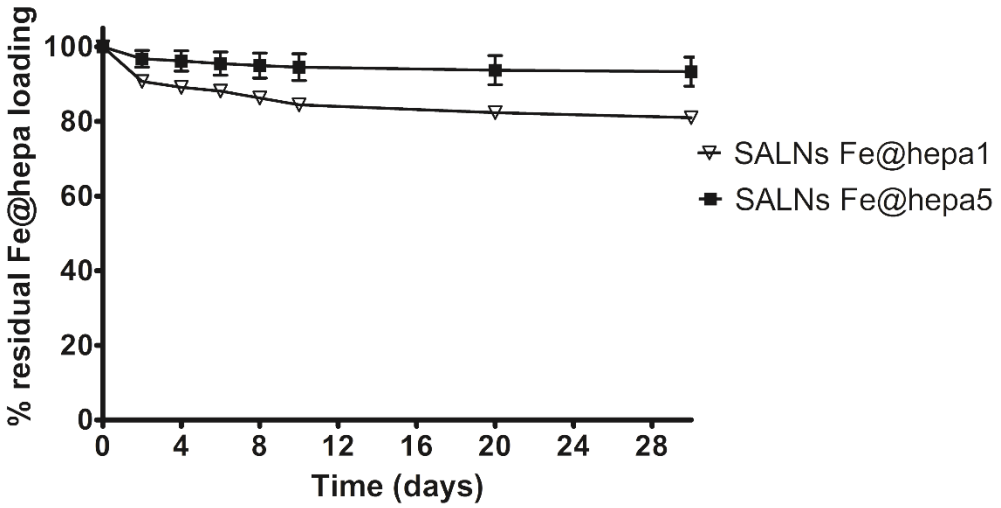

Figure 4. Percentage of Fe@hepa released from SALNs-Fe@hepa1 and SALNs–Fe@hepa5 stored as a suspension at 4 °C for one month, where 100% corresponds to initial SALNs–Fe@hepa drug loading. Error bars indicate standard deviation (SD); where not visible, error bars did not exceed symbol size.

3.5 Stabilization of heparin coating

In order to evaluate if the encapsulation of the Fe@hepa into SALNs was able to stabilize the heparin coating, the leakage of heparin form both naked Fe@hepa and SALNs-Fe@hepa5 was measured in physiologic solution (NaCl 0.9%). Indeed, the heparin shell was stable in water [41] but in the presence of saline medium the interaction between heparin and iron oxide became weaker, resulting in the release of heparin and in the loss of stability of the colloidal

suspension [48]. Therefore, to measure the stability of the coating, experimental conditions with minimal perturbation (saline solution) were considered and the amount of heparin released after only 1 h at room temperature was evaluated. As reported in Table 3, in the case of naked Fe@hepa, as expected, a leakage of about 70% of the initial amount of heparin occurred while in the case of the SALNs–Fe@hepa5 no release of heparin in solution was observed in the time period considered.

Table 3. Evaluation of the amount of heparin released in saline solution from SALNs–Fe@hepa5 and naked Fe@hepa.

	Mass of Fe@hepa (µg)	**Initial amount of heparin in Fe@hepa (µg)**	**% of heparin released in NaCl 0.9 %**
SALNs-Fe@hepa5	810	72.9	0
Fe@hepa	620	55.8	72

3.6 Cytotoxicity assay

In order to determine the in vitro cytotoxicity of SALNs–Fe@hepa5 compared to naked Fe@hepa and unloaded SALNs, the MTT was performed on the intestinal CaCo-2 cell line after different incubation times (2, 4, and 6 h). For each time, various concentrations of SALNs (0.8, 1.2, 1.6, 2 mg/mL) and the respective amount of Fe@hepa (21, 32, 42, 53 µg/mL) were tested and the results are reported in Figure 5. The cytotoxicity of Fe@hepa was always higher than that of the other samples, but the cellular viability never dropped below 74%. Unloaded SALNs showed a higher cell viability with respect to the control, while SALNs–Fe@hepa5 demonstrated an intermediate cell viability between the other two samples. However, significant differences were evident only within unloaded SALNs and the other two samples at the concentration of 2 mg/mL after 2 and 4 h of treatment.

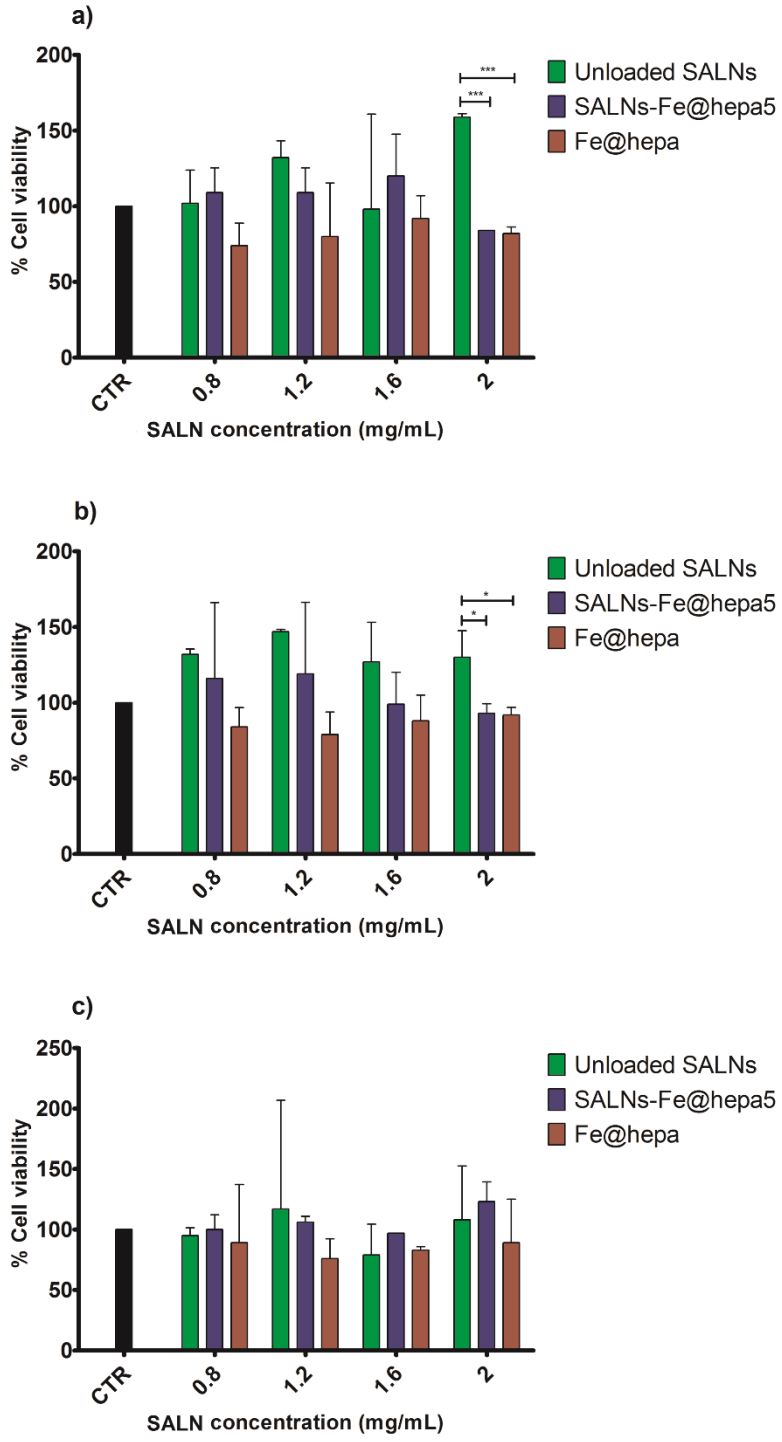

Figure 5. Analyses of cytotoxicity of the samples at different concentrations on CaCo-2 cells (colon rectal adenocarcinoma cell line of human origin) after 2 (a), 4 (b) and 6 h (c) of treatment, using methyl thiazole tetrazolium test (MTT) assay. SALN concentrations of 0.8, 1.2, 1.6, 2 mg/mL correspond to 21, 32, 42, 53 μg/mL of naked Fe@hepa, respectively. Comparison within samples was performed by ANOVA one-way test. Statistical significance levels were defined as: * ($p < 0.05$), *** ($p < 0.001$). Error bars indicate SD; where not visible, error bars did not exceed symbol size.

3.7 Quantification of SALNs–Fe@hepa in the CaCo-2 cell line

Considering the results obtained from the study of cytotoxicity, the concentration of SALNs equal to 2 mg/mL (corresponding to 53 µg/mL of Fe@hepa) is considered optimal to study the internalization of the systems in the CaCo-2 cell line, a colorectal cell line adopted as a model for lymphatic absorption [31,49]. Cells were preventively incubated for 2, 4 and 6 h with naked Fe@hepa and SALNs–Fe@hepa5, washed with PBS and then lysed.

The percentages of iron oxide found in the cell lysate respect to the amount used for the incubation are shown in Figure 6. After two hours of incubation, the percentage of iron oxide present into cell lysate was the same for both the samples (naked Fe@hepa and SALNs–Fe@hepa5). For the other incubation times, iron oxide in cell lysate resulted higher after the treatment with naked Fe@hepa. Moreover, a time-dependent correlation can be noticed: the amount of iron oxide increased with the increasing incubation time. Significant differences can be observed between the samples after 4 and 6 h of incubation ($p < 0.05$).

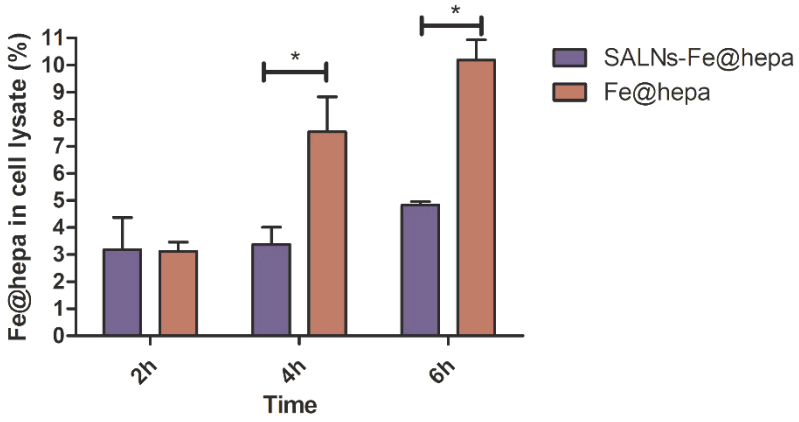

Figure 6. Quantification of iron oxide in CaCo-2 cells after 2, 4 and 6 h of treatment with SALNs-Fe@hepa5 at the concentration of 2 mg/mL (corresponding to 53 µg/mL of Fe@hepa) and naked Fe@hepa at the concentration of 53 µg/mL. A comparison between samples was performed by ANOVA one-way test. Statistical significance levels were defined as: * ($p<0.05$).

In order to visualize the internalization of the sample in the CaCo-2 cell model (Figure 7), confocal laser scanning microscopy analysis was performed. Cellular nuclei were stained in blue, SALNs were labelled in red, while Fe@hepa, owing to their density, were visible as black spots in white-line channel.

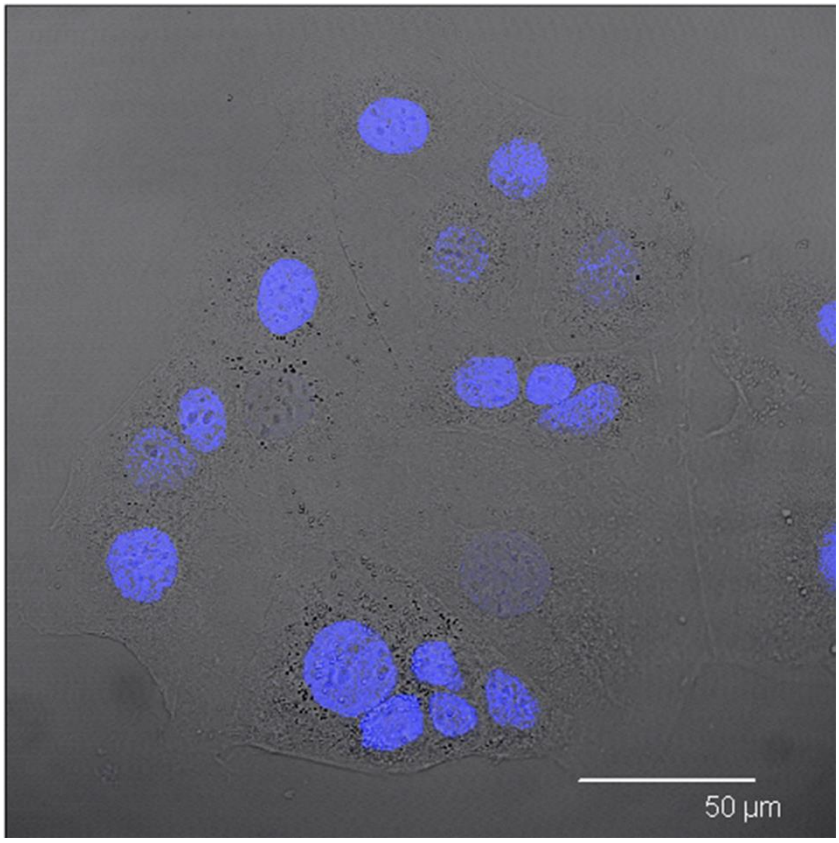

Figure 7. Confocal microscopy image of CaCo-2 cells after nuclei staining with Hoechst.

CaCo-2 cells were treated with Nile red-labelled unloaded SALNs, Nile red-labelled SALNs-Fe@hepa5 and naked Fe@hepa. Figure 8A shows CaCo-2 cells incubated with Fe@hepa. Black spots with different sizes, attributed to clusters of iron oxide nanoparticles, were visible near the cytoplasm but clearly in a different z-thickness compared to the nuclei.

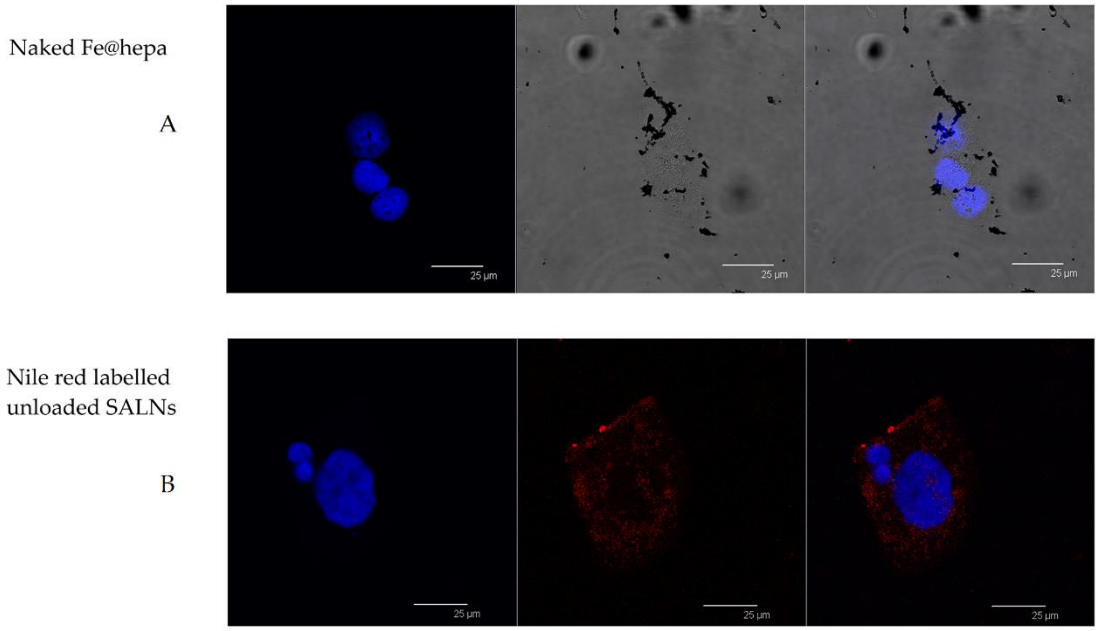

Figure 8. (A) Confocal microscopy images of CaCo-2 cells after nuclei staining and 4 h incubation with naked Fe@hepa. From left to right: blue channel (Hoechst), white-light channel and merged image. (B) Confocal microscopy images of CaCo-2 cells after nuclei staining and 4 h of incubation with Nile red-labelled unloaded SALNs. From left to right: blue channel (Hoechst), red channel (Nile red) and merged image

After incubation with Nile red-labelled unloaded SALNs (Figure 8B), red fluorescence was noticeable around the nuclei of CaCo-2 cells. Red spots are attributable to Nile red-labelled SALNs because no red fluorescence was observed in untreated CaCo-2 cells (Figure 7). The image clearly indicates that SALNs were localized inside the cells because the red fluorescence was located in the area surrounding the nuclei correspondent to the cytoplasm.

After treatment with Nile red-labelled SALNs-Fe@hepa5 (Figure 9), in addition to red spots, it was possible to appreciate, in white-light channel, a grey shading around the nuclei where also red fluorescence was located. Moreover, black spots attributable to Fe@hepa clusters were clearly visible externally to cells revealing the presence of non-encapsulated Fe@hepa, which have tendency to form clusters outside the cells.

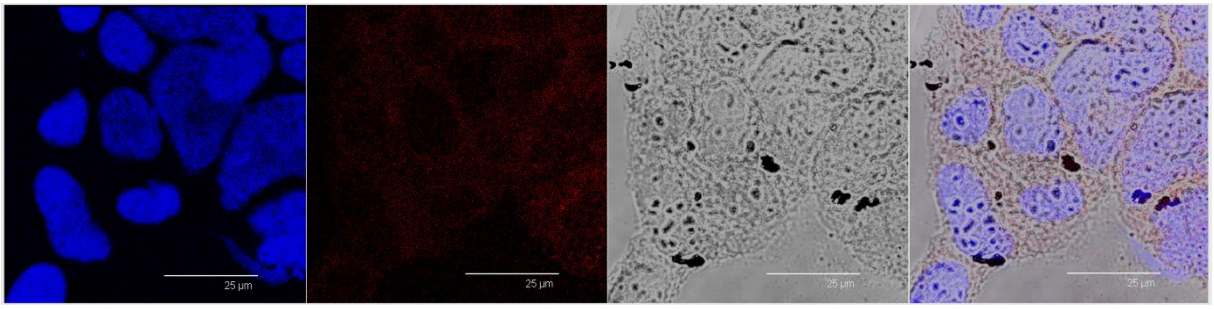

Figure 9. Confocal microscopy images of CaCo-2 cells after nuclei staining and 4h incubation with Nile red-labelled SALNs-Fe@hepa5. From left to right: blue channel (Hoechst), red channel (Nile red), white-light channel and merged image.

4. DISCUSSION

Iron oxide nanoparticles have attracted considerable interest due to their superparamagnetic properties and their potential biomedical applications. The dimensions of these nanoparticles make them ideal candidates for nano-engineering of surfaces to develop non-toxic and biocompatible nanoparticles. Moreover, different coating materials can prevent their irreversible aggregation in aqueous or biological media [50]. Vismara et al. proposed heparin coating as an attractive strategy to achieve a theragnostic aim exploiting anti-angiogenic activity of native heparin [41]. However, this coating is instable in physiological conditions. The goal

of this work was to stabilize Fe@hepa by encapsulation in SALNs, envisaging an oral absorption through a lymphatic route.

SALNs are biocompatible, biodegradable, and can be used as controlled drug delivery and targeting system. Owing to their composition, SALNs possess a structure very similar to that of glyceride-rich chylomicrons which are believed to allow lymphatic transport of drugs into the intestinal lymphatic circulation [51].

It is known that lipid nanoparticles based on triglycerides with a high carbon chain length are less susceptible to intestinal lipase than those composed of a shorter carbon chain and are preferably transported into the intestinal lymphatic system [32,49,52]. For this reason, Geleol™ and Gelucire 50/13® high carbon chain length lipids, both generally recognized as safe and biocompatible materials (manufacturer's information), were selected as the lipid matrix for the SALN preparation. Moreover, these lipids present a low melting point, avoiding the risk of degradation of the drug during the preparation. Gelucire 50/13® is composed of mono-, di-, and triglycerides with mono- and di-fatty acid esters of polyethylene glycol (PEG). Owing to the composition, it exhibits surfactant and solubility enhancing properties that can be exploited to better incorporate lipophilic compounds and to stabilize the lipid nanosystem [53,54]. Moreover, it has been demonstrated that Gelucire® decreases P-glycoprotein efflux, making it a good candidate to gain lymphatic uptake [55,56].

After different formulation attempts, the preparation was optimized to achieve a reproducible and stable colloidal suspension without an observed particle dimensional change when Fe@hepa were encapsulated in the lipid matrix. The average diameter (around 180 nm) and the lipid nature of the particles make this system potentially suitable for intestinal lymphatic uptake associated with chylomicrons synthesized within enterocytes [23,27]. Alternatively, large molecular weight drug-carrier constructs may be selectively taken up intact via the lymphatic system because their large size favor the uptake via the leakier structure of the lymphatic vessels, as compared to blood capillaries [57]. The size of the particles suitable for this pathway is a controversial matter [58]. However, it is recognized that the minute size of this formulation enables efficient uptake into the intestine, particularly via the lymphatic route, favored by particles between 20 and 500 nm in diameter [30].

Regarding the zeta potential, unloaded SALNs measured slightly negative (−16 mV), and became progressively more negative with increasing amounts of Fe@hepa. Considering that Fe@hepa are strongly negative (about −61 mV) due to the presence of heparin coating, the more negative surface charge observed for SALNs–Fe@hepa with respect to unloaded SALNs

can be attributable to a portion of Fe@hepa next to the SALN surface as observed in the STEM pictures (Figure 2C,D).

Morphological studies were performed to better understand the nanoparticle structure. The images obtained by SEM modality on the dried samples confirmed that the structure of the system is solid due to the lipid core made of solid components (Gelucire 50/13® and Geleol™), as can be seen in Figure 2A. However, the SEM modality does not allow the observation of particle contour due to the poor resolution under low-voltage operating conditions (5 kV). Thus, pictures of SALNs in suspension were obtained in STEM modality, highlighting a rough surface structure probably due to the presence of a mixture of the two lipids in the particle matrix. In Figure 2D, at high magnification, it is possible to observe black spots, attributable to Fe@hepa. The clusters of Fe@hepa appeared surrounded by the lipid matrix and the presence of Fe@hepa nanoparticles located in a peripheral position in the SALNs were also visible (Figure 2C,D). The presence of Fe@hepa close to the surface of the particles might explain the negative Z-potential value noticed for SALNs–Fe@hepa5. In addition, this finding was in agreement with EDX analysis that showed the superficial elemental composition of the particles. Indeed, EDX study demonstrated the clear presence of iron in the spectrum of SALNs−Fe@hepa (Figure 3A) while no iron signal was evident in the spectrum of unloaded SALNs. On the other hand, the incorporation of Fe@hepa into the lipid matrix, as observed by electronic microscopy, should lead to a stabilization of the heparin coating. To confirm if this goal was achieved, the release of heparin from the system in physiologic solution was evaluated comparing naked Fe@hepa and SALNs–Fe@hepa. The results (Table 3) showed that no heparin was released from the SALNs–Fe@hepa sample, indicating that the encapsulation of Fe@hepa inside SALNs is a good strategy to avoid the loss of heparin coating occurring for the naked Fe@hepa. Indeed, heparin, selected as an iron oxide coating for its antiangiogenic features in tumor environments [42–44], was linked to the particle surface by ionic bonds between the positive iron oxide core and its negative chain. Therefore, Fe@hepa were destabilized in biological isotonic fluid where the electrostatic interaction between iron oxide and heparin became weaker. On the other hand, when Fe@hepa were surrounded by lipid matrix, the interaction with the biological fluids is avoided and no leakage of heparin occurs.

To better understand the potential of Fe@hepa–loaded SALNs, the particles were prepared using two different dosages (1 or 5 mg). The analyses indicated that in both SALNs–Fe@hepa samples the percentage of Fe@hepa incorporated was around 90%. This means that, increasing the initial loading, the encapsulation efficiency remained stable, suggesting that using only 1 mg of Fe@hepa the loading capacity of the lipid system was far from saturation. As evidence

of this, increasing the initial amount of drug by five-fold, the loading increased proportionally from 5.14 μg/mg to 26.4 μg/mg (Table 2). However, during storage it was possible to notice a progressive sediment of Fe@hepa, indicating a probable desorption of Fe@hepa nanoparticles from the system. For this reason, the stability of SALNs–Fe@hepa samples was monitored for one month after the preparation (Figure 4). The data indicated that during one month, the higher loaded sample (SALNs–Fe@hepa5) was by far more stable than the less loaded sample (SALNs–Fe@hepa1). It can be assumed that in both the cases, the initial rapid loss of cargo was probably due to Fe@hepa non-embedded inside the lipid matrix or highly dispersed in the suspension. Afterwards, a release of Fe@hepa with a slower rate was observed; this was attributed to a leakage of Fe@hepa owing to its high density and to the magnetic forces between iron oxide nanoparticles. The results indicated clearly that the loss of Fe@hepa was larger for the lower loaded sample (SALNs–Fe@hepa1). To explain this finding, it can be assumed that when high amounts of Fe@hepa were embedded in the lipid matrix, the forces of attraction within Fe@hepa clusters were prevalent, stabilizing the cargo. On the contrary, when poor amounts of Fe@hepa were loaded, the forces of attraction of the clusters inside the particles were weaker in respect to the attraction of the non-embedded particles, leading to a progressive leakage of the cargo. For this reason, all subsequent studies on cells were conducted using only the most loaded and stable sample (SALNs–Fe@hepa5).

The MTT assay on CaCo-2 cells was performed after different times of exposure (2, 4, 6 h) to compare the cytotoxicity induced by unloaded SALNs, naked Fe@hepa, and SALNs–Fe@hepa5. The CaCo-2 cell line was used because it has been reported to be an indirect indication of intestinal lymphatic transport [31,49]. The results of the analyses indicated that the lipids used to develop SALNs were not toxic but, on the contrary, they seemed to improve the cell viability as the percentage of cell vitality observed after the treatment with unloaded SALNs resulted equal to or higher than the control (Figure 5). Only a slight cytotoxicity was observed for naked Fe@hepa since cell viability, at the experimental conditions adopted, never dropped below 74% compared to the control. Cytotoxicity studies reported in the literature and conducted on naked iron oxide nanoparticles demonstrated that these systems induce a reduction of cell viability depending on their coating, time of exposure, concentrations and cell type evaluated [59–61]. Thus, the results obtained in this work demonstrated that the coating with heparin allowed biocompatible and non-toxic nanoparticles to be obtained. The cytotoxicity of SALNs–Fe@hepa fell in the middle between that of unloaded SALNs and Fe@hepa at all concentrations and incubation times considered, probably because the partial negative effects of Fe@hepa were compensated by the positive effect of unloaded SALNs.

Therefore, it is possible to conclude that all the samples, at all the concentrations tested, did not exhibit toxicity on CaCo-2 cell model and the results indicated that the cytotoxicity is neither time- nor concentration-dependent. For this reason, to carry out the studies regarding the ability of the particles to enter the CaCo2 cells, the highest concentration (cell viability more than 80%) has been selected and therefore all the experiments were conducted using the concentration of 2 mg/mL.

The ability of the particles to enter in CaCo-2 cells was evaluated by measuring the amount of iron transported in the cells by the two systems (Fe@hepa and SALNs-Fe@hepa5). The results (Figure 6) indicated that the amount of iron found in the cells was higher for the cells incubated with naked Fe@hepa respect to cells incubated with SALNs–Fe@hepa, especially for longer incubation times. These findings seem to be in contrary to expectations because in the literature SALNs resulted able to improve the internalization of drugs thanks to their composition [25–27]. However, it is important to notice that the higher percentage of iron found in the cells treated with Fe@hepa might be due to the precipitation of naked iron oxide on the bottom of the wells, because of the loss of the heparin coating in biological fluids. Indeed, during the experiments, it was observed that in the case of cells treated with naked Fe@hepa, dark spots attributable to iron remained attached to the well bottom, even after the washing with PBS (see Section 2.11). On the contrary, in the case of cells incubated with SALNs–Fe@hepa5, the non-internalized particles were easily removed with washing owing to the low density of their lipid composition. As a result, in the case of cells treated with Fe@hepa an overestimation of Fe@hepa associated with the cells might have occurred.

In order to support this assumption, confocal laser scanning microscopy analysis was performed using Nile red as a probe to visualize SALNs in the red channel, while no probe was used for Fe@hepa since their clusters appeared as dark spots by observation in white-light channel. Observing the cells treated with Fe@hepa, the dark spots attributed to the Fe@hepa clusters seemed to be localized in a different z-thickness compared to nuclei, indicating that they were not internalized by CaCo-2 cells (Figure 8A). This observation indicated that iron clusters had not entered the cells, giving evidence of the overestimation of Fe@hepa associated with the cells. On the contrary, both unloaded SALNs and SALNs–Fe@hepa5 seemed to be internalized in the cells because a slight red fluorescence was noticeable around the nuclei, highlighting that the particles were localized in the cytoplasm. However, the iron particles embedded in the SALNs were not visible, probably owing to their small dimension even thought they could be considered responsible of the grey shading visible around the nuclei (Figure 9). On the other

hand, regarding the black spots visible outside the cells in the image of cells incubated with SALNs–Fe@hepa, they could be attributable to Fe@hepa not embedded in the lipid matrix but only absorbed on the surface or highly dispersed in the suspension according to what was observed in the in vitro stability studies (Figure 8).

5. CONCLUSIONS

In this work it was demonstrated that SALNs are an efficient carrier for Fe@hepa, reducing their cytoxicity to CaCo-2 cells and overcoming the loss of heparin coating in biological fluids. SALNs–Fe@hepa resulted able to be efficiently internalized in CaCo-2 cells, and demonstrated to be a promising tool for delivering the theragnostic Fe@hepa to lymphatic circulation by the oral route, although further studies are needed to comprehend the potential in vivo applications. Moreover, it would be interesting in the future to replace native heparin with low-molecular-weight heparins, which showed a less anticoagulant activity while maintaining antiangiogenic activity, in order to reduce risks of bleeding.

Chapter 2

Drugs/lamellae interface influences the inner structure of double-loaded liposomes for inhaled anti-TB therapy: An in-depth small-angle neutron scattering investigation

Eleonora Truzzi [1], Fiorella Meneghetti [2], Matteo Mori [2], Luca Costantino [1], Valentina Iannuccelli [1], Eleonora Maretti [1], Fabio Domenici [3], Carlo Castellano [4], Sarah Rogers [5], Angela Capocefalo [6], Eliana Leo [1]

[1] Dipartimento di Scienze della Vita, Università degli Studi di Modena e Reggio Emilia, via Campi 103, 41121 Modena, Italy

[2] Dipartimento di Scienze Farmaceutiche, Università degli Studi di Milano, Via L. Mangiagalli 25, 20133 Milano, Italy

[3] Dipartimento di Scienze e Tecnologie Chimiche, Via della Ricerca Scientifica, Università degli Studi di Roma Tor Vergata, 00133 Roma, Italy

[4] Dipartimento di Chimica, Università degli Studi di Milano, via Golgi 19, 20133 Milano, Italy

[5] ISIS-STFC, Rutherford Appleton Laboratory, Harwell Oxford, Didcot OX11 0QX, UK

[6] Dipartimento di Fisica, Sapienza Università di Roma P. le Aldo Moro 5, 00185 Roma, Italy

The majority of this chapter is directly copied or modified with publishing rights from Journal of Colloid and Interface Science **2019**, 541, 399-406; doi: 10.1016/j.jcis.2019.01.094

ABBREVIATIONS

API: active pharmaceutical ingredient

Chol: cholesterol

D_2O: deuterium oxide/deuterated water

DL: drug loading

EE: encapsulation efficiency

INH: isoniazid

Mtb: mycobacterium tuberculosis

PC: phosphatidylcholine

PCS: photon correlation spectroscopy

PDI: polydispersity index

Q: momentum transfer/scattering vector

RIF: rifampicin

SANS: small-angle neutron scattering

SLD: scattering length density

SLF: simulated lung fluid

TB: tuberculosis

1. INTRODUCTION

Tuberculosis (TB) is one of the world's deadliest communicable diseases [62]. Since Mycobacterium tuberculosis (Mtb) tends to localize in the lungs, the administration of therapeutic agents through the pulmonary route could be a valid strategy to improve the efficacy of drugs, as it allows the deposition of the active pharmaceutical ingredient (API) directly at the infection site, avoiding first-pass metabolism and reducing systemic side effects. Recently, liposomes have been proposed as new drug delivery carriers for inhalation therapy, to improve drug targeting and delivery [63,64]. The success of targeting alveolar macrophages depends critically on the chemico-physical characteristics of the nanocarriers, namely their size, shape, density, porosity, surface charge and presence of specific molecules involved in the receptor-mediated endocytosis [63,65]. Rifampicin (RIF) and isoniazid (INH), two powerful first-line anti TB drugs provided with a very different water solubility (INH LogP −0.64 and RIF LogP 3.719) [66,67], were here chosen as drug models for co-loading experiments, using conventional liposomes prepared with phosphatidylcholine (PC) and cholesterol (Chol). Considering the liposomal architecture, both the hydrophilic INH and the hydrophobic RIF were encapsulated within the nanoparticle, as they could interact with its different components, namely the lipid bilayers (RIF) and the central aqueous core (INH) [68]. Therefore, it was conceivable that these drugs could be located inside the liposomal formulations, as depicted in the model shown in Figure 1.

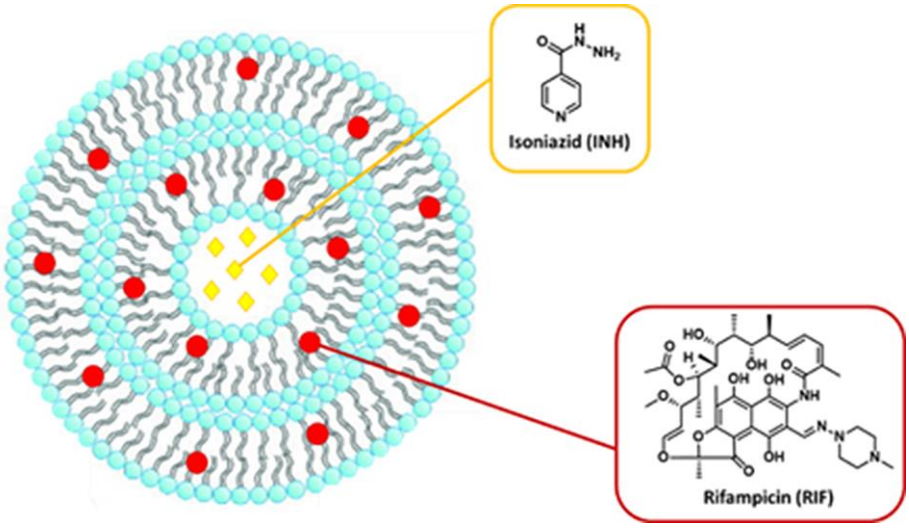

Figure 1. Multi-lamellar liposome representation showing the hypothesized localization of RIF and INH within its structure.

Taking into account that the co-administration of RIF and INH (Rifinah®) improves the outcomes in TB patients, we co-loaded these two drugs in the same formulation for pulmonary

delivery. Following this approach, these nanocarriers may acquire better pharmacokinetic properties, thus ensuring greater efficacy [69]. This strategy could also be conveniently applied for the administration of non-traditional antitubercular agents, targeting new druggable molecular pathways [70–72], with the aim of tackling the growing incidence of drug resistant infections [73]. In addition, the formulation of carriers, shipping high amounts of drugs, generally improves patient compliance and reduces systemic adverse effects.

In order to fully address these issues, an in-depth characterization of the nanocarriers is of critical importance for optimizing the loading conditions. Among the available techniques, small-angle neutron scattering (SANS) has recently emerged as a powerful tool to investigate amphiphilic aggregates, such as uni-lamellar and multi-lamellar vesicles [74]. In particular, SANS provides crucial information about the arrangement and behavior of the drug into the nanoparticle after its encapsulation and allows the analysis of these systems at nanometric level. This technique yields valuable and unique data about steric bilayer thickness, particle dispersion and the finer structural features. In detail, it is possible to determine: the core radius (r_c), the shell thickness (t_s), the shell scattering length density (SLD, ρs), the water layer thickness (t_w), the water scattering length density (SLD, $\rho 0$), the number of layers (N) and the overall liposome size (see Figure 2) [75].

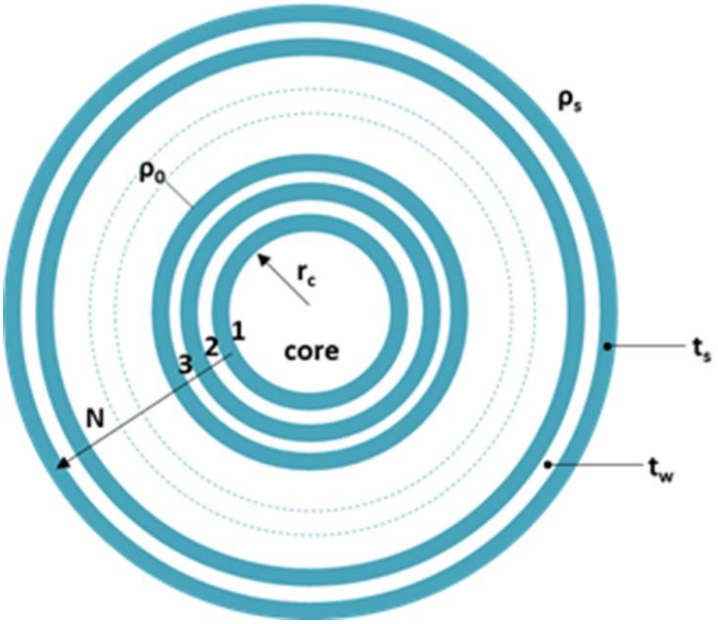

Figure 2. Multi-lamellar model of liposome showing the main parameters determined by SANS.

Therefore, we decided to apply this technique on liposomes co-loaded with RIF and INH, comparing this formulation with mono-loaded liposomes, in order to deeply characterize the structure of the carrier and any perturbation induced by the presence of these drugs, under

physiological conditions and without any earlier manipulation [76]. We complemented this SANS study with Photon Correlation Spectroscopy (PCS) analysis and drug release studies, in order to obtain key information on our new host-guest structures, for a synergistic and site-specific antitubercular therapy.

1.1 SANS TECHNIQUE

SANS is an advanced structural characterization method not fully employed in nanomedicine yet. The basic principles of SANS are similar to those of small-angle X-ray scattering and light scattering, but being generated by neutrons it provides unique information regarding drug delivery system structure.

The employment of such characterization techniques for the study of nanovectors is essential in order to determine shape and size of nanoparticles and the influence of the addition of drugs on their structure. Indeed, structural issues are noteworthy to control the mechanism of action of nanovector.

SANS can be applied to the study of large-scale structure, between 1 and 450 nm in size (10 – 4500 Å), such as proteins, drugs, polymers, membranes, surfactants, colloids and nanoparticles. It is different from the other techniques due to the use of neutrons. Neutrons are neutral subatomic particles, and their neutrality guarantees a deep penetration into the matter. Moreover, neutrons interact with atomic nuclei and they are scattered in a different way depending on the type and mass of the nucleus. Applying SANS to the study of macromolecules, the overall scatter of a molecule depends on the scatter of all its components. The scattering power of a molecule (or nucleus) is called scattering length density (SLD). In particular, the SLDs of hydrogen and deuterium (two isotopes) are quite different, generating huge differences in the scattering intensity. Taking advantage of this behavior of neutrons, the use of deuterated solvents increases the contrast between the studied system and the environment, without changing its properties.

This peculiarity makes the SANS technique unique and guarantees its applicability for an in-depth study of drug delivery systems.

The instrument

To perform SANS measurements a small-angle neutron scattering diffractometer is required. First of all, a neutron source is necessary in order to generate neutrons. They can be originated by two different mechanism: the nuclear fission and the spallation process. Once generated, the

neutrons with the required wavelength are selected in the energy (or velocity, in some setups) selector, also called monochromator. Then, the collimator is able to filter a stream of neutrons in order to select only those traveling parallel to a specified direction are allowed through. Finally, the screened neutrons hit the sample and the scattered neutrons are recorded by a detector. The detector can be moved inside the evacuated tube nearer or farther from the sample, in order to "capture" the small-angle scattered neutrons.

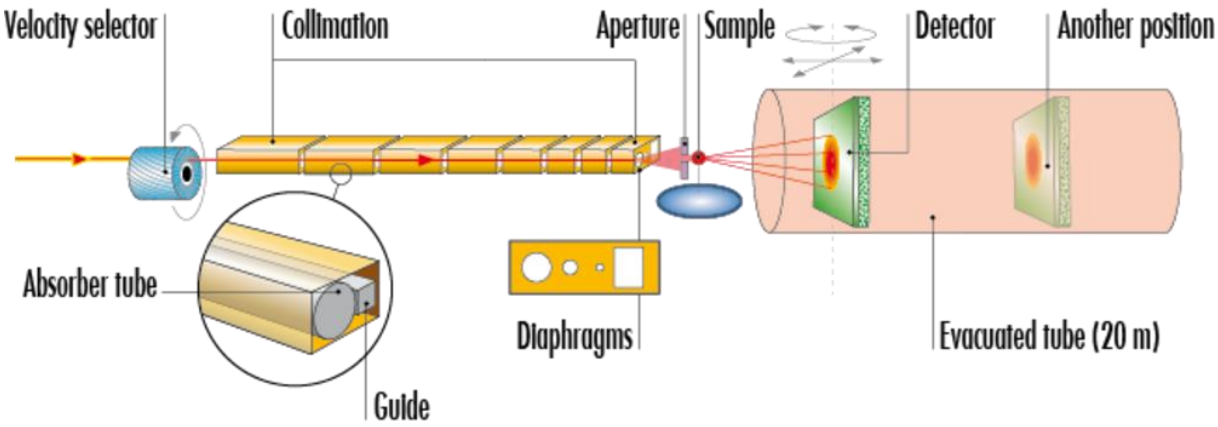

Figure 3. Small-angle neutron scattering diffractometer [77].

Basic principle

The central hypothesis of quantum mechanics is that all matters can exhibit both a particle- and wave-like behavior. In 1924, de Broglie demonstrated that neutrons behave as a wave when moving with a constant velocity. In neutron scattering, the wave nature of a neutron is generally expressed as a wave vector, k:

$$k = \frac{2\pi}{\lambda}$$

where λ is the wavelength.

When a neutron hits a molecule, it is scattered with a scattering angle 2ϑ thus determining a momentum transfer q (also called scattering vector), as illustrated in Figure 4.

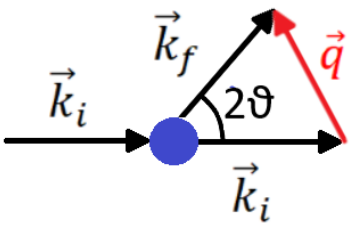

Figure 4. Illustration of the scattering process with the incoming (k_i) the outcoming (k_f) vectors and the scattering vector q.

Therefore, the scattering vector can be calculated by the following equation:

$$Q = |\vec{Q}| = |\overrightarrow{k_f} - \vec{k}_i| = \frac{4\pi}{\lambda} \sin\theta$$

Being k_f and k_i equal in the modulus, the scattering vector results as a sum of the two vectors. By recording the intensity of the scattering as function of the modulus of the scattering vector q, it is possible to obtain the scattering curves. However, the scattered neutrons can derive not only from the sample, but also from the solvent, the analysis cuvettes and other molecules present in the sample. Therefore, a subtraction of the background given by all the unrequired contributions is needed.

In nanomedicine field, where complex compounds are organized in nanostructures, the neutron scattering is not given by an atom, but by an entire molecule which has its own SLD (ρ):

$$\rho = \sum_i N_i b_i$$

where we sum the scattering length contributions (b_i) from the N atoms within the volume material. Therefore, each component of the nanosystem has its own SLD which can be calculated, permitting to identify its scattering contribution in the whole signal. Since nanoparticles are complex colloids, the neutron scattering derived is given by different aspects, such as shape, size, and molecular interactions. The scattering intensity as function of the modulus of q is given by the following equation:

$$I(Q) = \frac{N}{V} V^2 (\Delta\rho)^2 P(Q) S(Q) + B$$

Where N/V and V are the density and the volume of the scattering bodies respectively, P(Q) is the shape factor, S(Q) the interbody structure factor (intermolecular interactions), Δρ is the so-called "contrast factor" and B the background signal.

By fitting the experimental scattering curves obtained by SANS analysis with the equation above, information regarding shape, size and intermolecular interactions can be obtained, thus recreating the structure of the nanosystem.

Morphologies	P(Q)	Morphologies
Spheres (radius: R)	$\frac{9}{(QR)^6}[\sin(QR) - QR\cdot\cos(QR)]^2 = A^2_{sph}(QR)$	
Spherical shells (outer radius: R_1 inner radius: R_2)	$\frac{[R_1^3\cdot A_{sph}(QR_1) - R_2^3\cdot A_{sph}(QR_2)]^2}{(R_1^3 - R_2^3)^2}$	
Triaxial ellipsoids (semiaxes: a,b,c)	$\int_0^1\int_0^1 A^2_{sph}[Q\sqrt{a^2\cos^2(\pi x/2) + b^2\sin^2(\pi x/2)(1-y^2)_1 + c^2y^2}\,]\,dx\,dy$	
Cylinders (radius: R length: L)	$4\int_0^1 \frac{J_1^2[QR\sqrt{1-x^2}\,]}{[QR\sqrt{1-x^2}\,]^2}\,\frac{\sin^2(QLx/2)}{(QLx/2)^2}\,dx$ $J_1(x)$ is the first kind Bessel function of order 1	
Thin disk (radius: R)	By setting L = 0 $\quad \frac{2 - J_1(2QR)/QR}{Q^2R^2}$	
Long rod (length: L)	By setting R = 0 $\quad \frac{2}{QL}\int_0^{QL}\frac{\sin(t)}{t}\,dt - \frac{\sin^2(QL/2)}{(QL/2)^2}$	

Figure 5. Examples of different equations which represent different morphologies [78].

As mentioned before, the advantage of SANS technique is related to the SLD of different atoms. In particular, the isotope of hydrogen (H), deuterium (D), presents a completely different scattering power respect to H. Therefore, by using deuterated water (D_2O) or deuterated materials, a contrast factor can be obtained, increasing the contrast between the solvent and the materials, or increasing the contrast between two different materials inside a particle (*e.g.* drug embedded in a particle and matrix).

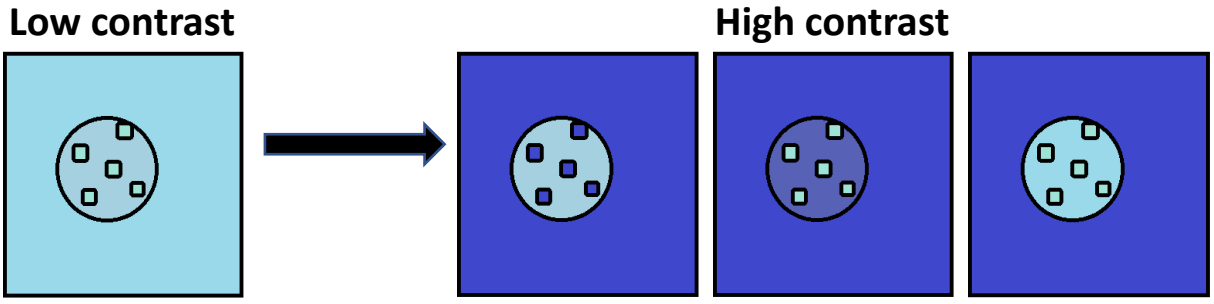

Figure 6. Representation of different contrast which can be obtained by using D_2O or deuterated materials.

Why is it called "small-angle"?

The scattering angle 2ϑ (and the corresponding Bragg's angle ϑ) is related to the dimensions of the scattering center (molecule, atom, particle…) in Bragg's law:

$$\lambda = 2d\sin\theta,\ d = \frac{\lambda}{2\sin\theta}$$

By substituting λ as a function of q, the direct relation between the scattering vector and the scatterer dimension can be obtained:

$$d = \frac{2\pi}{q}$$

Being d and q inversely proportional, to analyze colloids around 450 nm, low q values are required. Thus, being q proportional to the scattering angle 2ϑ and then to ϑ, this technique takes advantage of the possibility to move the detector at high distance from the sample, leading to record scattered neutrons at low ϑ.

2. MATERIALS AND METHODS

2.1 Materials

Cholesterol (Chol, ≥99%) was purchased from Sigma Aldrich (St. Luis, MO, USA), phosphatidylcholine (PC, 95%) from Egg yolk was obtained by Fluka Chemie (Buchs, Switzerland). Rifampicin (RIF, Lot. No 17447/BR, purity calculated according current Ph. Eur.: 97-102%) was a kind gift from Sanofi (Brindisi, Italy), while Isoniazid (Isonicotinic Acid Hydrazide, INH, 98.0%) was purchased from T.C.I Europe (Zwijndrecht, Belgium). Finally, deuterium oxide (D_2O, Lot. 170009, 99.96%) was purchased from VWR (Milan, Italy). All solvents employed were of analytical grade.

2.2 Liposome preparation

Liposomes were prepared using the Reverse Phase Evaporation (REV) technique and homogenized using an Ultra-Turrax device (Ika-euroturrax T 25 basic, IkaLabortechnik, Staufen, Germany) [79].

Cholesterol (Chol) and phosphatidylcholine (PC) with fixed molar ratio (1:1) were weighed and solubilized in chloroform at the final concentration of 40 mM. The obtained solution was placed into a glass flask, and the solvent was removed under vacuum at room temperature until the formation of a dry film (Buchi HB-140, Buchi, Swiss). The phospholipid film was re-dissolved in diethyl ether and mixed with water (3:1 ratio). This suspension was vortexed to form a W/O emulsion; than the emulsion was stirred for 2 hours at 200 rpm to remove the organic solvent, inducing the phase reversal and, finally, the formation of liposomes (MLV). Liposomes were homogenized by Ultra-Turrax (Ika-euroturrax T 25 basic, IkaLabortechnik, Staufen, Germany)

for 3 minutes and purified by dialysis for 30 minutes in order to separate the free drugs before being stored at +4 °C in vials. For loaded liposomes, RIF:lipid (w/w) ratios of 3:100, 6:100, 12:100 (for RIF 3%, 6%, 12% samples, respectively) were used, adding the drug to the chloroform solution along with the lipids; for INH-loaded liposomes 15:100, 30:100, 60:100 drug:lipid (w/w) ratios were employed (for INH 15%, 30%, 60% samples, respectively), adding INH to the water phase mixed with diethyl ether. For the preparation of liposomes encapsulating INH and RIF (Co-loaded liposomes), a RIF:INH:lipid (w/w) ratio of 12:15:100 was employed. For SANS analysis, liposomes were prepared and purified using D_2O instead of milliQ water.

2.3 Photon Correlation Spectroscopy (PCS)

Liposome size and polydispersity index (PDI) were determined by photon correlation spectroscopy (PCS) technique using a Zetasizer Nano ZS analyzer system (Zetasizer version 6.12; Malvern Instruments, Worcs, U.K.). The results were expressed as the average of three different measurements.
Analysis was performed in triplicate and each measurement was averaged over at least 12 runs.

2.4 Drug loading and Encapsulation Efficiency

The drug loading (DL %) and the encapsulation efficiency (EE %) of loaded-liposomes were evaluated by UV-visible spectroscopy (Lambda 3B Perkin-Elmer, Wotham, USA). For the determination of the hydrophilic drug (INH), 300 µL of liposomal suspension was dissolved in 1.5 mL of isopropanol and this solution was diluted with MilliQ water. The amount of incorporated INH was determined in the solution by recording the absorbance at $\lambda = 262$ nm. In the same way, for the determination of RIF, 300 µL of liposomal suspension was dissolved in 1.5 mL of isopropanol and this solution was diluted with methanol. The amount of incorporated RIF was determined by recording the absorbance at $\lambda = 475$ nm.
The absorbance of the solutions containing the drugs was converted to the amount of drug by preparing standard calibration curves constructed using supernatants of the corresponding unloaded liposomes (n = 6), in order to eliminate any possible interference in the measurements. The direct quantification of drug amounts in co-loaded liposomes using UV-visible spectroscopy cannot be performed, since INH absorption spectrum is overlapped to that of RIF [80]. For this reason, to determine INH peak-to-peak first-order derivative, UV spectroscopy was employed. Gürsoy *et al*. demonstrated the reliability of derivative UV spectrophotometry

for the simultaneous estimation of RIF and INH, avoiding the interference problem related to spectral overlap at 262 nm [81].

DL % and EE % were calculated with the following equations:

$$DL\ \% = \frac{incorporated\ drug\ (mg)}{total\ mass\ of\ liposomes\ (lipids\ and\ drug)} * 100$$

$$EE\ \% = \frac{incorporated\ drug\ (mg)}{amount\ of\ drug\ added\ (mg)} * 100$$

The method to determine the amount of RIF and INH in liposomes has been validated by using unloaded liposomes spiked with known quantities of drugs.

2.5 Drug release studies

The *in vitro* release of RIF and INH from liposomes was analyzed in Simulated Lung Fluid (SLF) at pH 7.4 [82]. Briefly, 1 mL of liposome suspension placed in a semipermeable membrane (Dialysis Tubing - Visking MWCO-12-14000 Daltons, Medicell International Ltd, London) was immersed into a vessel containing 30 mL of SLF medium and maintained at 37 ± 0.5 °C under gentle stirring. At fixed time intervals, aliquots (1 ml) were withdrawn from the solution and INH and/or RIF content was determined by spectrophotometry, as previously described (Lambda 35). Two aliquots were analyzed for each time point using unloaded liposomes as blank and the study was performed in triplicate.

2.6 SANS experiment

Nanoparticles characterization was undertaken using the fixed-geometry, time-of-flight small angle neutron scattering Sans2d instrument at the ISIS Spallation source at the Rutherford Appleton Laboratory, U.K.

A scattering vector $q = (4\pi/\lambda) \sin(\theta)$ (where λ is the neutron wavelength and 2θ is the scattering angle) range between 0.001 and 0.5 $Å^{-1}$ was obtained by using neutron wavelengths spanning from 2.2 to 10 Å, with a sample–detector distance of 4 and 12 m.

The samples were contained in 2 mm path length, UV-spectrophotometer grade, quartz cuvettes and mounted on aluminum holders on top of an enclosed, computer-controlled, sample chamber. Temperature control was achieved by using a thermostated circulating bath pumping fluid through the base of the sample chamber, achieving a temperature stability of ± 0.2 °C. The

experiments were run at 25 °C using 0.6 mL volume samples in quartz cuvettes (Hellma, GmbH). To maintain the degree of purity of D_2O and avoid phenomena of deuterium chemical exchange, the SANS measurements were performed in controlled hermetic conditions.

All scattering data were (a) normalized for the sample transmission, (b) background corrected using a quartz cell filled with the solvent used (D_2O), and (c) corrected for the linearity and efficiency of the detector response (component of the instrumental smearing) using the instrument specific software package [83]. The experimental time of a single measurement was between 30 and 60 minutes.

The experimental data were analyzed using the multi-shell spherical model of the fitting routine SASView 2.2.0, in the context of a spherical core-shell morphology.

SANS experiments were carried out to quantify the specific type of aggregated system (observed by the previous techniques), in terms of shape and size characteristics. The scattering intensity detected by this technique contains intra-particle information (size, shape) and inter-particle information (interactions between the scattering centers of the aggregated systems) in solution (eqn (1)),

$$I(q) = N_p V_p^2 \Delta\rho^2 P(q) S(q) + B \qquad (1)$$

where N_p is the number of scattering particles per unit volume, V_p is the volume of one scattering particle, $\Delta\rho$ is the difference in scattering length density (SLD) in the system (known as contrast), P(q) is the form factor and gives intra-particle information (size and shape), S(q) is the structure factor and gives inter-particle information (particle interactions), B is the background signal.

According to the employed model [84], the scattering intensity of non-interacting (S(q) ~ 1) multilamellar vesicles is given by the formula:

$$I(q) = \frac{\Phi}{V(R_N)}(\rho_S - \rho_0)^2 \left[\sum_{i=1}^{N} 3V(r_i)\frac{\sin(qr_i) - qr_i\cos(qr_i))}{(qr_i)^3} - 3V(R_i)\frac{\sin(qR_i) - qR_i\cos(qR_i))}{(qR_i)^3}\right]^2 \qquad (2)$$

where Φ is the volume fraction of the particles in solution, R_N is the total radius of the multilamellar liposome containing N layers, $V(r)$ is the volume of a sphere with radius r, ρ_S is the shell SLD, ρ_0 is the solvent SLD, , $r_i = r_c + (i-1)(t_s + t_w)$ with r_c water core radius and t_s and t_w thickness of the lipid layer and of the solvent, respectively; $R_i = r_i + t_s$. The size $2R_N$ of the multilamellar vesicles is calculated from the values of the parameters extrapolated from the best fits of the SANS curves according to the formula $2R_N = 2r_C + N \cdot 2t_s + (N-1) \cdot 2t_w$.

In the fitting procedure and data analysis, the following foresights have been employed: (a) a polydispersity (PDI) following a Gaussian distribution has been considered for the structural parameters r_c, t_s and t_w; (b) the SLD values ρ0 and ρs (with default scale was 1 and background 0.02 cm^{-1}) were initialized according to literature [85] and optimized in the fitting procedure in order to evaluate SLD changes attributable to the presence of the drugs, both in the water and in the lipid layers; (c) the fit quality was determined by the reduced χ^2 value, which is reported in the caption of the corresponding Figures. Neither aggregation processes nor appearance of precipitate were revealed by visual inpection. In this respect, the SANS measurement was repeated twice to ensure that the system was effectively at equilibrium.

Due to the huge difference in the coherent scattering lengths of deuterium and hydrogen, the D_2O/H_2O contrast variation SANS methodology allows a well distinguished scattering from the shell with respect to the corresponding inner content. Therefore, by using D_2O in the external phase of the liposomal system, we gained information on the morphology and structure of the lipid shell correlated to the loaded drug placement.

2.7 Statistical analysis

Statistical analysis was performed using the one-way analysis of variance (ANOVA). The data are represented as means ± SD. Differences were considered statistically significant at p-values less than 0.05 (*p<0.05; **p<0.01; ***p<0.005).

3. RESULTS

3.1 Liposome characterization

Data of size, polydispersity index (PDI), determined by PCS analysis, encapsulation efficiency and drug loading of the analysed liposomes are shown in Table 1.

No significant size differences could be appreciated between the drug-loaded liposomes and the unloaded samples. With respect to particle size distribution, the polydispersity index (PDI), used to define the degree of homogeneity of a size distribution of particles, is a parameter given by the Zeta sizer analyzer System. Generally, a PDI of 0.3 and below is considered to be acceptable for drug delivery systems and indicates a monomodal distribution of vesicles [86]. Regarding this value, we observed that if we increased the amount of RIF from 3 mg to 12 mg, a PDI increment from 0.283 to 0.440 followed. With respect to INH-loaded liposomes, differences neither in size nor in PDI values could be appreciated in the differently concentrated

drug-loaded samples. Finally, the co-loaded sample presented the same size and intermediate PDI value as compared to the homologous single loaded samples.

Concerning encapsulation efficiency, UV-vis spectroscopy analysis indicated that about 50% of both the drugs were incorporated in each sample, regardless of the drug/lipid ratio adopted. As for the drug loading capacity, this parameter increased proportionally with the initial amount of added drug. The co-loading of RIF and INH in the liposomes significantly increased the encapsulation efficiency, with respect to the formulations containing the equivalent amount of the single drug.

Table 1. Particle size (nm), polydispersity index (PDI), Encapsulation Efficiency (EE %) and Drug Loading (DL %) of unloaded, single loaded liposomes and RIF/INH co-loaded liposomes (mean ± standard deviation).

Liposome content	Z-Average (nm)	PDI	EE %	DL %
Unloaded	350 ± 29	0.266 ± 0.030	-	-
RIF 3%	332 ± 33	0.283 ± 0.094	55.1 ± 6.1	1.7 ± 0.3
RIF 6%	347 ± 18	0.373 ± 0.115	55.3 ± 6.6	3.8 ± 0.1
RIF 12%	398 ± 15	0.440 ± 0.073	50.6 ± 7.1	5.9 ± 0.9
INH 15%	340 ± 25	0.124 ± 0.085	52.5 ± 6.2	7.8 ± 0.4
INH 30%	379 ± 51	0.262 ± 0.060	56.2 ± 2.8	14.9 ± 0.6
INH 60%	360 ± 8	0.200 ± 0.046	48.2 ± 0.9	22.4 ± 0.2
Co-loaded	361 ± 18	0.290 ± 0.032	RIF: 74.2 ± 6.4* INH: 71.3 ± 5.1$^{\#}$	RIF: 7.7 ± 0.7* INH: 9.2 ± 0.2$^{\#}$

3.2 Release studies

As shown in Figure 7, single loaded RIF and INH liposomes showed no significant differences in the drug release profile, independently to the amount of drug loaded. In agreement with its hydrophilic features, INH release rate was faster than that of RIF: 80-90% of INH was released in 5 hours, whereas 25-35% of RIF was released in the same time frame. As for the co-loaded liposomes, each drug showed the same release rate of the homologous single-loaded liposomes.

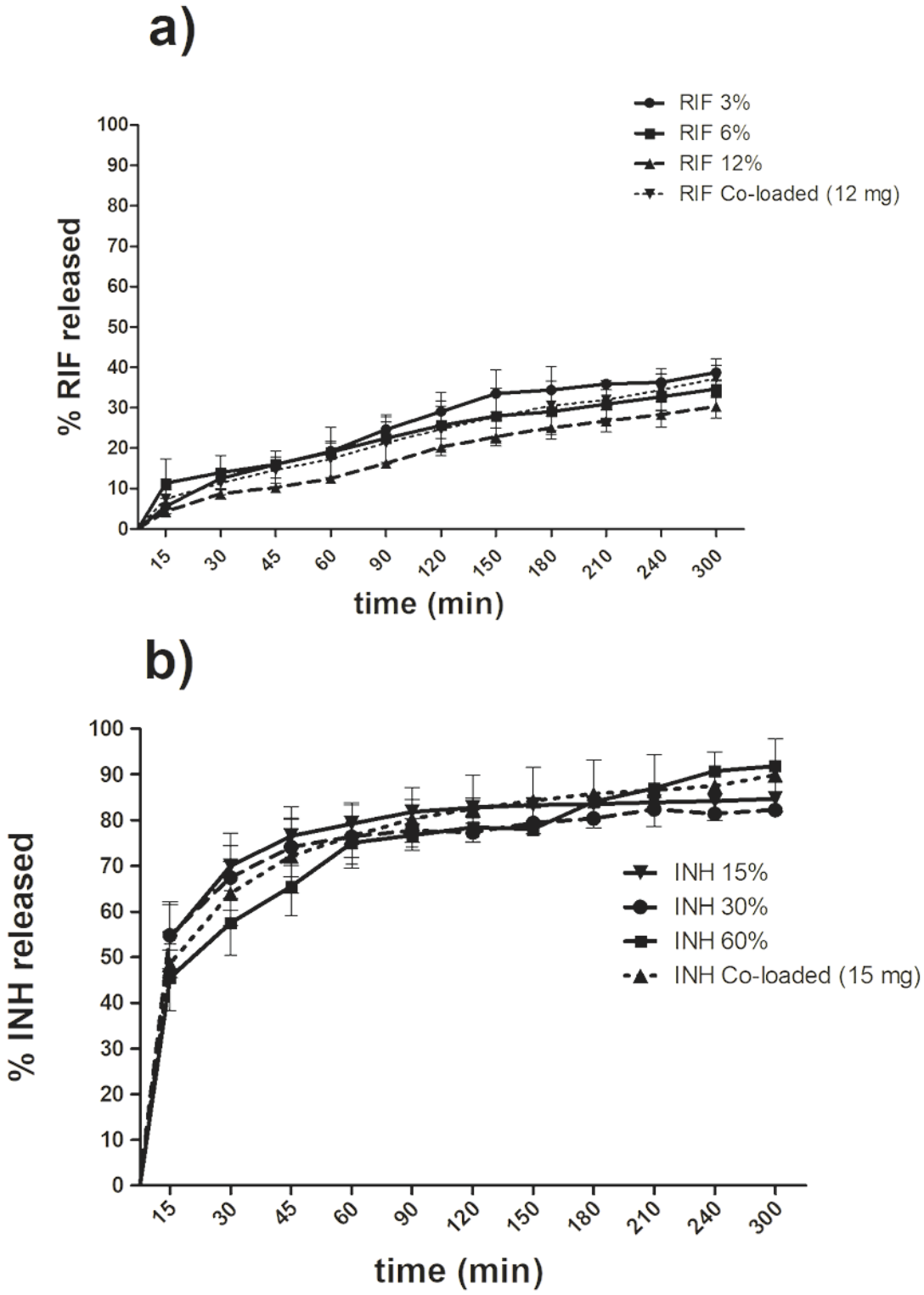

Figure 7. *in vitro* release profiles of (a) RIF, (b) INH from liposomes.

3.3 SANS experiment

The SANS data are displayed in Figures 8-9, as absolute scattering intensity (shifted vertically) plotted as a function of the scattering vector q. Error bars correspond to one standard deviation of the mean scattering intensity.

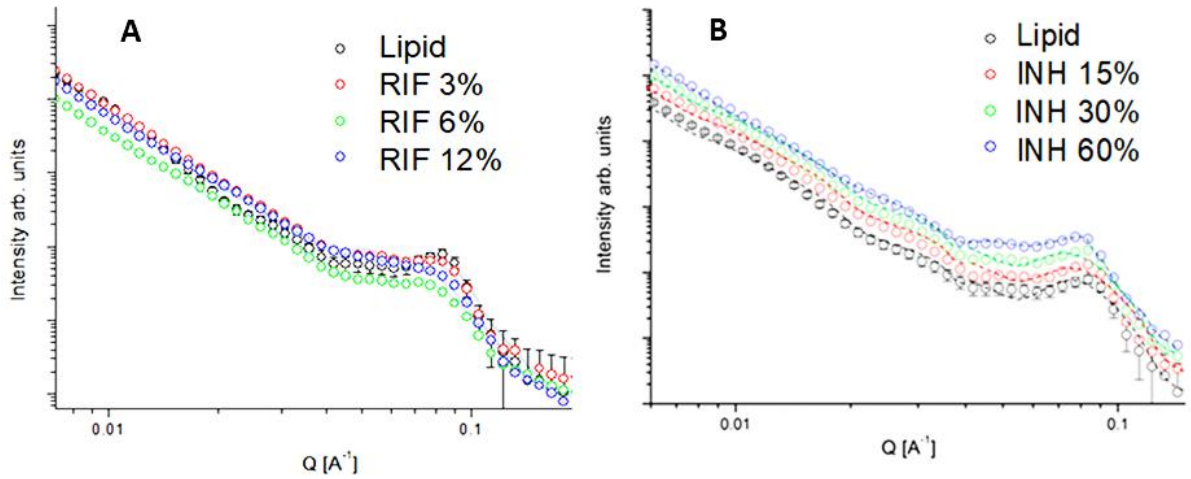

Figure 8. SANS profiles of unloaded and RIF-loaded liposomes at various RIF concentrations (A) and INH-loaded liposomes at various INH concentrations (B). Best fits (dashed lines) are superimposed to the experimental points (empty circles).

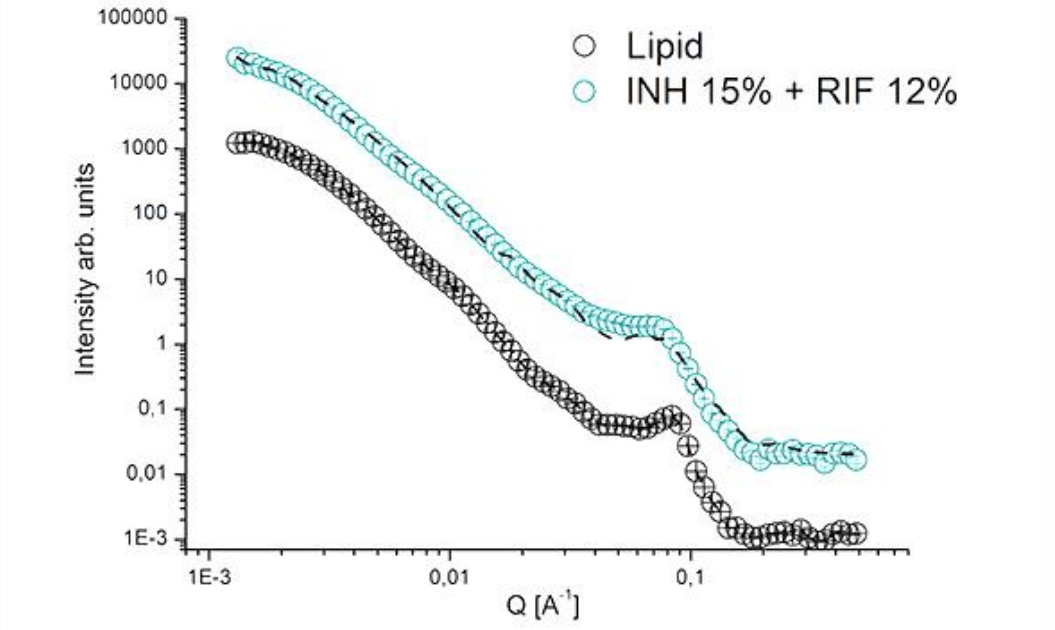

Figure 9. SANS profile of liposomes loaded with both INH and RIF at different relative concentrations compared with the scattering curve of empty liposomes (in black). Best fits (dashed lines) are superimposed to the experimental points (empty circles).

Figures 8-9 report the superimposed SANS profiles of representative samples of liposomes loaded with different concentrations of RIF, INH and both drugs respectively, together with the

corresponding best fit performed by SasView by using the well-established multi-lamellar vesicle model. This model provides the form factor, P(q), for a multi-lamellar vesicle depicted in Figure 2 with N lipid-drug shells of a span t_s and a scattering length density ρ_s, where the core is filled with solvent and the shells are interleaved with solvent-drug layers of a span t_w and a scattering length density ρ_0. All the parameters extrapolated from the best fits are reported in Tables 2 and 3.

Table 2. Best fit structural parameters obtained from the analysis of SANS curves of unloaded liposomes and for liposomes loaded with RIF and INH at different concentrations. The standard deviations are ~ 2% of the fitting parameters values.

Fit parameters	**r_c (nm)**	**t_s (nm)**	**ρ_s (nm^{-2})**	**t_w (nm)**	**ρ_0 (nm^{-2})**	**N**	**Liposome Size (nm)**
Unloaded liposomes	170	5.0	$2.38*10^{-6}$	1.8	$6.42*10^{-6}$	6	418
RIF 3%	170	4.6	$1.38*10^{-6}$	2.2	$6.40*10^{-6}$	5	404
RIF 6%	180	4.0	$1.70*10^{-7}$	2.7	$6.30*10^{-6}$	3	390
RIF 12%	184	4.1	$1.30*10^{-7}$	2.7	$6.40*10^{-6}$	2-3	397
INH 15%	170	4.8	$3.13*10^{-6}$	2.0	$6.42*10^{-6}$	6	418
INH 30%	170	4.8	$3.13*10^{-6}$	1.9	$6.38*10^{-6}$	6	417
INH 60%	172	4.6	$3.13*10^{-6}$	1.6	$6.00*10^{-6}$	5	403

Table 3. Structural parameters of liposome loaded with both drugs obtained from the analysis of SANS curves. The standard deviations are ~ 2% of the fitting parameters values.

Fit parameters	**INH 15% + RIF 12%**
r_c (nm)	167
t_s (nm)	4.8
ρ_s (nm^{-2})	$3.06*10^{-6}$
t_w (nm)	2.0
ρ_0 (nm^{-2})	$6.40*10^{-6}$
N	4
Liposome Size (nm)	418

Unloaded liposomes assemble in solution as oligo-lamellar vesicles constituted of roughly 6 concentric bilayers giving rise to a periodicity of ~ 68 Å (shell + water thickness), compatible with the thickness of each bilayer [87]. The vesicles are stable and show a spherical shape, well-matched with the best fit model used, with a size of ~ 420 nm (Table 2).

Regarding RIF-loaded liposomes, a reduction in the shell scattering length density (SLD, ρ_s) with respect to the unloaded liposomes was observed. This effect is symptomatic of structural modifications of the lipid bilayers due to a different packing of the lipid molecules upon the inclusion of the hydrophobic drug. On the contrary, no significant perturbations were appreciated in SLD of deuterated water confined among the shells and in the core of liposomes. Such RIF hydrophobic interaction modifies the structure of the multi-lamellar arrangement, in proportion to the concentration of the drug in the lipid (from 3% to 12%) (Figure 8A). In particular, starting from RIF at 6% concentration, we detected a reduction of the lamellae number with a concomitant slight increase in the periodical spacing, given by the repetition of the liposome lipid bilayers, and polydispersity of the shell thickness, obtained comparing the best fit parameter values, which changes to 0.5 and 0.6 for RIF at 6% and 12% respectively, compared to 0.3 obtained for the lowest RIF concentration. In addition, no significant aggregation was detected. The best fit results are reported in Table 2.

Regarding INH-loaded liposomes, the hydrophilic drug does not seem to induce significant changes in the multi-lamellar assembly of unloaded liposomes (Figure 8B). In fact, our results indicate that the lamellae number of oligo-lamellar vesicles is maintained up to 60% of INH (Table 2). At the highest tested concentration, the drug embedded within the liposomes induced a slight but significant decrease in the water-drug phase SLD, ρ_0 of the system, with a change in the inter-bilayer periodical spacing and a slight change in size of the liposomes.

Finally, the effect of the co-loading of both drugs on the liposomes was examined. Taking into account the structural modification which can affect the liposome stability due to the presence of the drugs, the combination of RIF at 12% and INH at 15% was chosen. In co-loaded liposomes the structure of the multi-lamellar arrangement was not affected by the presence of RIF. This is in contrast with the results obtained for RIF-loaded liposomes, despite the same amount of RIF was used in the formulation. The SANS data depicted in Table 3 indicated the presence of the drugs both in the water compartments and in the bilayer. Moreover, the vesicle demonstrated to be stable with a spherical shape, as evidenced from the goodness of the best fit with a multi-shell spherical model.

In order to better visualize the obtained results, the SLD profiles have been reconstructed from the values of the structural parameters, extrapolated from the best fits, as a function of the

liposome radius. The profiles obtained for the liposomes loaded with the highest drug concentrations (RIF 12% and INH 60%) and liposomes co-loaded with both the drugs (RIF 12% and INH 15%) are reported in Figure S1, in comparison with the unloaded sample.

4. DISCUSSION

Liposomes here described, co-incorporating RIF and INH, are intended for inhaled chemotherapy against pulmonary TB; they were designed to reach a higher antimycobacterial potency and improve the drug therapeutic profile [88]. The addition of two different drugs inside liposomal vesicles could alter the carrier structure; therefore, we performed an in-depth structural study in order to investigate any possible destabilization of the liposome framework. PCS analyses on the liposome samples showed no differences in size, regardless of the type and amount of the embedded drug. All the samples have an average diameter around 350 nm, demonstrating the suitability to be analyzed by SANS (Table 1) [75]. Regarding the PDI value, we observed some differences among the analyzed samples. For RIF-loaded liposomes, a parallel increase in the PDI values with the drug loading was detected, suggesting a drop of size homogeneity when an increase of drug loading occurred. This effect might be due to changes in the structural organization of the lipid bilayer caused by the hydrophobic drug, which may interact with phospholipid tails of the liposome lamellae [89,90]. In INH-loaded liposomes, the size homogeneity did not change with the increase of the drug loading, probably because INH is highly soluble in water and its interaction with the phospholipid lamellae is low. Finally, PCS analysis of co-loaded liposomes showed an intermediate value of PDI, with respect to the loaded and unloaded samples, indicating the opposite influence of the two drugs on the homogeneity of the vesicle size.

The results of PCS analysis were further supported by SANS data. By fitting the scattering curves, a destabilization of liposomal structure of RIF-loaded liposomes was highlighted. The fit parameters showed that the size underwent a slight decrease (too small to be detected by PCS analysis) with respect to the unloaded carrier. This modification is probably due to interactions between the hydrophobic tails of phospholipids and RIF. Moreover, at higher concentrations, the Bragg peak, indicating the spacing of the planes satisfying the Bragg's law, was wider and the lamellar structure appeared destabilized. The behavior in the presence of the hydrophilic drug INH was different, since liposome dimension and multi-lamellar assembly did not significantly change up to 60% of INH. The hydrophilicity of this drug leads to its confinement in the aqueous environment of the core and in the inter-bilayer spaces composing the liposome shell. Relevant changes in the stereochemistry of the multilamellar vesicles and,

in particular, in the thickness of the water and lipid layers t_w and t_s are not observed at the lower INH concentrations (15% and 30%). In contrast, for the sample with the highest INH concentration, a slight but significant decrease in both ts and tw is detectable, along with a decrease in the number of lamellae and a lower measured size (~ 403 nm). The position of INH within the liposome is also confirmed by water-drug layer SLD ρ_0, whose value decreases with the drug concentration respect to that of pure D_2O. Moreover, the change in the inter-bilayer periodical spacing suggests the formation of interactions between the drug and the phospholipid heads, at the water-lipid interface. These interactions are probably hydrogen bonds or van der Waals forces, giving rise to slight changes in the liposome size, which cannot be detected by PCS analysis. In more detail, the interaction of the phosphate region of the phosphatidylcholine's polar heads with the INH molecules could enhance the choline motional freedom [91], affecting the packing of the lipid bilayer. This effect is coherent with the observed decrease of the lipid bilayer thickness, which shifts from 5.0 nm for the unloaded samples to 4.8/4.6 nm for the INH-loaded vesicles. Notably, the disorganization of the lipids within the bilayer leads to an increment of the membrane fluidity, promoting the penetration of water molecules [92] and thus resulting in a slight increase of the shell SLD ρs for all the INH-loaded samples with respect to that of the control.

As confirmed by PCS studies, the SANS profiles for the co-loaded liposomes highlighted that, in the experimental condition adopted, it is possible to obtain stable liposomes co-embedded with both drugs. Notably, SANS data suggested that the hydrophobic RIF determines a large destabilization of the multi-lamellar vesicular structure, while the co-presence of INH and RIF causes an intriguing stabilization effect on the oligo-lamellar shelled liposome (Table 3). This synergistic effect promoted the uptake of both drugs inside the vesicles, as confirmed by the drug loading results. Taking into account the previous outcomes, it is important to underline that co-loaded liposomes proved to be able to incorporate higher amount of both drugs, even if the loading capacity was high for INH but not for RIF. This effect was previously observed in other studies and it was attributed to the enhanced solubility of RIF and INH in mixture [81]. On the basis of the results of SANS analysis, it is possible to provide a more detailed description for this phenomenon. The increased amount of RIF loaded might be explained by the structure stabilization exerted by the co-presence of INH, while the higher INH loading could be attributable to an increase in the lipid bilayer rigidity, induced by the intercalation of the hydrophobic RIF, during liposome formation. To the best of our knowledge, SANS data corroborate information provided by other spectroscopic techniques reported in the literature [89,90].

With regard to drug release, this effect did not elicit any significant variation in the *in vitro* behavior of these systems. Despite the different localization of the two drugs within the nanocarriers, the presence of RIF and IHN in the same liposome did not modify the release profiles of each drug, which remained substantially unaltered with respect to those of the mono-loaded formulations. A similar result was obtained by Gürsoy *et al.* [81], who used liposomes constituted of natural phosphatidylcholine, which possessed a low transition temperature, resulting in high membrane fluidity [93].

5. CONCLUSIONS

In this paper, we studied several liposome formulations as carriers for the most used anti TB-drugs: RIF and INH. Our data demonstrated the importance of SANS in defining not only the drug localization (expected data), but also the role that the drugs play in contributing to the stability of single and co-loaded liposomes. Studies performed with liposomal forms of tuberculostatics showed that the bilayer composition is critical for targeting liposomes and for obtaining stable drug-liposome formulations [94]. Moreover, a comprehensive study explaining the complex interaction between these drugs and liposomes is still lacking.

We showed that the SANS technique is able to define RIF and INH localization within MLV liposomes and drug-lipids interactions, providing important clues for obtaining stable nanoparticles to be used in tuberculosis therapy. In particular, we calculated the size of MLV and we obtained detailed information on their fine structure. Moreover, we described the changes, both in the water and in the lipid layers, attributable to the presence of the drugs, as these latter interfered with the MLV self-assembling. In the case of RIF-loaded liposomes, the hydrophobic molecules, embedded in the lipid bilayers, altered the lipid organization in the lamellae; we highlighted that this effect depends on the RIF concentration. Regarding the interaction of the hydrophilic INH with the phospholipid heads at the water-lipid interfaces, we evidenced that INH affected the bilayer structure as well as the organization of the coordinated water, in the water leaflet between the lamellae. The penetration of water molecules in the bilayer increased the distances between lipid molecules, producing in this way a sort of "membrane fluidification effect". When RIF and INH are co-loaded, the SANS data demonstrated that a sort of stabilization of the structure and dimension of the liposome occurred, which might promote, in a synergistic way, the embedding of both drugs.

In conclusion, SANS analysis supplies much more detail about the size than PCS and provides in depth information about the architecture of liposomes, allowing to better understand the

effects and the localization of these drugs inside the liposomes. In addition, the stabilization effect on the structure and dimensions of the liposome when RIF and INH are co-administered is an encouraging result for the development of more efficient nanoparticles.

All these outcomes represent the key preliminary step for the understanding of the *in vitro* and *in vivo* behavior of these systems and for the designing of new drug carriers, intended for inhalation therapy.

Chapter 3

In vivo behavior of Solid Lipid Nanoparticles surface decorated with a mannose-based surfactant: a promising tool for pulmonary tuberculosis treatment?

Eleonora Truzzi [1], Thais Leite Nascimento [2], Valentina Iannuccelli [1], Luca Costantino [1], Eliana Martins Lima [2], Eliana Leo [1], Cristina Siligardi [3], Magdalena Lassinantti Gualtieri [3], Eleonora Maretti [1]

[1] Department of Life Sciences, University of Modena and Reggio Emilia, Modena, Italy

[2] Laboratory of Pharmaceutical Technology, Federal University of Goiás, Goiânia, Goiás, Brazil

[3] Department of Engineering "Enzo Ferrari", University of Modena and Reggio Emilia, Modena, Italy

Submitted.

ABBREVIATIONS

ACN: acetonitrile

AM: alveolar macrophages

BALF: bronchoalveolar lavage fluid

DL: drug loading

ED: emitted dose

F127: lutrol F127

FMT: fluorescence molecular tomography

FPF: fine particle fraction

IS: internal standard

MR: mannose receptors

MS: mannose-based surfactant

Mtb: mycobacterium tuberculosis

RIF: rifampicin

SLNas: solid lipid nanoparticles assemblies

ST: sodium taurocholate

TB: tuberculosis

1. INTRODUCTION

Priorities to achieve the WHO goal of ending tuberculosis (TB) epidemic by 2030 include new drugs or formulation approaches to simplify and shorter conventional drug regimens [62]. TB is caused by *Mycobacterium tuberculosis* (Mtb) residing and surviving inside alveolar macrophages (AM). After being inhaled, Mtb reaches the alveoli, where it is phagocytosed by AM, a site difficult to be reached effectively by most antibiotics [95–99]. If the primary infection (pulmonary TB) is not completely eradicated, it can progress and disseminate into other organs (miliary TB). It is important to note that conventional administration routes, such as oral or parenteral, may lead to sub-therapeutic levels of anti-TB drugs at the primary site of infection, due to poor pulmonary distribution of most systemically administered drugs. As a result, drug-resistant strains may appear quickly [100]. Considering that 75-80% of infection cases remain localized in the lungs, the pulmonary route, widely used for local or systemic treatment of other pathologies [101], appears to be the most promising route of drug administration to reach promptly AM, the primary site of Mtb infection [102,103]. Local administration could harbor resistant tubercle bacilli and avoid first-pass metabolism and gastrointestinal degradation, leading to a reduction in dose level and preventing adverse drug reactions.

With the purpose to confer on drugs alone the properties required for a powder inhalation therapy in terms of respirability and internalization by AM, particulate vehicles have gained extensive attention. Among these, Solid Lipid Nanoparticles (SLN) are composed of lipids generally recognized as safe and devoid of toxicity following pulmonary administration [104,105]. Thus, SLN represent a useful approach for the administration of drugs against pulmonary TB, enabling their deposition onto alveolar epithelia and transport into AM after drug emission by Dry Powder Inhaler devices. Concerning the mechanism of AM entry, phagocytosis is established for particles in the range of about 1-3 μm and maintained by macrophages infected by *Mtb* providing efficient intracellular drug delivery after only 1 h [97,106,107]. In addition, drug biological activity inside infected AM can be reasonably expected owing to the intracellular biodegradation of the lipid matrix [108].

Within this context, we prepared respirable SLN assemblies (SLNas) loaded with rifampicin, a clinically useful anti-TB drug for an AM passive targeting [99,109]. SLNas surface-decorated with mannosylated derivatives proved to be able to interact with mannose receptors (MR) located on macrophages and overexpressed on Mbt-infected AM for an active targeting [110,111]. These SLNas exhibited a more efficient ability to enter AM cell line compared to bare RIF and non-functionalized SLNas with the involvement of MR-specific binding [112].

However, in addition to AM phagocytosis, other pathways should be considered before establishing a targeting to the alveolar region. Indeed, a few *in vivo* evidences of translocation across the alveolar epithelium through the *interstitium* into the blood or lymphatic circulation were referred. [113–118], although the mechanism involving inhaled nanoparticle alveolar clearance remains quite unknown. It therefore follows that *in vivo* experimental studies have to be performed to assess the actual fate of inhaled particles, especially for those having new surface physico-chemical properties.

Thus, the purpose of the present work was to detect in mouse lungs and extra-pulmonary organs the biodistribution of inhaled SLNas surface-decorated with mannose in comparison with untargeted SLNas.

2. MATERIALS AND METHODS

2.1 Materials

Palmitic acid (PA) was purchased from Fluka Chemie (Buchs, Switzerland), cholesteryl myristate (CM) from TCI Europe (Zwijndrecht, Belgium), polyoxyethylene polyoxypropylene block copolymer (Lutrol F127) (F127) from BASF (Ludwigshafen, Germany), sodium taurocholate (ST), rifampicin (RIF) from Alfa Aesar (Ward Hill, MA, USA), and IR-780 iodide from Sigma-Aldrich (Milan, Italy). The mannose derivative hexadecanoic acid (aminoethyl α-D-mannopyranoside) amide (MS) was synthesized as previously reported [99] and used as mannosylated functionalizing/surfactant agent. For HPLC analysis, methyl parahydroxybenzoate, used as internal standard (IS), was purchased from Carlo Erba Reagenti (Milan, Italy). For the *in vivo* experiments, ketamine and xylazine were purchased from Syntec (Santana de Parnaiba, São Paulo, Brazil), hematoxylin–eosin (H&E) from Easypath (Indaiatuba, São Paulo, Brazil), Hoechst 33342 from Invitrogen (Carlsbad, CA, USA), and Tissue-Tek O.C.T. Compound from Sakura (Alphen aan den Rijn, Netherlands). All the other chemicals were of analytical grade.

2.2 SLNas preparation

SLNas were prepared by the melt emulsification technique, as previously described in detail [112]. Briefly, the lipid phase containing 92.5 mg PA, 42.5 mg CM, and 45 mg RIF was melted and emulsified by ultrasonication in 10 mL MilliQ water containing the functionalizing/surfactant agent MS (0.1%) alone or in a blend with ST (0.05%) to prepare the samples SLNas/MS or SLNas/MS-ST, respectively. As controls, non-mannosylated samples

SLNas/ST and SLNas/F127 were obtained by using 0.2% ST and 1% F127, respectively. Labelled SLNas were prepared by dissolving 0.2% IR-780 in the melted PA.

2.3 HPLC analysis

Quantification of RIF in both mice organs and SLNas samples was carried out using a 1260 Infinity HPLC (Agilent Technologies, Santa Clara, CA, USA) equipped with a 1260 quaternary pump, 1260 DAD detector and 1260 ALS flow cell. Chromatographic separation was achieved using a Zorbax Extend C18 column (150 mm x 4.6 mm, 5 μm) (Agilent Technologies) at 35 °C. The mobile-phase consisted of a mixture of acetonitrile (ACN):water (v/v) with flow rate of 1.0 mL/min and used in a gradient as follows: 30:70 until 2 min, increasing to 70:30 at 2-4 min, kept at 70:30 until 7 min, decreasing to 30:70 from 7-9 min and kept at 30:70 until 11 min. Detection wavelengths were 254 nm and 333 nm (for plasma samples) and the injection volume was 10 μL. For the drug loading determination, a calibration curve from 5 to 30 μg/mL was obtained with r^2>0.995. Calibration curves in each organ were obtained from 0.09 to 2.7 μg/mL and from 3 to 7 μg/mL with r^2>0.988, using IS. Run time was 11 min, and RIF elution was observed at 5.4 min and IS elution at 3.7 min.

2.4 Drug loading levels

To 10 mg of SLNas samples, 10 mL of IS solution and methanol were added. The suspension was heated at 50 °C for 30 min, properly diluted (1:5) with methanol, filtered, and analyzed by HPLC. Drug loading (DL%) was calculated as the weight percentage of RIF in the total particle weight. The reported values were averaged on three determinations.

2.5 In vitro drug release

In vitro RIF dissolution and release from SLNas powders were examined in sink conditions on exactly weighed samples (100 mg) by means of the dialysis membrane (MWCO 12–14,000 Da; Medicell International Ltd., London, GB) method, in 30 mL of simulated lung fluid according to Marques [82] under gently magnetic stirring at the temperature of 37.0 ± 0.2°C to reproduce stagnant lung conditions. Sample solutions (1 mL) were withdrawn at fixed intervals for a time period of 6 h and the initial volume restored. RIF quantification was performed spectrophotometrically (Lambda 35; Perkin-Elmer, Norwalk, CT, USA) in triplicate at the wavelength of 475 nm. The reported values were averaged on three determinations.

2.6 In vivo study

2.6.1 Animals

Female Swiss mice aged 4-6 weeks (27 - 35 g) were obtained from the Central Animal Facility at Federal University of Goiás (Goiânia, Goiás, Brazil). Animals were acclimatized for a week prior to the beginning of experiments under 12:12 h light-dark cycles and controlled temperature. Food and water were provided *ad libitum* and animals were treated with chlorophyll-free grains for 7 days before treatment. Experiments were conducted according to the NC3RS guidelines for laboratory animal care. The experimental protocol (no. 109/18) was approved by the Animal Research Ethics Committee of the Federal University of Goiás. Animals were anesthetized before sample administration with ketamine and xylazine at 100 and 10 mg/kg, respectively. After intubation, 3 x 350 µL puffs of air were used to administer the powders into the mouse trachea using 20GA x 1.16" catheters connected to 1 ml syringe.

2.6.2 Real-time fluorescence imaging

Four groups of mice (n = 4 per group) were treated with 3 mg of labelled SLNas/MS, SLNas/MS-ST, SLNas/ST, and SLNas/F127 formulations. An untreated group was used as the control. Real-time fluorescence imaging was used to evaluate qualitatively the tissue distribution of SLNas formulations. Fluorescence scans were performed at 0.5, 3, 6, and 24 h after administration using a Fluorescence Molecular Tomography (FMT) *in vivo* imaging system (model 1500, PerkinElmer, Norwalk, CT, USA). Excitation and emission quantification wavelengths were 790 and 780 nm. Animals were euthanized 24 h after treatment using an excess of anesthetic. Lungs, heart, liver, and kidneys were harvested, rinsed with 0.9% NaCl solution and imaged for fluorescence detection by FMT.

2.6.3 Lung section analysis

At 24 h after intratracheal administration of SLNas samples, lungs were dissected and flash-frozen with liquid nitrogen in Tissue-Tek O.C.T. Compound. Transverse sections of 6 µm thickness were obtained at various points along the length of the tissue (superior, median, and caudal regions) using a Leica CM-1850 cryostat (Leica Biosystems, Inc., Buffalo Grove, IL, USA). For histopathological evaluation, the sections were stained with H&E and analyzed using light microscopy (DM 2000 Leica Microsystems, Bannockburn, IL, USA) coupled to a photographic camera (Canon PowerShot S80, VA, USA). Moreover, lung sections were observed by fluorescence microscopy.

2.6.4 Rifampicin biodistribution

To quantify the amount of RIF in the different tissues after intratracheal administration mice were randomly divided into five groups (n = 4-6 per group) and treated with 3 mg of SLNas/MS, SLNas/MS-ST, SLNas/ST, SLNas/F127 and bare RIF diluted to 3 mg with mannitol (10% RIF) to obtain insufflation RIF dose comparable to those of SLNas samples. An untreated group was used as the control. Mice were euthanized 30 min and 3 h after treatment.

2.6.4.1 Actual inhaled drug dose

The non-administered SLNas powder was quantified in order to calculate the actual inhaled dose of RIF per mouse. In practice, each administration device was washed 10x with 2 mL of ACN containing IS. The resulted suspension was heated at 50 °C for 30 min and filtered (0.45 μm porosity). The obtained solution was analyzed by HPLC. The inhaled dose, expressed as percentage of the administered one, was calculated by subtracting the non-administered powder to the amount introduced into the administration device.

2.6.4.2 Bronchoalveolar lavage fluid

Bronchoalveolar lavage fluid (BALF) was collected as described by Aragao-Santiago [119]. Alveolar macrophages were separated from the BALF by centrifugation at 500 g for 10 min. The cell pellet was then split in two aliquots for AM fluorescence microscopy and RIF quantification. For fluorescence microscopy, BALF cells were smeared in duplicates onto slides using Cyto-system (Hettich, Germany) at 219 g for 10 min, at room temperature. Cytoslides were then stained with Hoechst 33342 and observed using fluorescence microscopy (DMI 4000B, Leica Microsystems, Bannockburn, IL). For RIF quantification, cells were lysed with the addition of 200 μL ACN containing IS and sonicated by ultrasonic bath for 15 min. The solutions were filtered (0.45 μm porosity) and analyzed.

2.6.4.3 Plasma and organs

Blood was collected by cardiac puncture and immediately centrifuged at 2,000 g for 5 min to separate the plasma, which was stored overnight at −70 °C before analysis by HPLC. Lungs, liver, and kidneys were harvested, rinsed with 0.9% NaCl, dried and weighed. Tissues were homogenized in pH 4.5 PBS, containing 10^{-3} M of ascorbic acid, by Ultra-Turrax at 20,000 rpm for 3 min in glass conical tubes placed in ice. The homogenates were stored at −70 °C overnight prior to HPLC analysis. RIF was extracted from tissues and plasma by protein

precipitation. 300 µL of homogenate and 150 µL of plasma were treated with 1 mL and 500 µL of ACN (4 °C), respectively, and mixed by vortex for 60 sec. The mixtures were centrifuged at 5,000 g for 5 min (4 °C). The supernatants were collected, filtered (0.45 µm porosity), and analyzed. The IS, diluted with ACN, was added to all samples to a final concentration of 0.69 µg/mL prior to protein precipitation.

2.6.5 Statistical analysis

Statistical analysis of data was performed by two-way Analysis of Variance (ANOVA) followed by Bonferroni's test. Differences between groups were considered to be statistically significant at $p<0.05$.

3. RESULTS AND DISCUSSION

3.1 In vitro properties

In our previous work [112], mannosylated SLNas/MS and SLNas/MS-ST targeted to alveolar macrophages (AM) were characterized for physico-chemical properties, lipid corona formation, cytotoxicity, and rifampicin (RIF) transport within AM in the presence of a pulmonary surfactant substitute. Non-mannosylated SLNas/ST and SLNas/F127 were used as the controls. The mannosylated samples satisfied the properties required for reaching the alveolar epithelium in terms of size and respirability (emitted dose and fine particle fraction). Moreover, the surface functionalization by means of mannose groups improved RIF translocation into murine AM cells without impairment caused by the proved nanoparticle interactions with pulmonary surfactant (Table 1)

Table 1. SLNas size, *in vitro* emitted dose (ED), fine particle fraction (FPF), intramacrophagic rifampicin (AM RIF), and intramacrophagic rifampicin in the presence of pulmonary surfactant after 0.5 h (AM RIF 0.5 h) and 3 h (AM RIF 3 h) determined on MH-S cell line (adapted from data in [112]).

	Size (nm)	**ED (%)**	**FPF (%)**	**AM RIF 0.5 h (%)**	**AM RIF 3 h (%)**
SLNas/MS	740 ± 85	87 ± 4	38 ± 5	98.43 ± 12.23	52.81 ± 2.32
SLNas/MS-ST	309 ± 30	84 ± 2	41 ± 5	71.38 ± 1.45	51.24 ± 1.57
SLNas/ST	668 ± 25	83 ± 1	53 ± 4	46.84 ± 1.96	46.93 ± 1.52
SLNas/F127	408 ± 57	72 ± 8	11.77 ± 0.01	40.34 ± 2.85	42.91 ± 5.03

The present investigation was designed to establish *in vivo* RIF biodistribution following intratracheal administration of SLNas/MS or SLNas/MS-ST samples in comparison with the controls SLNas/ST and SLNas/F127. Consequently, the same batch of each SLNas sample to be administered to mice was investigated for drug loading and *in vitro* release using simulated lung fluid as the release medium. Rifampicin payload in SLNas was about 10% without relevant differences among the samples: 9.6 ± 0.2, 10.3 ± 0.4, 11.8 ± 0.4, 8.10 ± 0.1 for SLNas/MS, SLNas/MS-ST, SLNas/ST, SLNas/F127, respectively.

Concerning *in vitro* release allowing for prediction of drug leaching before AM internalization, RIF release profile from SLNas was gradual compared with the fast and complete free RIF dissolution. About 30% RIF was released from mannosylated SLNas/MS and SLNas/MS-ST at the end of the experiment, less than the values detected from the non-mannosylated samples (Figure 1), probably owing to a stronger barrier offered by the mannosylated surfactant [99]. In the light of the fast internalization process by AM, acceptable drug retaining within SLNas matrices before macrophage uptake would be therefore reasonably expected.

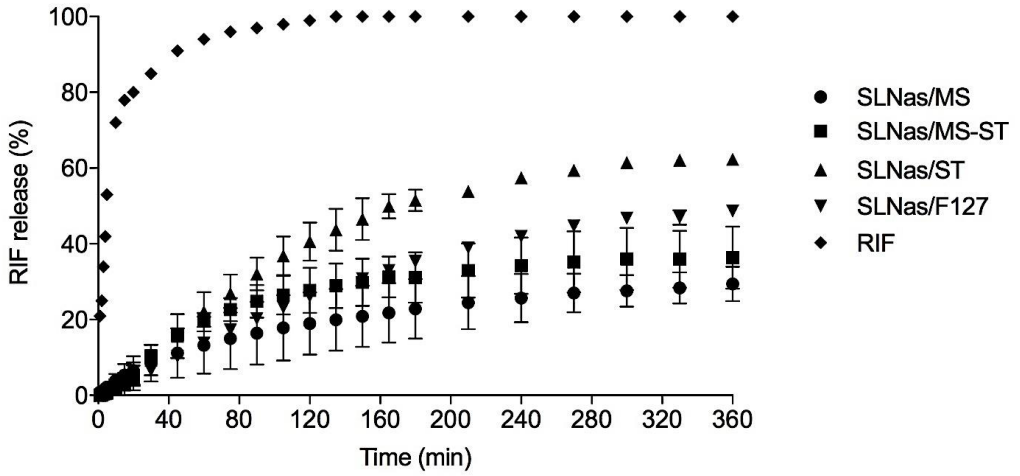

Figure 1. *In vitro* rifampicin (RIF) dissolution and release from SLNas samples in simulated lung fluid. For some points error bars do not exceed symbol size.

3.2 In vivo study

The transport of RIF within pulmonary and extra-pulmonary regions by means of mannosylated SLNas (SLNas/MS and SLNas/MS-ST) was assessed in mice following intratracheal administration of 3 mg dose of powder, the maximum tolerated dose. The study involved the real-time whole-body imaging on living mice and excised organs (lungs, liver, and kidneys) as well as the fluorescence microscopy of alveolar macrophages (AM) from BALF and lung

dissections. Additionally, RIF was quantified in AM, lungs, plasma, liver, and kidneys. Drug transport was compared with that provided by administering non-mannosylated SLNas (SLNas/ST and SLNas/F127) and bare RIF. Short-term studies were performed at quantification times of 0.5 and 3 h post-exposure since AM internalization as well pulmonary and extra-pulmonary effects occur within the first hours after administration [120–122].

FMT performed on mice that received labelled SLNas samples and the fluorescence microscopy on AM collected from BALF exploited the fluorescence emitted from IR-780 reasonably retained within SLNas. Indeed, IR-780 is a hydrophobic dye insoluble in water. For this reason, several nanostructures have been used to incorporate firmly, even if non-covalently, this dye until the target tissue [123]. If on one hand dye diffusion from SLNas lipid matrices in an aqueous environment is limited, on the other its *in vivo* release by SLNas lipolytic biodegradation is expected. In fact, following the nanoparticle rapid engulfment by AM [124,125], lipolysis may take place in AM lysosomes by lipolytic enzymes [126–128]. Excluding the low enzymatic activity in the respiratory tract, SLNas biodegradation may also occur by serum esterases towards nanoparticle migrated into the systemic circulation [117,129]. Nevertheless, efficient dye encapsulation in the lipid matrices could be assumed longer than the time periods used in the present study [130–132]. The same could also be applied to the lipophilic rifampicin embedded within SLNas before their uptake by AM.

Concerning RIF determination, data generating from each animal in terms of drug concentration were related to the drug loading corresponding to each administered sample. Moreover, since relationships between dosage emission and device flow-rate are well known [133–135], the actual inhaled dose per mouse was calculated by considering RIF amount not emitted by the device. The actual emission doses were ≥70% on those loaded inside the device (78.6 ± 3.3%, 69.3 ± 9.2%, 85.6 ± 5.4%, for SLNas/MS, SLNas/MS-ST, SLNas/ST, respectively). The lowest inhaled dose was found for the control SLNas/F127 (53.4 ± 10.7%) in agreement with its very poor flowability and high cohesiveness highlighted in a previous work [112].

3.2.1 Fluorescence imaging on mice whole-body and excised organs

SLNas accumulation and retention within lungs after intratracheal administration was assessed by real-time FMT. The analysis was carried out for 24 h in order to monitor particle permanence in lung and particle spreading to all body, by measuring IR-780 fluorescence intensity emitted from living mice whole-bodies. Moreover, excised organs (lungs, liver and kidneys) were analyzed 24 h post-exposure. Taking into account nanoparticle ability to penetrate into rodent lung interstitial spaces [136], SLNas detection in lungs was assigned to both particle

translocation across epithelial cells and internalization by AM which were not removed by BALF.

Despite IR-780 strong fluorescence intensity and low fluorescence mice diet used in the present study, mice auto-fluorescence limited monitoring SLNas distribution by means of FMT [137]. Nevertheless, increases in IR-780 accumulation compared with the fluorescence from untreated animals were registered only in the lungs of SLNas/MS-treated mice. Concerning mice organs excised at 24 h, fluorescence was registered only in the lungs, regardless of SLNas sample, even though a higher intensity was observed after SLNas/MS administration (Figure 2). This finding may offer a preliminary evidence of a more substantial translocation and long-term accumulation within lungs of the nanoparticles surface-decorated with MS as compared with the other SLNas samples. Appreciable IR-780 emissions from extra-pulmonary regions were not detected, regardless of SLNas sample, demonstrating the high retention of SLNas in the pulmonary region with a poor diffusion in the system circulation.

Finally, no IR-780 signal was found in the upper respiratory region at all scanning times, suggesting the nanoparticle deposition into the lower respiratory tract, without any mucociliary clearance.

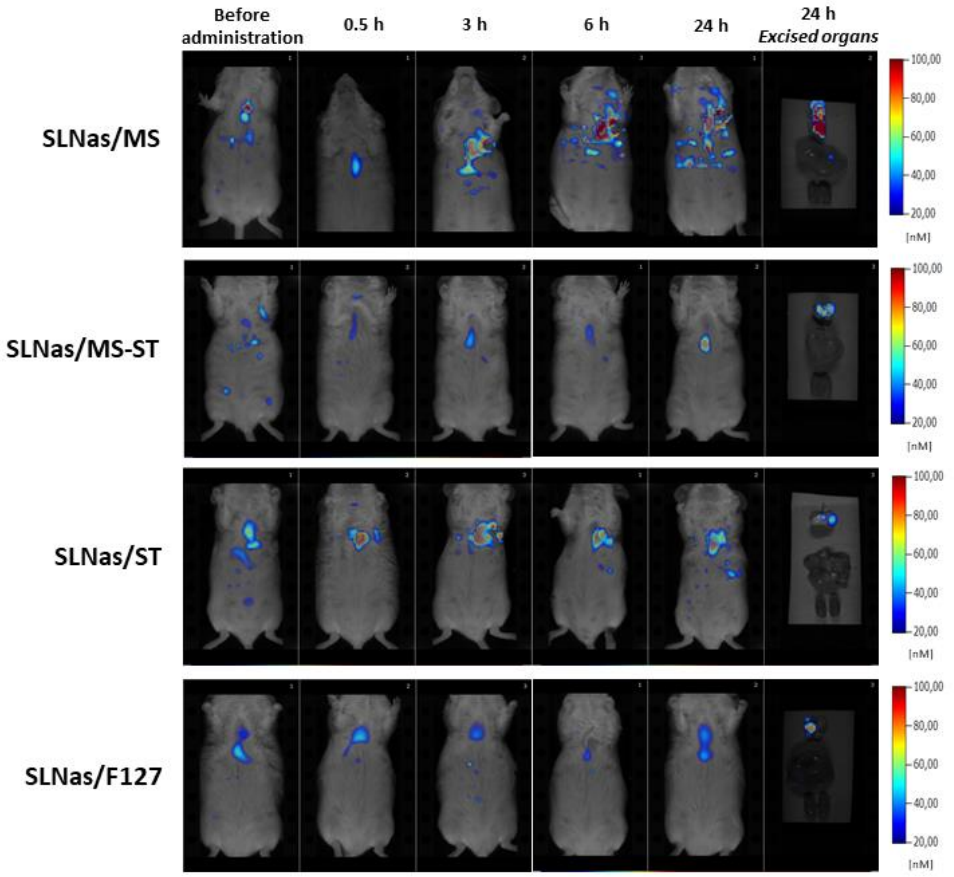

Figure 2. Representative FMT images at 0.5, 3, 6 and 24 h after administration of SLNas to mice. Whole-body scans were acquired after pulmonary treatment of SLNas/MS, SLNas/MS-ST, SLNas/ST, and SLNas/F127 samples. Images of the excised organs (lungs, liver, and kidneys from top down) show the organ biodistribution of particle-related fluorescence at 24 h post-exposure.

3.2.2 SLNas biodistribution in the pulmonary region

In order to further investigate the localization and permanence of SLNas samples within the pulmonary region, fluorescence microscopy on AM from BALF and lung tissue sections was performed. Subsequently, RIF quantification in both AM and lung tissue was exploited. Once nanoparticles are deposited onto the alveolar region of the respiratory tract, they first come into contact with pulmonary surfactant and then they are taken up by AM mostly within 2-3 h after particle deposition [114]. Hence, isolated BALF was employed in order to remove non-internalized nanoparticles from the lungs and collect non-adherent AM, i.e. the cells residing in the airway lumen and representing more than 90% of the cells contained in the mouse BALF [138–140]. As a further result, non-adherent AM are separated from interstitial macrophages, a large component of the total macrophage population in murine lungs residing in lung parenchyma [141]. AM recovery from BALF, however, has been reported to be incomplete

since the most AM activated by particle internalization strongly adhere to the lung tissue [141,142]. The morphologic study of BALF cell population confirmed that the majority of cells were AM. No significant differences in the total number of macrophages removed from the BALF were observed among the administered SLNas samples as well as in comparison with that obtained from the untreated mice, regardless of the collection time. Compared with the control, IR-780 particle-related fluorescence was observed in the collected AM for SLNas/MS, SLNas/MS-ST, and SLNas/ST both at 0.5 and 3 h post-exposure (Figure 3). This finding might already evidence the AM internalization of the mannosylated samples as well as SLNas bearing ST on their surface, nearly in agreement with previous *in vitro* results (Table 1). In contrast, negligible fluorescence intensities were detected for SLNas/F127, regardless of the collection time. Cell internalization appears, therefore, to be precluded in the case of SLNas/F127 as support of its insufficient respirability properties [99] and the known cell adhesion inhibition ascribed to F127 polyethylene oxide chains [143].

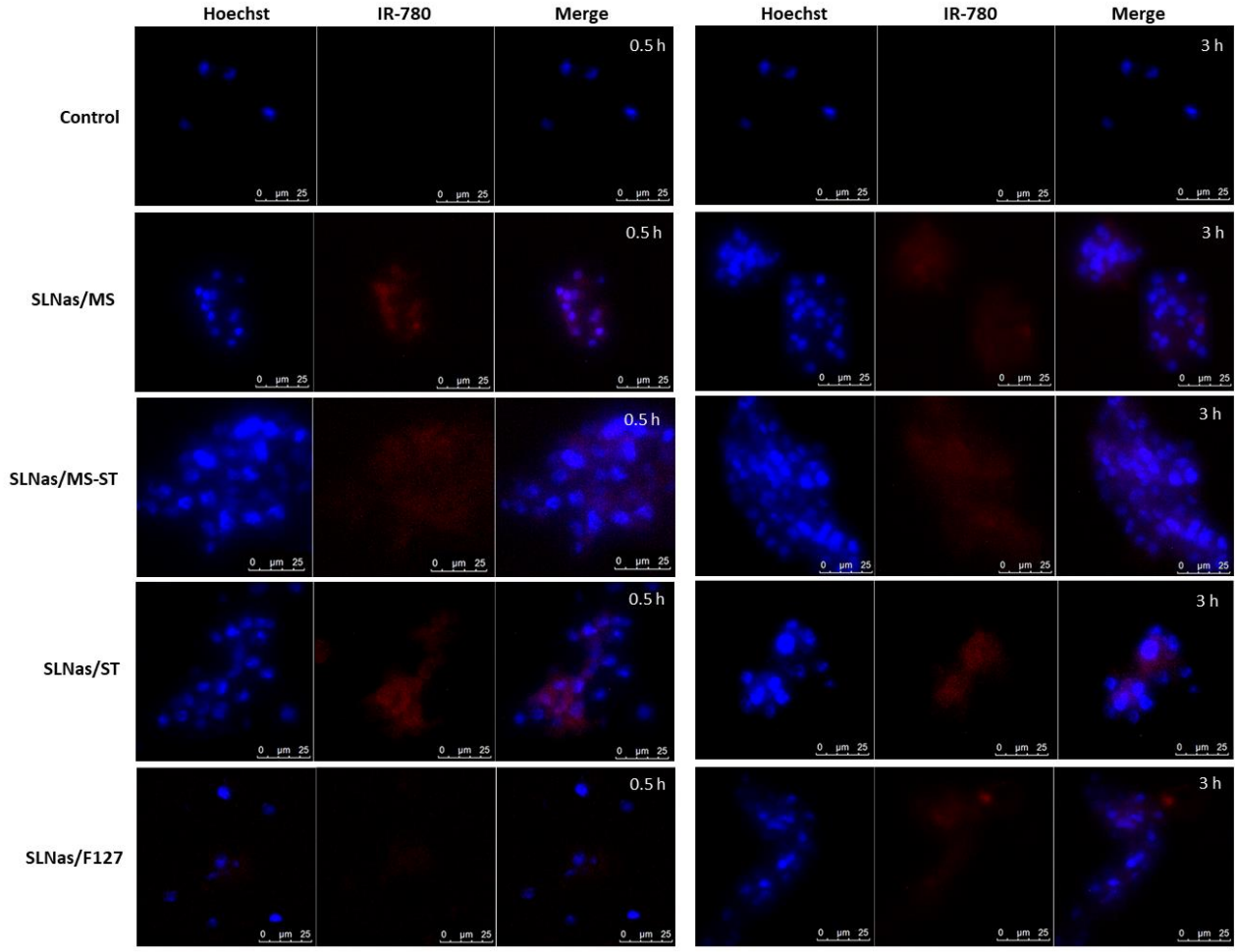

Figure 3. Fluorescence microscopy on AM from BALF showing SLNas post-inhalation exposure. Pictures were taken with a 40x magnification. From left to right, first frame: image taken using the filter for Hoechst staining

(cells), second frame: image taken using the filter for IR-780 (SLNas), third frame: merge, showing BALF AM in blue and IR-780/SLNas in red. Animals were euthanized after 0.5 (right panel) and 3 h (left panel) post-exposure and BALF was immediately collected for analysis. Scale bars = 25 µm.

Lung dissections at 24 h post-exposure observed by fluorescence microscopy indicated that a portion of SLNas was still present in the lung tissue, regardless of SLNas sample (Figure 4), in agreement with FMT results.

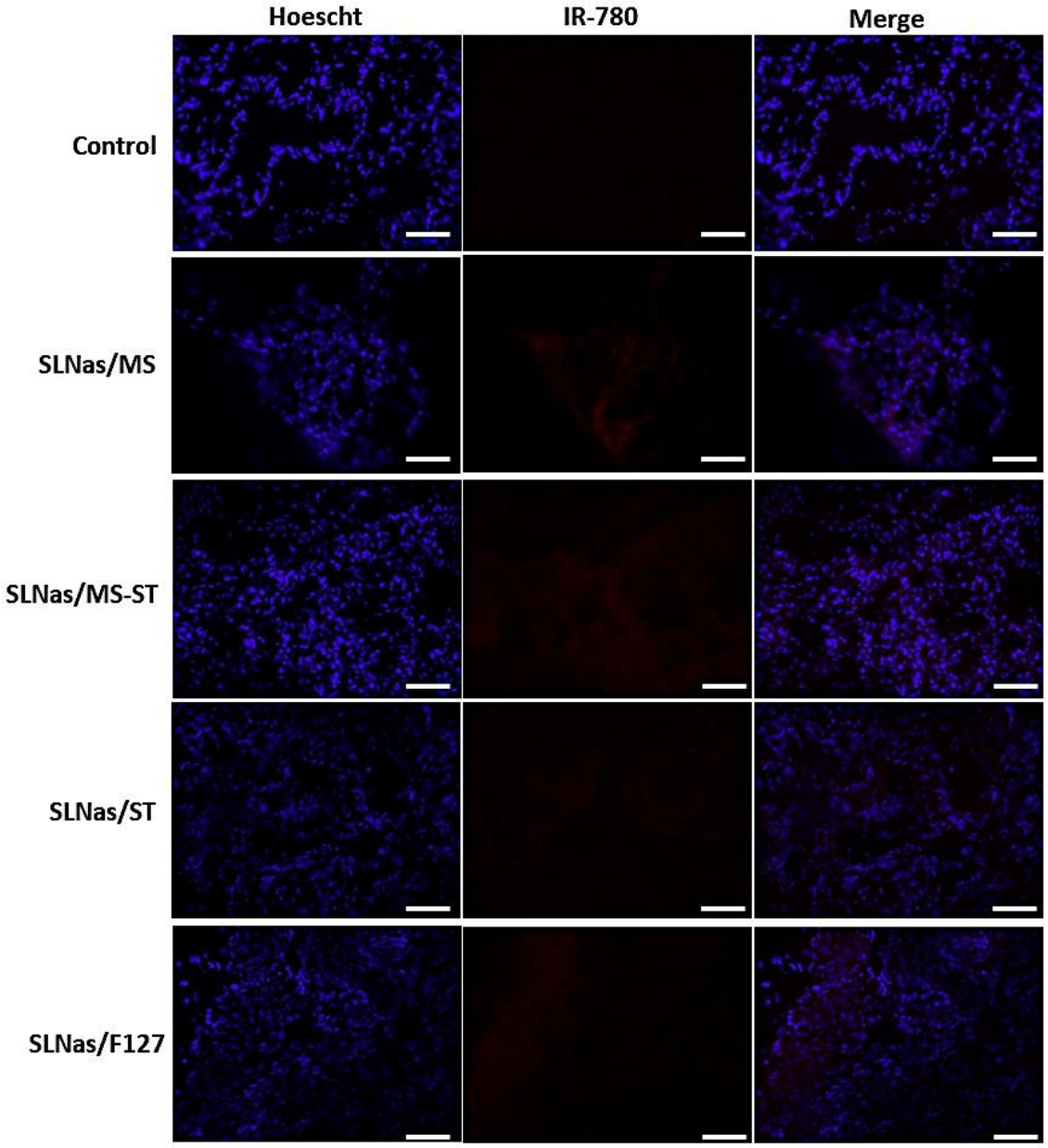

Figure 4. Representative fluorescence microscopy images of lung dissections at 24 h post-exposure. Pictures were taken with a 20 x magnification. From left to right, first frame: images taken using the filter for Hoechst label (cells), second frame: images taken using the filter for IR-780 label (SLNas), third frame: merge, showing lungs cells in blue and SLNas in red. Scale bars = 100 µm.

In the early time points post-exposure (0.5 and 3 h), the relationship between SLNas detected within AM by means of fluorescence microscopy and RIF quantification in the lungs might offer information about nanoparticle entry mechanisms according to their surface properties. The highest RIF levels in lungs ($p<0.001$) were found following SLNas/MS administration (19.65 ± 10.97% and 2.36 ± 2.65% of the inhaled dose per gram of tissue at 0.5 and 3 h, respectively). Otherwise, RIF levels were about 10-fold lower following 0.5 h exposure to SLNas/MS-ST and SLNas/ST (1.87 ± 1.97% and 2.35 ± 2.41% of the inhaled dose per gram of tissue, respectively) and about 4.5-fold lower for bare RIF (4.37 ± 3.30% of the inhaled dose per gram of tissue) without significant differences among them ($p>0.05$). Then, RIF levels declined up to the quantification limit or to negligible concentrations at 3 h post-exposure (Figure 5). Only SLNas/MS provided RIF levels higher than the minimum inhibitory concentration against *Mtb* strain [122] regardless of post-exposure time.

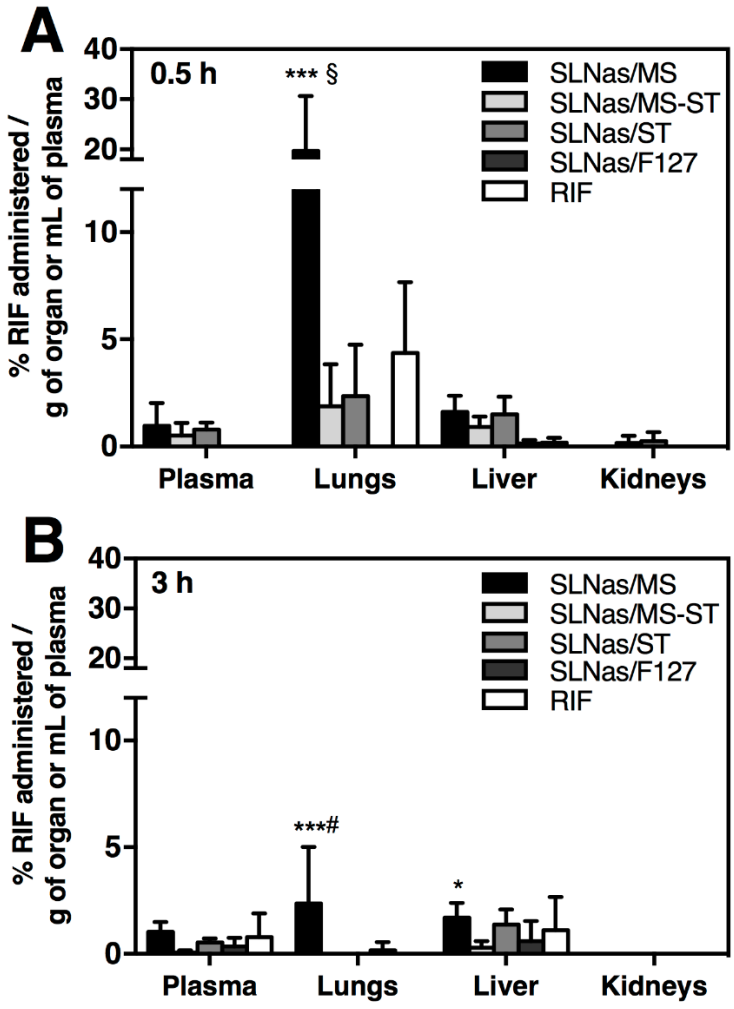

Figure 5. Quantification of RIF in plasma and tissue homogenates. Percentages of RIF inhaled dose per plasma volume or lung, liver or kidneys weight (n = 4-6) at 0.5 h (A) and 3 h (B) after pulmonary administration of SLNas/MS, SLNas/MS-ST, SLNas/ST, SLNas/F127, and bare RIF. ***§$p<0.001$ *vs* SLNas/MS-ST, SLNas/ST,

SLNas/F127 and bare RIF. ***#p<0.001 *vs* SLNas/MS-ST, SLNas/ST, SLNas/F127 and bare RIF. *p<0.05 *vs* SLNas/MS-ST.

The greater RIF retention in the lungs measured at 0.5 h post-exposure of SLNas/MS might have received the major contribution from internalization by adherent AM *via* the mannose-receptor mediated pathway in accordance with the results obtained previously on murine AM MH-S cells (Table 1). Although SLNas/MS-ST and SLNas/ST were detected within AM as well, the lower immediate retention of RIF in lungs compared with that achieved by SLNas/MS administration could be related to their passive mechanism of entry AM without mannose receptor involvement [112]. Despite this, the role of the carrier surfaces modified by MS in a blend with ST as well as ST alone would ensure a certain intramacrophagic activity in contrast to the inhalation of bare RIF. Indeed, drug localization in lungs post-exposure to bare RIF, showing difficulty of crossing AM membrane as demonstrated previously [99], could be reasonably assigned to a translocation mechanism across epithelial cells into the interstitium or other lung cells. Declining RIF concentrations at 3 h post-exposure was observed for all the groups. The decrease of RIF levels could be attributed to both AM clearance involving RIF biodegradation [99] and systemic translocation. Other pathways for lung entrance and subsequent clearance should be, however, considered for SLNas bearing ST on their surface. In fact, in addition to AM internalization, the paracellular passage should be possible owing to the well-known permeation enhancing properties of ST [11]. Otherwise, drug lung clearance following 3 h bare RIF post-exposure might be due to the molecule absorption beyond the epithelial barrier into the blood and lymphatic circulation. No RIF amounts, conversely, were measured in the lungs at both 0.5 and 3 h post-exposure to SLNas/F127 in agreement with the lack of AM fluorescence and RIF levels determined previously on murine AM cell line (Table 1). This finding is consistent with the non-adhering properties of F127 surfactant to cells, preventing nanoparticle translocation across both AM and epithelial cells along with the poor respirability features of SLNas/F127. No RIF was detected within non-adherent AM collected from the BALF post-exposure of all the samples, regardless of the exposure time probably owing to the quantification limit of the HPLC method.

From a histopathological point of view, lung sections examined at 24 h post-exposure to SLNas/ST, SLNas/MS-ST and SLNas/F127 samples indicated the absence of an inflammatory response. No signs of toxicity were expected, since all the samples were obtained by using recognized biocompatible excipients [21]. Moreover, *in vivo* administration of RIF on rats did not exhibited any evidence of toxicity after inhalation [144]. On the contrary, a mild neutrophilic infiltration in mice treated with SLNas/MS was noticed (Figure 6) even if MR

activation has been generally recognized as a promoter of the anti-inflammatory response [145–147]. Thus, a contribution to the inflammation might arise from the increased SLNas/MS endocytosis compared with the other samples leading to a higher production of reactive oxygen species [148].

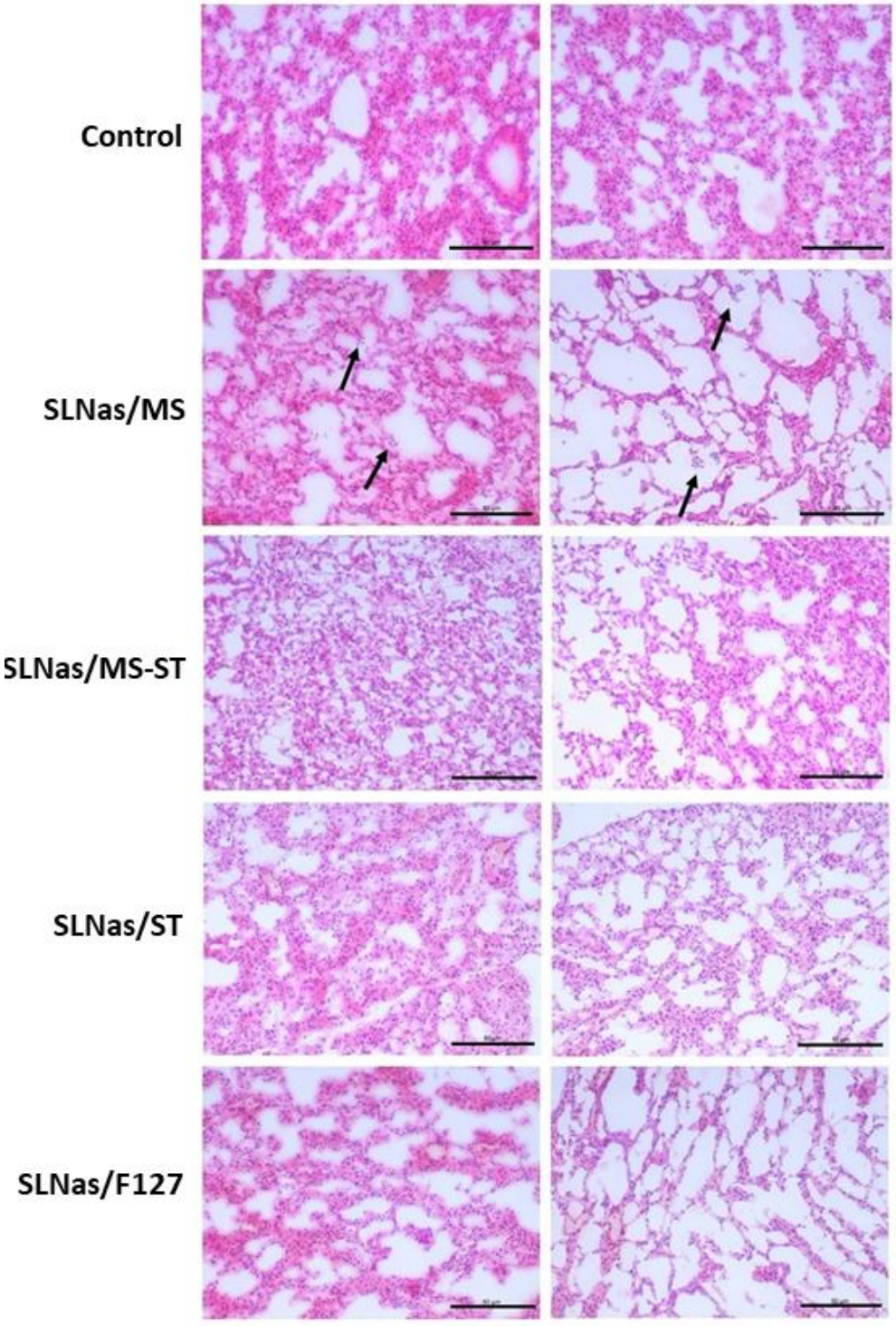

Figure 6. Histological sections of the medial (left panel) and inferior portion (right panel) of control mice lungs in comparison with lungs at 24 h post-exposure to SLNas/MS, SLNas/MS-ST, SLNas/ST, and SLNas/F127.

Arrows indicate mild neutrophilic infiltration. Slides were stained using H&E. Magnification: 20X. Scale bars = 80 μm.

3.2.3 SLNas biodistribution in extra-pulmonary regions

Inhaled nanoparticles have been proved to pass through the lung epithelium, enter the blood circulation, and accumulate in extra-pulmonary organs, according mainly to the nanoparticle size [116]. Translocation from the lungs to other organs with a possible accumulation in lymph nodes may occur from direct uptake into epithelial cells and/or phagocytosis by AM, which then migrate into the lung interstitium [119,149]. Thus, plasma, liver, and kidneys were analyzed by both RIF quantification at 0.5 and 3 h post-exposure of SLNas samples and bare RIF as well as FMT at 0.5, 3, 6, and 24 h post-exposure of SLNas samples. However, for the recovery of RIF in plasma, RIF serum half-life in mice (about 5 h) needs to be taken into account [150,151]. In addition, plasma levels are transient since they are balanced with the clearance by the kidneys and uptake by the other tissues. Drug levels in plasma and liver were found less than 2% for all the samples, regardless of the exposure time, without significant differences among them ($p>0.05$). These findings indicate the poor systemic activity offered by the lipid nanocarrier, irrespective of the pathway followed from the airway lumen into the lung tissue. Similarly, other studies in mice have evidenced negligible levels in blood and extra-pulmonary organs for nanoparticles >30 nm in size [113,116,119]. Drug levels in kidneys were barely measurable, regardless of the sample and the exposure time (Figure 5).

4. CONCLUSIONS

The present *in vivo* study was addressed to assess the fate of rifampicin transported by respirable mannosylated lipid-based nanoparticles designed for an intramacrophagic delivery. The results highlighted the suitability of the RIF-loaded nanocarrier obtained to efficiently target the alveolar macrophages *via* a mannose-receptor mediated pathway with a poor systemic biodistribution. The achievement of antimicrobial drug concentrations at this site of infection may support the goal of a potential application as inhaled therapy for the treatment of the pulmonary tuberculosis.

Chapter 4

Drug delivery strategies for geraniol nose-to-brain administration for Parkinson's disease treatment

- ***First strategy:*** submitted

Geraniol/Ursodeoxycholic Acid conjugate: a new prodrug against neuronal disorders administered by nasal route after nanoencapsulation

- ***Second strategy:*** preparing for submission

Delivery of naked GER in Cyclodextrin inclusion complexes

ABBREVIATIONS

ACN: acetonitrile

AFM: atomic force microscopy

BBB: blood-brain barrier

CDs: cyclodextrins

CNS: central nervous system

CSF: cerebrospinal fluid

DL: drug loading

DTA: differential thermal analysis

EE: encapsulation efficiency

GER: geraniol

GER-UDCA: geraniol- ursodeoxycholic acid conjugate

HPβCD: 2-hydroxypropyl-β-cyclodextrin

IE: inclusion efficiency

IR: fourier transform infrared

LNP: lipid nanoparticles

NOE: nuclear overhauser effect

NP: polymeric nanoparticles

PCS: photon correlation spectroscopy

PD: Parkinson's disease

SDS: sodium dodecyl sulphate

SEM: scanning electron microscopy

SLN: solid lipid nanoparticles

TGA: thermogravimetry

UDCA: ursodeoxycholic acid

1. INTRODUCTION

Parkinson's disease (PD) was first described by James Parkinson in 1817 in its "An essay on the Shaking Palsy" [152]. PD is a progressive neurodegenerative disorder which affects the 1% of the people over 65 years old. It is pathologically characterized by the prominent death of dopaminergic neurons in the *substantia nigra pars compacta*, leading to severe motor and non-motor symptoms [153].

Therapies currently used in PD treatment predominantly focused on symptomatic relief, aiming to either re-establish the dopamine level in the striatum or to act on striatal post-synaptic dopamine receptors. Nevertheless, as dopamine is not the only neurotransmitter involved in the disorder, several other drugs are also being used to target non-motor symptoms, such as depression or dementia.

Several mechanisms have been implicated in PD pathogenesis, where α-synuclein aggregation seems to play a central role in the development of the disease. Multiple other processes are thought to be involved in PD progression, such as mitochondrial dysfunction and neuroinflammation [154,155].

Geraniol (GER) is a volatile acyclic monoterpene abundant in several essential oils extracted from rose, lemongrass, lavender and other plants. GER demonstrated different pharmacological activities, such as antioxidant, anti-inflammatory and neuroprotective properties both in vitro and in vivo PD models [156–158]. All these reasons taken together with its classification in generally-recognized-as-safe (GRAS) category make GER a potential therapeutic agent for PD treatment, to arrest and treat the disorder disease [159].

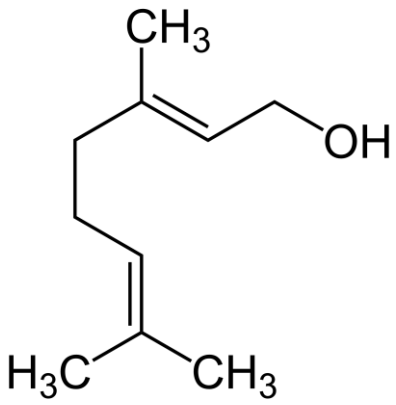

Figure 1. Geraniol chemical structure.

GER therapeutic properties were evidenced after oral administration of dosing ranging from 50 and more than 200 mg/Kg [156,158,160,161]. Pavan *et al.* demonstrated that GER is able to

reach the cerebrospinal fluid (CSF) after 30 min to the oral administration with a fast decrease over the time. In fact, after 60 min no GER was detected in CSF. Moreover, GER short half-life was determined around 12 min, due to a fast metabolic and excretion process and a compound distribution in all the body [159]. Taking into account these results, it is clear that to observe and obtain therapeutic effects in PD, a nose-to-brain administration of GER should be considered. Nose-to-brain administration demonstrated to increase drug levels in brain, reaching directly the target, avoiding the first-pass metabolism and the blood-brain barrier (BBB). In fact, in the nasal cavity the olfactory epithelium is the only region where the central nervous system (CNS) is not protected by the BBB and therefore in direct contact with the external environment. Following intranasal administration, drug can enter the CNS through 3 main pathways: the olfactory nerve in the olfactory region, the trigeminal nerve which innervates both the olfactory and respiratory regions and the vascular pathways, since the nose is highly vascularized [162]. However, GER is a high volatile compound with irritant effects on the mucosae. In that, an appropriate delivery system is required in order to protect the nasal mucosae after an intranasal administration. Otherwise, GER derivatization and modification might be an alternative strategy for its administration via nose-to-brain.

Therefore, in this project two different strategies were designed, developed and applied to intranasally administer GER to exploit its pharmacokinetic through this pathway. The first strategy aimed to encapsulate naked GER or its newly synthesized prodrug covalently conjugated with the ursodeoxycholic acid (UDCA) into lipid- and polymeric-based nanoparticles. UDCA was used as compound for the prodrug synthesis due to its therapeutic properties in PD. In fact, UDCA recently demonstrated a rescue mitochondrial function in parkinsonian patients and it is now in phase II of a clinical trial [163,164]. Moreover, the good safety and tolerability of UDCA make it a promising compound for PD treatment. All the nanoparticle formulations were characterized. In vivo tests were performed in rats by administering the most suitable formulation.

The second strategy aimed to encapsulate naked GER as an oil in cyclodextrin inclusion complexes. The inclusion complexes were optimized, fully characterized and in vivo tested.

2. FIRST STRATEGY: MATERIALS AND METHODS

2.1 Materials

UDCA was kindly supplied by ICE Srl (RE, Italy) and used without purification. GER (98%), carbazole, *N*-ethyl-*N'*-(3-dimethylaminopropyl) carbodiimide hydrochloride (EDCI·HCl), HPLC-grade methanol, acetonitrile, ethyl acetate (EtOAc); Span 85, Tween 80, PLGA 75:25, high molecular chitosan, gelatin, Pluronic-F127 and sodium taurocholate hydrate 97% were acquired from Sigma–Aldrich (Milan, Italy). Compritol ATO 888 was a kind gift from Gattefossè (Saint Priest, France). Triacetin and isopropyl myristate were obtained from Merck KGaA (Darmstadt, Germany). Miglyol 812 was purchased from Sasol (Witten, Germany). All other chemicals were of analytical grade.

2.2 Synthesis

Thin layer chromatography (TLC) was performed on precoated silica gel glass plates 60F254 (thickness 0.25 mm, Merck). Reagents and compounds were detected under short wave- length UV light and by heating after spraying with a 5% phosphomolybdic acid solution. Silica gel (Fluka, Kieselgel 60, 70−230 mesh) was used for preparative column chromatography. ^{1}H and ^{13}C-NMR spectra were recorded on 400 MHz spectrometers in $CDCl_3$ at room temperature. Chemical shifts are given in parts per million (ppm); J values are given in hertz (Hz). All spectra were internally referenced to the appropriate residual undeuterated solvent. Mass spectra were recorded using a LCQ Duo (ThermoQuest, San Jose, CA, USA), equipped with an electrospray ionization (ESI) source. IR spectra were recorded on a Perkin-Elmer FT-IR Paragon 500.

2.3 Synthesis of GER-UDCA conjugate.

A solution of UDCA (1.50 g, 3.82 mmol), GER (0.65 g, 4.20 mmol) and 4-dimethylaminopyridine (DMAP) (0.46 g, 3.82 mmol) in dry DMF (8 mL) was treated at 0°C with EDCI·HCl (0.80 g, 4.20 mmol). The reaction mixture was stirred at 0°C for 1 h then at room temperature monitored by TLC (cyclohexane/EtOAC 40:60). After 20 h the mixture was evaporated under vacuum to dryness, then EtOAc (50 mL) was added. The organic layer was washed with 5% aqueous HCl (30 mL), saturated aqueous $NaHCO_3$ (40 mL) and brine (40 mL), then dried (Na_2SO_4), filtered and concentrated in vacuo. Chromatography on silica gel (cyclohexane/EtOAc mixture 40:60) provided product **1** (1,67 g, 83%) as a sticky solid.

^{1}H-NMR (400 MHz, $CDCl_3$): δ 5.32 (t, J = 6.8 Hz, 1H), 5.07 (br, 1H), 4.58 (d, J = 6.8 Hz , 2H), 3,57 (br, 2H), 2.40-2.14 (m, 2H), 2.15-1,0 (m, 39 H), 0.93 (s, 3H), 0.91 (d, J = 6,4 Hz, 3H), 0.66 (s, 3H).

^{13}C{1H}-NMR (101 MHz, $CDCl_3$): δ 174.28, 142.14, 131.80, 123.73, 118.33, 71.42, 71.35, 61.21, 55.68, 54.88, 46.53, 43.74, 42.41, 40.10, 39.52, 39.14, 37.27, 36.79, 35.23, 34.90, 34.05, 31.32, 31.01, 30.31, 28.58, 26.88, 26.28, 25.68, 23.37, 21.14, 18.37, 17.69, 16.47, 12.11.

FT-IR (neat, cm^{-1}): νmax 3345, 2927, 1733, 1671, 1161. ESI-MS: m/z 551.33 $(M + Na)^+$

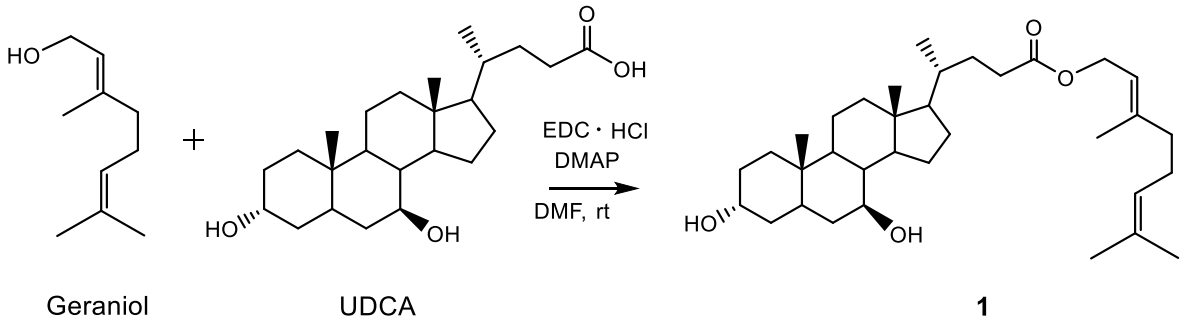

Figure 2 Synthesis of the conjugate GER-UDCA.

2.4 HPLC analysis

The quantification of the GER-UDCA prodrug and its hydrolysis product, GER, was performed by HPLC. The chromatographic apparatus consisted of a modular system (model LC-10 AD VD pump and model SPD-10A VP variable wavelength UV−vis detector; Shimadzu, Kyoto, Japan) and an injection valve with 20 μL sample loop (model 7725; Rheodyne, IDEX, Torrance, CA, USA). Separations were performed at room temperature on a 5 μm Hypersil BDS C-18 column (150 mm × 4.6 mm i.d.; Alltech Italia Srl, Milan, Italy), equipped with a guard column packed with the same Hypersil material. Data acquisition and processing were accomplished with a personal computer using CLASS-VP Software, version 7.2.1 (Shimadzu Italia, Milan, Italy). The detector was set at 210 nm. The HPLC assay of GER alone was isocratically performed with a mobile phase constituted by a mixture of CH_3CN and H2O 50:50 (v/v). The flow rate was 1 mL/min and the retention time 4.7 min. The HPLC assay of GER-UDCA alone was isocratically performed with a mobile phase constituted by a mixture of CH_3CN and H_2O 90:10 (v/v). The flow rate was 1 mL/min and the retention time 5.5 min. The isocratic conditions were used for the evaluation of GER loaded in the nanoparticles and GER-UDCA

solubility, its loading and release from nanoparticles (see below). The chromatographic precision for GER and GER-UDCA dissolved in a water-acetonitrile mixture (50:50 v/v) was evaluated by repeated analysis (n = 6) of the same sample (100 μM) and it is represented by the relative standard deviation (RSD) values of 0.91% and 0.89%, respectively, referred to peak areas. The calibration curves of peak areas versus concentration were generated in the range 1 to 500 μM for GER and GER-UDCA dissolved in a mixture of aqueous phase and acetonitrile (50:50 v/v ratio). The calibration of GER and GER-UDCA alone were also performed in pure acetonitrile (for GER or GER-UDCA loading studies). Moreover, the calibration of GER-UDCA was performed in 50 mM Tris-HCl buffer (pH 7.4) mixed to 10% methanol (for kinetic studies) and in water with 5 mM sodium dodecyl sulfate (SDS, for release studies). All the calibration curves of GER and GER-UDCA were linear (n = 10, r > 0.995, P < 0,0001).

In order to simultaneously quantify GER and GER-UDCA in blood or homogenate extracts, the mobile phase consisted of a mixture of water and acetonitrile regulated by a gradient profile programmed as follows: isocratic elution with 40% (v/v) CH3CN in H_2O for 11 min; then a 4 min linear gradient to 90% (v/v) CH_3CN in H2O; the mobile phase composition was finally maintained at 90% CH_3CN for 8 min. After each cycle the column was conditioned with 40% (v/v) CH_3CN in H_2O for 10 min. The flow rate was 1 mL/min. Carbazole was used as internal standard for the analysis of rat blood and liver or brain homogenate extracts (see below). The retention times for GER, carbazole and GER-UDCA were 10.5, 14.9 and 21.3 min, respectively. The precision evaluation and calibration procedures following the extraction of the analytes from homogenates and whole blood were performed in the presence of the internal standard (carbazole) and are described in the appropriate sections (see 2.9. and 2.14.)

2.5 Water solubility of GER-UDCA

For determining the solubility of GER-UDCA, an excess amount of the naked compound (2 mg/mL) was added to 5 mL of water and left to equilibrate at room temperature under continuous stirring for 36 h. After centrifugation at 14,000 g for 15 min, a supernatant aliquot was mixed with acetonitrile (50:50 v/v ratio), then 10 μl of the mixture were injected into the HPLC system for GER-UDCA quantification. The experiments were performed in triplicate.

2.6 GER and GER-UDCA stock solutions.

Stock solutions of $5{\cdot}10^{-2}$ M GER and GER-UDCA in DMSO were prepared and stored at − 20 °C until their use for kinetic studies.

2.7 Kinetic analysis of GER-UDCA in Tris-HCl buffer.

The conjugate GER-UDCA was incubated at 37 °C in 50 mM Tris-HCl buffer (pH 7.4) mixed to 10% methanol (v/v, final concentration) in order to increase the GER-UDCA solubility and to obtain its 50 μM final concentration. In particular, $5 \cdot 10^{-2}$ M stock solution in DMSO was diluted 1:100 in methanol, then 5.4 mL of Tris-HCl 50 μM were spiked with 600 μL of the 500 μM solution of GER-UDCA in methanol. At regular time intervals 200 μL of samples were withdrawn and 10 μL aliquots were immediately injected into the HPLC apparatus in order to quantify the GER and GER-UDCA amounts. All the values were obtained as the mean of three independent experiments.

2.8 Preparation of rat brain and liver homogenates

Brains of male Sprague-Dawley rats (Charles-River, Milan, Italy) were immediately isolated after their decapitation and homogenized in 5 volumes (w/v) of TrisHCl (50 mM, pH 7.4, 4 °C) with an ultra-Turrax (IKA Werke GmbH & Co. KG, Staufen, Germany) using 3 × 15 s bursts. The supernatant obtained after centrifugation (3,000 x g for 15 min at 4 °C) was decanted off and stored at −80°C before its use for kinetic studies. The total protein concentration in the tissue homogenate was determined using the Lowry procedure [165] and resulted as 7.2 ± 0.4 μg protein/μL. The livers of male Sprague-Dawley rats were immediately isolated after their decapitation, washed with ice cold saline solution and homogenized in 4 volumes (w/v) of TrisHCl (50 mM, pH 7.4, 4 °C) with the use of a Potter-Elvehjem apparatus. The supernatant obtained after centrifugation (2,000 g for 10 min at 4 °C) was decanted off and stored at −80 °C before its use for kinetic studies. The total protein concentration in the tissue homogenate resulted as 29.4 ± 1.1 μg protein/μL.

2.9 Kinetic analysis of GER and GER-UDCA in rat brain or rat liver homogenates

GER or the conjugate GER-UDCA were singularly incubated at 37 °C in 3 mL of rat brain or rat liver homogenates, resulting in a final concentration of 500 μM obtained by adding 10 μL of $5 \cdot 10^{-2}$ M stock solution in DMSO for each milliliter incubated. At regular time intervals, 100 μL of samples were withdrawn and immediately quenched in 200 μL of ethanol (4° C); 100 μL of internal standard (100 μM carbazole dissolved in ethanol) were then added. After centrifugation at 13,000 x g for 10 min, 300 μL aliquots of supernatant were reduced to dryness under a nitrogen stream, then 150 μL of a water and acetonitrile mixture (50:50 v/v) were added, and, after centrifugation, 10 μL were injected into the HPLC system. In order to evaluate the

potential influence of unloaded nanoparticles on GER-UDCA hydrolysis, the same procedure was adopted for the analysis of rat liver homogenate samples containing the free prodrug in combination with unloaded NPs using the same amounts employed for the loaded ones. The only difference was the addition of 50 µL of dichloromethane to the withdrawn samples before the extraction procedure. All the values were obtained as the mean of three independent incubation experiments.

Recovery experiments were performed by comparing the peak areas extracted from brain or liver homogenate test samples (100 µM) at 4 °C with those obtained by injection of an equivalent concentration of the analytes dissolved in water-acetonitrile mixture (50:50 v/v). The average recoveries ± SD were 56.7 ± 2.3% for the GER extracted from rat brain homogenate; 38 ± 1.9% for the GER extracted from rat liver homogenate; 69.3 ± 3.8% for the conjugate GER-UDCA extracted from rat brain homogenate; 86.2 ± 4.7% for the conjugate GER-UDCA extracted from rat liver homogenate. The concentrations of GER and GER-UDCA were therefore referred to as peak area ratio with respect to their internal standard carbazole. The precision of the method based on peak area ratio was represented by RSD values in the different homogenates ranging between 1.33% and 1.41% for 100 µM GER or between 1.18% and 1.21% for 100 µM GER-UDCA. For all compounds analyzed, the calibration curves were constructed by using ten different concentrations in homogenates at 4 °C ranging from 5 to 500 µM and expressed as peak area ratios of the compounds and the internal standard *versus* concentration. The calibration curves were linear ($n = 10$, $r \geq 0.995$, $P < 0.0001$).

A preliminary analysis performed on blank rat liver homogenate samples showed that their components did not interfere with the GER, GER-UDCA, and carbazole retention times.

The half-life value of the conjugate GER-UDCA incubated in rat liver homogenate was calculated from an exponential decay plot of its concentrations versus incubation time, using the computer program GraphPad Prism (GraphPad, San Diego, CA). The same software was used for the linear regression of the corresponding semilogarithmic plot. The quality of the fits was determined by evaluating the correlation coefficients (r) and P values.

2.10 Preparation of GER and GER-UDCA-loaded nanoparticles

GER-loaded lipid nanoparticles (LNP) were prepared with both solvent evaporation and melt-emulsification techniques. Preparation parameters were changed for each lipid employed in order to obtain optimized formulations.

For the solvent evaporation method, Gelucire-based nanoparticles (LNP-GE 1 and 2) were prepared by dissolving 300 mg of lipid, GER and oil (when present) in 1 mL of

dichloromethane. The organic phase was dropped into 10 mL of water. The mixture was then sonicated (Vibra-Cell, Sonic & Materials, Inc. 53 Church Hill Road, Newton, CT, USA) for 2 min at 20 W and the obtained emulsion was stirred for 2 h to eliminate the organic solvent.

Gelucire-based nanoparticles (LNP-GM 3, 4 and 5) were prepared by the melt-emulsification method Briefly, 150 mg of Gelucire were melted at 65 °C and GER and oil (when present) were added. The mixture was fast cooled in an ice bath and then added to 10 mL of water, previously heated at 65 °C. Finally, the dispersion was homogenized for 5 min at 24000 rpm by ultraturrax (T-25 basic IkaLabortecnik, Staufen, Germany) and fast cooled in an ice bath for about 10 min.

Compritol-based nanoparticles (LNP-CM) were prepared by melting 150 mg of lipid at 85 °C and adding GER and oil (when present). The aqueous phase (6 mL, 1% of Tween80), previously heated at the same temperature, was poured into the lipid phase and the mixture was homogenized by 1 min of sonication at 22W (Vibra-Cell), followed by 1 min of ultraturrax (T-25 basic) at 24,000 rpm and 1 min of sonication at 22W (Vibra-Cell). Finally, the obtained emulsion was cooled in an ice bath for about 10 min.

All LNP samples were purified by dialysis (12000 – 14000 Da) and then freeze-dried for 24 h (Lio 5P, Cinquepascal, Milano, Italy).

Table 1. Sample preparation parameters.

Sample	Method	GER (mg)	Liquid lipid (mg)	Coating
LNPs-GE1	Solvent evaporation	30	-	-
LNPs-GE2		15	Isopropyl myristate 15	-
LNPs-GM3	Melt-emulsification	30	-	-
LNPs-GM4		15	Isopropyl myristate 15	-
LNPs-GM5		15	Triacetin 15	-
LNPs-CM1		15	-	-
LNPs-CMC		15	-	Chitosan
LNPs-CMG		15	-	Gelatin
NPs	Nanoprecipitation	15	Miglyol 812	-
NPs-C		15	Miglyol 812	Chitosan
NPs-G		15	Miglyol 812	Gelatin

Polymeric nanoparticles (NPs) were obtained by nanoprecipitation method. Briefly, 100 mg of PLGA, GER and Miglyol 812 (1:1 molar ratio) were dissolved in a solvent mixture (4 mL acetonitrile + 2 mL methanol). The organic phase was added into 30 mL of aqueous phase

(0.1% of Pluronic-127) and stirred overnight to complete solvent elimination. NPs were washed 3 times by centrifugation (Rotina 380R, Hettich, Germany) in 100 kDa MWCO Vivaspin columns and freeze-dried for 48 h (Lio 5P).

LNPs-CMC and LNPs-CMG and NPs-C and NPs-G were further coated by chitosan or gelatin, by adding sample suspensions into chitosan acid solution (0.8%) or gelatin solution (0.7%) and stirring overnight. The coated samples were washed 3 times by centrifugation (Rotina 380R) before freeze-drying.

GER-UDCA-loaded Solid lipid nanoparticles (SLNs) were prepared by emulsification/evaporation solvent method. Firstly, compritol ATO 888 (120 mg), Span 85 (40 mg) and 30 mg of GER-UDCA were dissolved in 3 mL of chloroform. This organic phase was dropped into 5 mL of aqueous phase (Tween 80 1% + Taurocholate sodium salt 1%, w/v) and homogenized by UltraTurrax (Ika-euroturrax T 25 basic, IkaLabortechnik, Staufen, Germany) at 24,000 rpm for 5 min. The O/W emulsion was poured quickly into 15 mL of the aqueous phase and sonicated at 20W for 3 min in an ice bath. The resulting suspension was maintained in magnetic stirring for 2 h to allow the solvent evaporation. Finally, SLNs were purified by dialysis (12000 – 14000 Da cut off) for 30 min and freeze-dried for 48 h (Lio 5P, Cinquepascal, Milan, Italy).

GER-UDCA-loaded polymeric nanoparticles (NPs) were obtained by nanoprecipitation method. Briefly, PLGA (100 mg) and GER-UDCA (30 mg) were dissolved in a solvent mixture (4 mL acetonitrile + 2 mL methanol). Then, the organic phase was added into 30 mL of aqueous phase containing 0.1% w/v of Pluronic-127 under magnetic stirring. The formulation was kept under magnetic stirring overnight to complete the elimination of organic solvents. NPs were purified 3 times by centrifugation (5000 x g) (Rotina 380R, Hettich, Germany) in 100 kDa MWCO Vivaspin (Sartorius, Goettingen, Germany) columns and freeze-dried for 48 h (Lio 5P).

2.11 Particle size, zeta potential and morphological analysis

Particle size, polydispersity index (PDI) and zeta-potential were measured by Photon Correlation Spectroscopy (PCS) (Zetasizer version 6.12, Malvern Instruments, Worcs, U.K. equipped with a 4 mW HeNe laser (633 nm) and a DTS software (Version 5.0)) at 25°C. Freshly prepared formulations were diluted in purified deionized water (1:5) and the analysis was performed in triplicate, each measurement was averaged over at least 12 runs.

SLNs morphology was determined by Atomic Force Microscopy (AFM) (Park Autoprobe Atomic Force Microscope, Park Instruments, Sunnyvale, CA, USA) at room temperature (25

°C), operating in non-contact mode, with resonance frequencies from 100 to 200 kHz. SLNs suspension was deposited onto a small mica disk with a diameter of 1 cm. Topographical AFM images was processed using Gwyddion (2.5 version) software. NPs morphology were observed by field-emission gun scanning electron microscopy (SEM-FEG, Nova NanoSEM 450, Fei, Eindhoven, The Netherlands) using both Scanning Electron Microscopy (SEM) and Scanning Transmission Electron Microscopy mode (STEM). NPs suspension was dropped on aluminium stub or carbon/copper grids for SEM-FEI and STEM, respectively, and after drying, coated with carbon under vacuum conditions (Carbon Coater, Balzers CED-010, Oerlikon Balzers, Balzers, Liechtenstein).

2.12 GER and GER-UDCA loading and entrapment efficiency

Formulations (2 mg) were dissolved in acetonitrile (2 mL) heated at 50 °C for 15 min. Then, samples were vortexed for 5 min and centrifuged at 14,000 g for 10 min. The supernatant was re-centrifuged, then 10 µL were injected into HPLC system for GER-UDCA quantification. All experiments were performed in triplicate. The drug loading (DL %) and drug entrapment efficiency (EE %) were calculated according to the following equations:

$$EE\% = \frac{Amount\ of\ prodrug\ in\ purified\ sample}{Total\ amount\ of prodrug\ used}\ x\ 100$$

$$DL\% = \frac{Amount\ of\ incorporated\ prodrug}{Total\ mass\ of\ freeze-dried\ sample}\ x\ 100$$

2.13 In vitro drug release

In vitro release profiles of GER-UDCA from nanocarriers were evaluated by ultracentrifugation separation technique. 0.5 mg of GER-UDCA or equivalent pro-drug amount loaded in freeze-dried nanoparticles were suspended into 75 mL of water with SDS 5 mM at 37 °C under magnetic stirring (100 rmp). At predefined time points (0.25, 0.5, 1, 1.5, 2, 4, 6 and 8h), 150 µL of sample were withdrawn and replaced by fresh release medium. The samples were centrifuged at 24,000 x g (Rotina 380R), for 20 min at 4 °C and the supernatant analyzed by HPLC, as described above. All experiments were performed in triplicate.

2.14 In Vivo GER and GER-UDCA nasal administration and quantification.

Adult male Sprague−Dawley rats (200- 250 g body weight) fasted for 24 h, anesthetized and laid on their backs, received by nasal way about 1 mg of GER (4 mg/kg) or about 500 µg of GER-UDCA (2 mg/kg). In particular, 55 µl of GER emulsified (10 mg/mL, corresponding to 11.4 µL/mL) in a mixture of glycerol and water 60:40 (v/v), or 55 µl of an aqueous suspension containing an amount of loaded SLNs corresponding to about 250 µg of GER-UDCA were introduced in each nostril of rats. The nasal administrations were performed using a semiautomatic pipet which was attached to a short polyethylene tubing. The tubing was inserted approximately 0.6–0.7 cm into each nostril. After the administration, blood (100 µL) and CSF samples (50 µL) were serially collected at fixed time points from each rat. The CSF was withdrawn using the cysternal puncture method described by van den Berg et al. [166], which requires a single needle stick and allows the collection of serials (40–50 µL) CSF samples that are virtually blood-free [167]. A total volume of about a maximum of 150 µL of CSF/rat (i.e. three 50 µL samples/rat) was collected during the experimental session, choosing the time points (n = 4-6, taking into account a maximum of three collections for rat) in order to allow the restoring of the CSF physiological volume. The CSF samples (10 µL) were immediately injected into the HPLC system for GER and GER-UDCA detection. For CSF simulation, standard aliquots of balanced solution (PBS Dulbecco's without calcium and magnesium) in the presence of 0.45 mg/mL BSA were used [168,169]. In this case, the chromatographic precision was evaluated by repeated analysis (n = 6) of the same sample solution containing 5 µM of GER (0,77 µg/mL) or GER-UDCA (2.65 µg/mL) and it is represented by the RSD values of 1.18% or 1.02%, respectively, referred to peak areas. The calibration curves of peak areas versus concentration in CSF simulation fluid of the analytes were generated in the range 1 to 300 µM for GER (0.15 to 46.5 µg/mL) and 1 to 40 µM for GER-UDCA (0.53 to 20.1 µg/mL), appearing linear ($n = 8$, $r \geq 0.994$, $P < 0{,}0001$).

The blood samples were hemolyzed immediately after their collection with 500 µL of ice-cold water, and then 50 µL of 10% sulfosalicylic acid and 50 µL of internal standard (100 µM carbazole dissolved in a water-methanol mixture (50:50 v/v) were added. The samples were extracted twice with 1 mL of water saturated ethyl acetate, and, after centrifugation, the organic layer was reduced to dryness under a nitrogen stream. Then, 150 µL of a water-acetonitrile mixture (50:50 v/v) were added, and, after centrifugation, 10 µL were injected into the HPLC system for GER and GER-UDCA detection. Recovery experiments were performed comparing the peak areas extracted from blood test samples (10 µM) at 4 °C (n = 6) with those obtained by injection of an equivalent concentration of the analytes dissolved in water-acetonitrile mixture (50:50 v/v). The average recoveries ± SD were 60.9 ± 2.8% and 74.6 ± 4.0% for GER

and the conjugate GER-UDCA, respectively. Their concentrations were therefore referred to as peak area ratio with respect to the internal standard carbazole. The precision of the method based on peak area ratio was represented by RSD values of 1.38% and 1.20% for GER and the conjugate GER-UDCA, respectively. The calibration curves referred to these compounds were constructed by using eight different concentrations in whole blood at 4 °C ranging from 2 to 40 μM (0.30 to 6.2 μg/mL for GER; 1.1 to 20.1 μg/mL for GER-UDCA) and appeared linear ($n = 8$, $r \geq 0.995$, $P < 0.0001$).

A preliminary analysis performed on blank CSF and blood samples showed that their components did not interfere with the GER, GER-UDCA, and carbazole retention times.

All in vivo experiments were performed in accordance with the European Communities Council Directive of September 2010 (2010/63/EU). Any effort has been done to reduce the number of the animals and their suffering.

2.15 Histopathological examinations of nasal mucosa

The short-term effect of GER and GER-UDCA-SLNs on the structural integrity of nasal mucosa was evaluated on adult male Wistar rats weighing 250–300 g (obtained from the Central Animal Facility at Federal University of Goiás). Animals were acclimatized for a week prior to the beginning of experiments and kept under 12:12 h light-dark cycles at 25°C ± 1°C with food and water ad libitum. GER, GER-UDCA-SLNs, PBS 7.4 (as negative control) and pure isopropyl alcohol (as positive control) were administered intranasally in rats (n=3). GER and GER-UDCA formulations were the same used for the uptake studies in CSF (section 5.14). Nasal administration was performed by introducing 55 μl of the sample in each nostril using a semiautomatic pipet, by inserting 0.6-0.7 cm of the attached polyethylene tubing into the nostrils. After 2h from the administration, the nasal mucosa was carefully removed. Tissues were washed in PBS, fixed in 10% v/v of formalin solution overnight and paraffin-embedded. Finally, slide samples (5 μm) were prepared using a microtome, stained with hematoxylin–eosin and observed under optical microscope (40x) to evaluate the mucosa integrity.

In vivo experiments were approved by the Federal University of Goiás (UFG) Animal Research Ethics Committee (protocol 38/18). Experimental protocols followed the principles for laboratory animal care and the Brazilian legislation (Law 11,794, October 8, 2008).

2.16 Statistical analysis

Statistical comparisons between percentage values of GER-UDCA and GER obtained by incubation of the free or encapsulated prodrug in liver homogenates were performed by one-way ANOVA followed by Dunnet post-test. Statistical comparison of the nanoparticle size was performed by one-way ANOVA test considering $p < 0.05$ statistically significant. Statistical comparison AUC test was performed by Student's test. $P < 0.05$ was considered statistically significant. The calculations were performed by using the computer program Graph Pad Prism.

3. FIRST STRATEGY: RESULTS

3.1 Synthesis of GER-UDCA prodrug.

The GER-UDCA prodrug 1 was obtained as sticky solid in 83% yield and ≥ 98% purity as determined by their 1H-NMR analysis after column chromatography. The molecular weight, 1H-NMR, 13C-NMR and IR spectra of prodrug were in agreement with those required by its structure.

3.2 Hydrolysis and solubility studies of GER-UDCA

A first step of the present work was the evaluation of the potential hydrolysis pattern of the GER-UDCA conjugate in different media such as Tris-HCl buffer, rat brain and liver homogenates. The second step was the nasal administration of GER-UDCA loaded in nanoparticulate systems and its detection in CSF and whole blood of rats. Toward these aims it was firstly necessary to detect and quantify not only the conjugate, but also GER, obtainable by the potential hydrolysis of the prodrug in all incubation media and all physiologic fluids. GER was chosen as hydrolysis product to be analyzed, being detectable and quantifiable by the UV detector of the HPLC system. To this purpose, an efficacious analytical method was developed based on the use of a reverse phase C-18 HPLC column and a mobile phase constituted by a mixture of water and acetonitrile following a gradient profile allowing us to quantify both the conjugate GER-UDCA and its hydrolysis product GER in the same HPLC chromatogram in all incubation media investigated.

The solubility value of GER-UDCA in water was 439 ± 35 nM (0.23 ± 0.02 μg/mL).

The conjugate GER-UDCA was not degraded in Tris HCl buffer (pH 7.4) during its incubation at 37 °C for 8 h.

The kinetic studies in rat brain and liver homogenates were performed by adding the stock solutions (1% v/v GER or GER-UDCA 5·10−2 M in DMSO) in the incubation media, taking

into account that the protein contents in physiologic fluids allowed solubilization of the lipophilic conjugate [170]. In these incubation media GER showed high stability within 6 h, whereas the conjugate GER-UDCA appeared degraded. In particular, Figure 3A reports the degradation profile of GER-UDCA in rat liver homogenate whose half-life is 36.5 ± 2.1 min. This degradation followed a pseudo first-order kinetic, confirmed by the linear pattern of corresponding semilogarithmic plot ($n = 8$, $r = 0.984$, $p < 0.0001$) suggesting, therefore, that conjugate degradation is governed by a hydrolysis process. The hydrolysis of GER-UDCA was confirmed by the GER appearance in incubation media with amounts increasing during time, as reported in Figure 3B. In particular, more than the 95% of GER-UDCA appeared hydrolyzed after incubation for 180 min in rat liver homogenate. This degradation profile was not significantly changed in the presence of unloaded PLGA or SLN particles (data not shown).
Similarly, the conjugate GER-UDCA exposed to rat brain homogenate underwent hydrolysis, as reported in Figure 4, however the reaction rate was markedly lower in comparison with the degradation in liver homogenate. Indeed, after 360 min of incubation, about the 30% of the conjugate appeared hydrolyzed, with the release of a corresponding amount of GER.

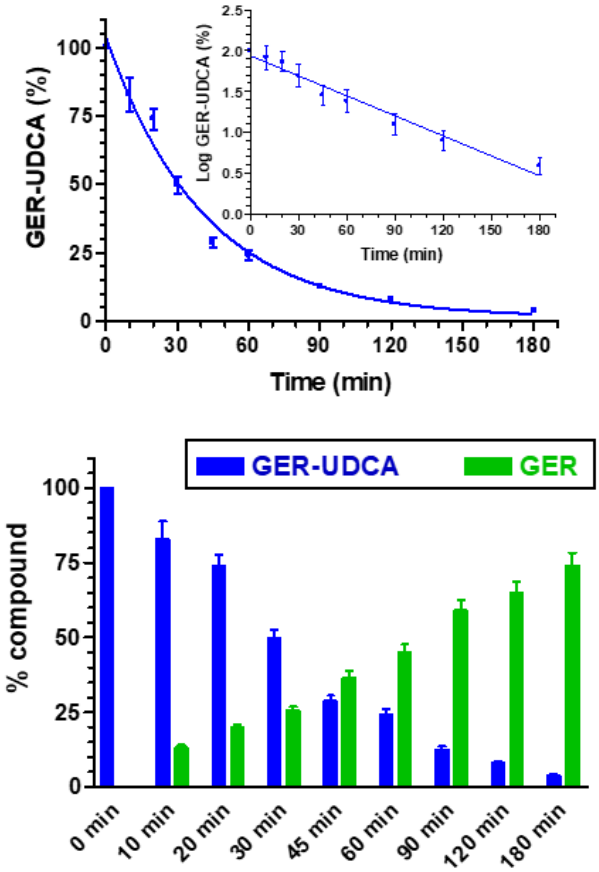

Figure 3. [A] Hydrolysis profile of the prodrug GER-UDCA incubated in rat liver homogenate and the corresponding semilogarithmic plot, whose linearity ($n = 8$, $r = 0.984$, $p < 0.0001$) indicate a pseudo first order kinetic process. **[B]** Hydrolysis profile of the prodrug GER-UDCA represented with the corresponding appearance

profile of GER during incubation in rat liver homogenate. All the values are reported as the percentage of the overall amount of incubated prodrug and as the mean ± SD of three independent experiments.

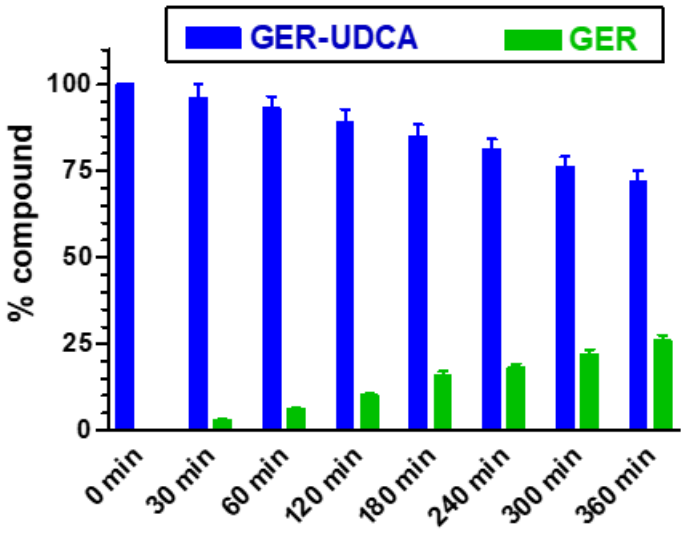

Figure 4. Hydrolysis profile of the prodrug GER-UDCA represented with the corresponding appearance profile of GER during incubation in rat brain homogenate. All the values are reported as the percentage of the overall amount of incubated prodrug and as the mean ± SD of three independent experiments.

3.3 Characterization of GER and GER-UDCA-loaded nanoparticles

Particle size, PDI and GER content of both lipid and polymeric nanoparticles are reported in Table 2 and 3. GER and GER-UDCA content is expressed as encapsulation efficiency (EE%) before freeze-drying and drug loading (DL%) after freeze-drying.

Table 2. Particle size, polydispersity index (PDI), Encapsulation Efficiency (EE%) and Drug Loading (DL%) of GER-loaded LNPs and NPs. NV: negligible value

Sample	Particle size (nm)	PDI	EE%	DL%
LNPs-GE1	173 ± 3	0.200 ± 0.040	52.0 ± 0.9	NV
LNPs-GE2	180 ± 4	0.220 ± 0.020	60.9 ± 0.5	NV
LNPs-GM3	93 ± 1	0.110 ± 0.010	53.0 ± 1.0	NV
LNPs-GM4	98 ± 3	0.170 ± 0.010	65.1 ± 0.9	NV
LNPs-GM5	102 ± 2	0.190 ± 0.020	62.0 ± 1.2	NV
LNPs-CM1	140 ± 2	0.180 ± 0.050	82.4 ± 0.5	NV
LNPs-CMC	328 ± 10	0.528 ± 0.110	82.9 ± 2.0	NV
LNPs-CMG	308 ± 4	0.475 ± 0.090	84.1 ± 2.5	NV
NPs	144 ± 4	0.052 ± 0.030	60.1 ± 2.0	NV
NPs-C	330 ± 7	0.500 ± 0.090	65.8 ± 1.5	NV
NPs-G	407 ± 5	0.117 ± 0.080	64.7%	NV

All GER-loaded LNPs and NPs showed a particle size below the 200 nm with a good dispersion homogeneity, except for the ones with chitosan or gelatin coating. In fact, especially for LNPs -CMC LNP -CMG, the addition of chitosan and gelatin polymers increased both particle size and non-homogeneity. GER quantification before freeze-drying process showed a high EE%, over 60%. However, for all the samples, DL% after freeze-drying process was not quantifiable, being near zero. Several modifications of the formulation process were adopted but negligible amounts of drug were found after freeze drying process in all cases. For this reason, formulation GER-loaded LNPs and NPs was not viable.

Table 3. Particle size, polydispersity index (PDI), Encapsulation Efficiency (EE%) and Drug Loading (DL%) of GER-UDCA-loaded lipid (SLNs) and polymeric (NPs) nanoparticles. Data represents mean ± SD (*;# $p<0.05$)

Formulation	Size (nm)	PDI	Zeta (mV)	EE%	DL% (w/w)
Unloaded SLNs	104 ± 5.3	0.148 ± 0.02	-20.0 ± 5.5	-	-
GER-UDCA-SLNs	121± 8.4*	0.164 ± 0.03	-22.5 ± 7.7	94.5 ± 2.6	6.2 ± 0.6
Unloaded NPs	144 ± 9.2	0.052 ± 0.01	-23.6 ± 4.6	-	-
GER-UDCA-NPs	181 ± 5.9#	0.060 ± 0.02	-26.7 ± 6.5	89.3 ± 3.2,	12.1 ± 1.4

Conversely, the EE% values of GER-UDCA-SLNs and GER-UDCA-NPs before freeze-drying were 94.5 ± 2.6% and 89.3 ± 3.2%, respectively and the DL% values of freeze-dried samples were 6.2 ± 0.6% (GER-UDCA-SLNs) and 12.1 ± 1.4% (GER-UDCA-NPs), demonstrating that the freeze-drying process did not remove GER-UDCA from these formulations as occurred for GER with the native compound.

GER-UDCA-SLNs and GER-UDCA-NPs showed mean particle size of 121 ± 8.4 and 181 ± 5.9 nm with polydispersity index less than 0.2, and zeta potential around -22.5 ± 7.7 and -26.7 ± 6.5 mV, respectively. It was observed that the incorporation of GER-UDCA into both nanosystems increased their size compared to unloaded formulations ($p< 0.05$). On the contrary, the particle homogeneity was not significantly affected by the addition of the drug, maintaining the narrow distribution for both the delivery systems. Additionally, morphology analysis showed spherical shape and homogeneous size of the nanoparticles (Figure 5).

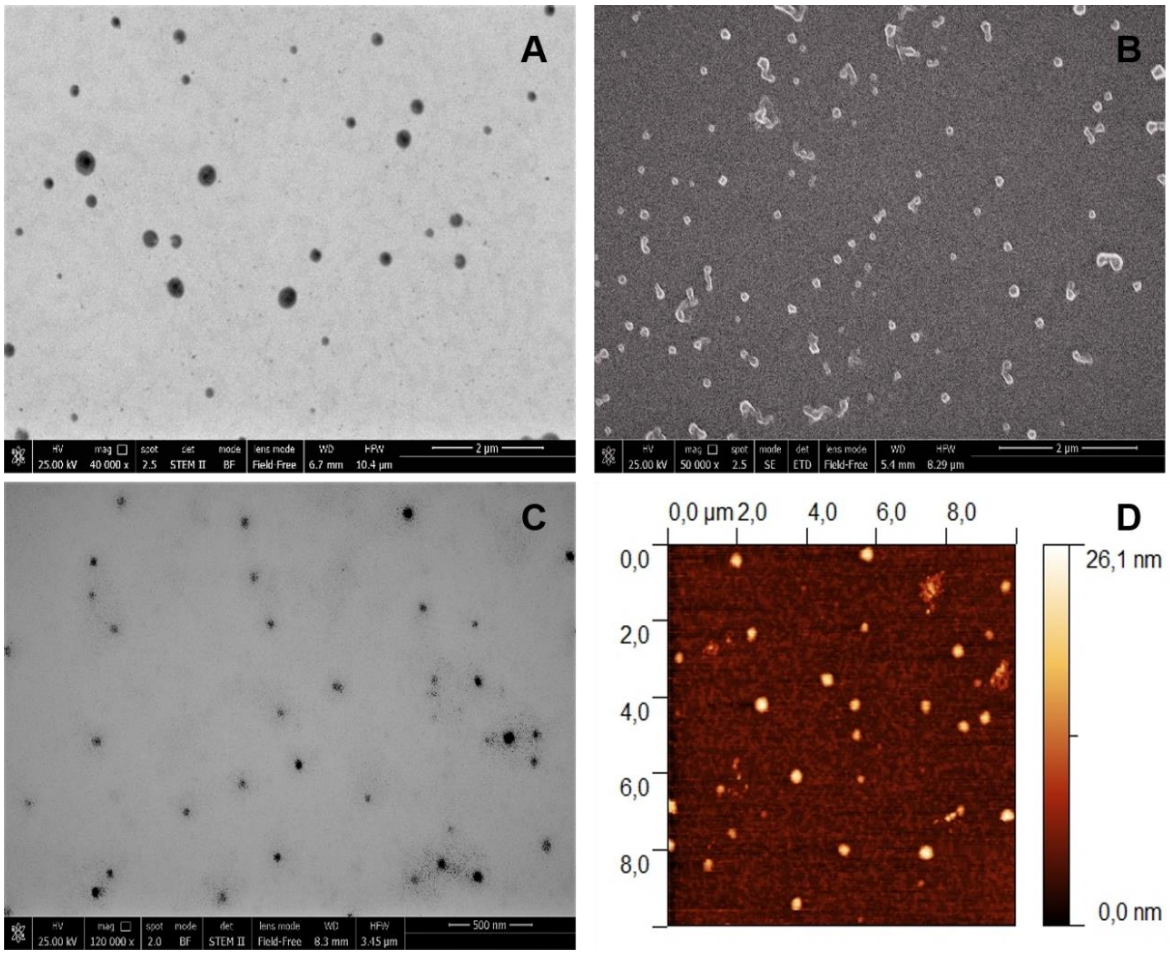

Figure 5. Microscopy images of GER-UDCA nanoparticles showing a spherical shape and size homogeneity. A-B: Trasmission electron microscopy (TEM) and Scanning electron microscopy (SEM) images of GER-UDCA-NPs C-D: TEM and atomic force microscopy (AFM) images of GER UDCA-SLNs.

In vitro release experiments demonstrated a low dissolution rate of free GER-UDCA, where less than 10% of the prodrug was dissolved in 8 h. On the other hand, GER-UDCA release from nanoparticles showed a high and quick burst effect of approximately 29% and 68% at 15 min for GER-UDCA-NPs and GER-UDCA-SLNs, respectively (Figure 6). In addition, the overall GER-UDCA released within 8h from NPs was about 40%, while for SLNs a minimum increase of prodrug release was observed over time, following the burst effect. However, the cumulative release of GER-UDCA from SLNs within 8h was about 35% higher than NPs, mainly due to initial burst effect.

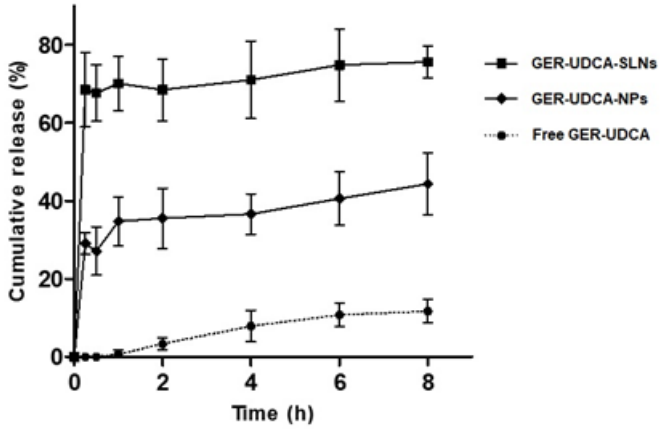

Figure 6. *In vitro* cumulative GER-UDCA release from formulations in aqueous medium with 5 mM SDS at 37°C (n=3). Data represent mean ± SD.

3.4. In vivo GER and GER-UDCA-loaded SLNs nasal administration.

GER was nasally administered at the dose of 4 mg/kg as emulsified formulation in a mixture of glycerol and water. Figure 7 reports the GER concentrations detected during time in CSF of rats, following the nasal administration. The GER values detected were 4.3 ± 0.70 and 2.16 ± 0.32µg/mL at 30 and 60 min, respectively, as evidenced in the inset of Figure 7. However, a drastic increse of GER concentration was evidenced in CSF at 90 min, (122 ± 15 µg/mL) whose value appeared up to 56 times higher than those detected at 30 or 60 min. These data suggest that the GER ability to permeate across olfactory mucosa drastically increased after 1h of its presence in the nasal cavity of rats.

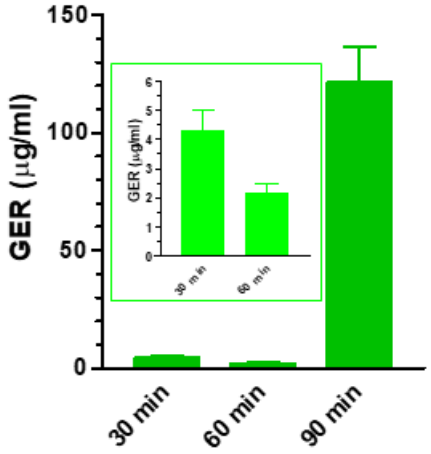

Figure 7. GER concentrations (µg/mL) detected in the CSF of rats after nasal administration of a 1 mg dose as emulsified formulation in a mixture of glycerol and water. Data are expressed as the mean ± SD of at least four independent experiments.

GER-UDCA-SLNs demonstrated not only a high EE% but also the ability to induce a fast release of GER-UDCA. Therefore, GER-UDCA was nasally administered at the dose of 2 mg/kg as a water suspension of GER-UDCA-SLNs in order to verify its potential uptake in the CNS.

The GER-UDCA-SLNs nasal administration produced detectable amounts of GER-UDCA in the CSF of the rats, as reported in Figure 8. In particular, the GER-UDCA concentrations in the CSF were 4.65 ± 0.52 µg/mL at 30 min then the concentration values slowly decresed to 1.1 ± 0.10 µg/mL at 150 min after nasal administration. After 180 min the GER-UDCA concentration was not detectable. No GER amounts were detected in CSF of rats wihin 180 min after nasal administration of the SLNs. Moreover, no GER or GER-UDCA amounts were detected in the bloodstream within 180 min after nasal administration of the particles. The AUC value in CSF obtained by nasal administration of GER-UDCA-SLNs (500 µg of GER-UDCA for rat) was 389 ± 15 µg·mL-1·min (736 ± 28 µM · min).

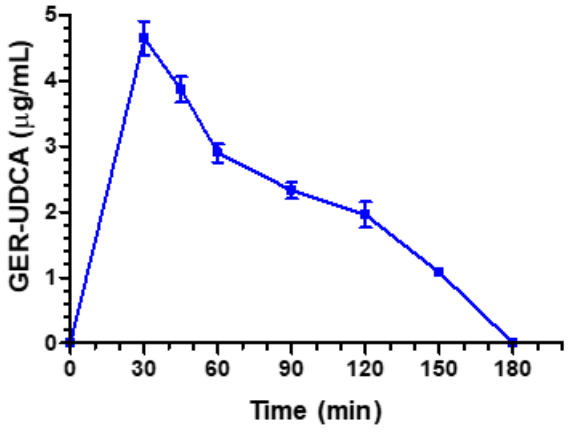

Figure 8. GER-UDCA concentrations (µg/mL) detected in the CSF of rats after nasal administration of a 500 µg dose as GER-UDCA-SLNs . Data are expressed as the mean ± SD of at least four independent experiments.

3.5 Histopathological examinations of nasal mucosae

The histopathological evaluation of rat nasal mucosae was performed after 2 h from the intranasal administration of free GER, GER-UDCA-SLNs, PBS 7.4 and isopropyl alcohol (Figure 9). No signs of damage were detected on the nasal mucosa after the administration of both PBS 7.4 (negative control, Figure 9A) and GER-UDCA-SLNs (Figure 9C), since a well-preserved epithelial lining of the olfactory region was evident. On the contrary, after the administration of both the positive control (isopropyl alcohol, Figure 9B) and free GER (Figure

9D), a separation of pseudostratified columnar epithelium from basement membrane was observed.

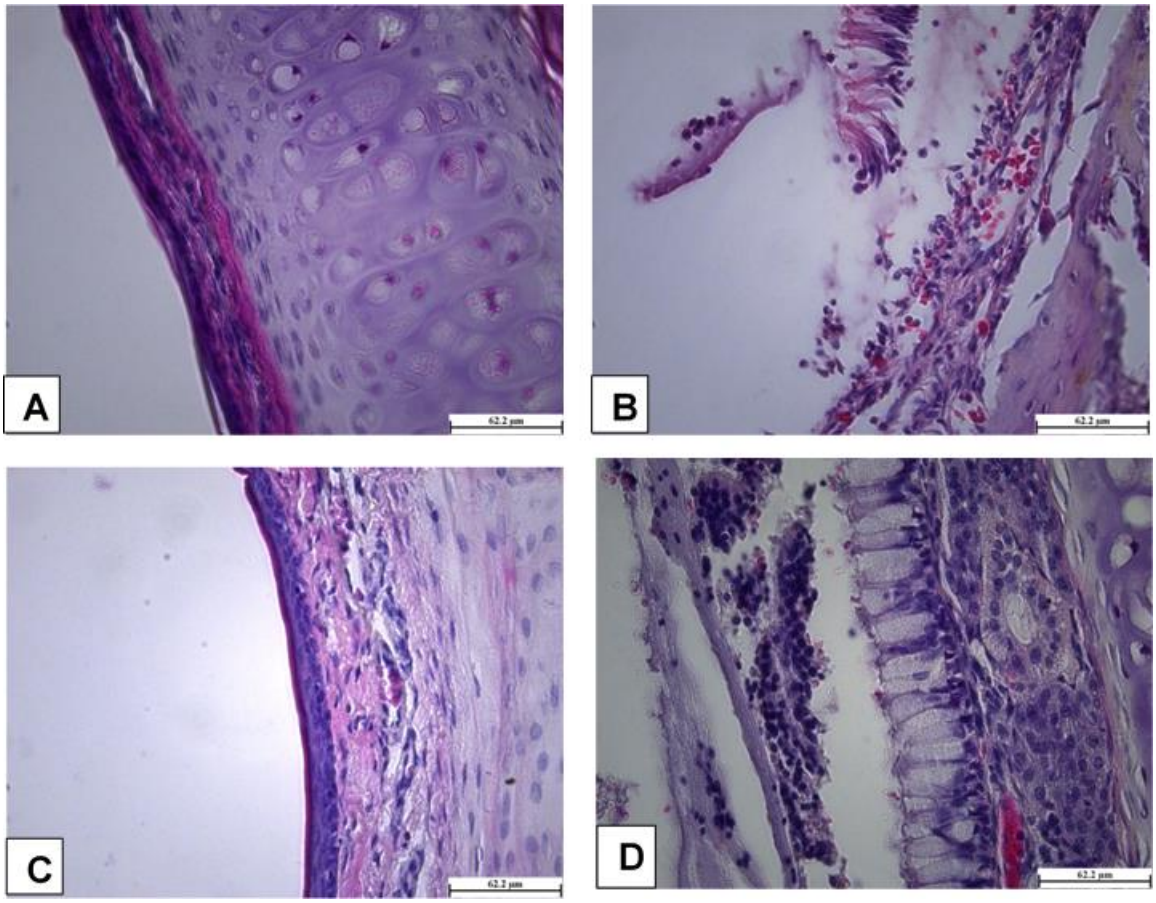

Figure 9. Representative histological sections of nasal mucosae of rats 2 h after intranasal administration of (A) PBS 7.4 (as negative control), (B) isopropyl alcohol (as positive control), (C) GER-UDCA-SLNs and (D) free GER. Magnification: 40X. Scale bars = 62.2 µm.

4. FIRST STRATEGY: DISCUSSION

Therapeutic strategies able to counteract neuroinflammation or to protect mitochondrial functions appear promising in preventing and reducing progression of PD. Recently, natural compounds such as GER and UDCA have been proposed as new promising drugs against PD. Both GER and UDCA permeate in the CNS from the bloodstream and their ability to reach the cerebrospinal fluid has been recognized [159,171,172]. Therefore, their neuroprotective effects can be achieved after oral administration, even though high doses are required (up to 200 mg/kg or 50 mg/kg per day for GER or UDCA, respectively) [158,171]. Moreover, GER shows a very short half-life (about 12 min) at systemic and central levels in rats [159]. These aspects could compromise the use of these potential natural drugs for long-term therapies against PD.

Taking into account the features of GER and UDCA, we have provided their ester conjugation to obtain a prodrug of both these compounds, which can be released by GER-UDCA hydrolysis induced by appropriate esterases [173].

The prodrug approach has been proposed as a useful strategy in order to avoid the clinical limitations related to the therapies based on some neuroactive drugs [174,175]. As an example, this strategy allows to circumvent the active efflux transporters expressed on the BBB [170], and it can prolong the activity of drugs with short half-lives [176]. Nose-to-brain administration represents an interesting strategy to directly deliver a neuroactive agent in low doses to CNS, bypassing both the BBB and the first-pass metabolism.

The conjugate GER-UDCA showed high stability in Tris-HCl buffer. On the other hand, in rat liver or brain homogenates the conjugate was hydrolyzed, evidencing its aptitude to release GER and UDCA in physiologic environments. The lower hydrolysis rate of the prodrug in brain homogenates with respect to liver homogenates suggests that GER-UDCA may induce a controlled release of GER and UDCA in the CNS, allowing their prolonged activity during time. Moreover, GER-UDCA demonstrated to overcome GER limitations in nose-to-brain administration. Here, we have evidenced this aspect, considering the effects of GER nasal administration (4 mg/kg) to rats, as a water emulsion in the presence of glycerol. GER concentrations in the CSF ranged between ~2 and ~4 μg/mL within 60 min after the nasal administration, and at 90 min suddenly increased to ~120 μg/mL, suggesting a drastic change of permeability of nasal mucosa. In line with this scenario, the histopathological analysis of nasal mucosa of rats evidenced serious mucosal damages 120 min after the administration of this GER emulsion (Fig. 9D). Finally, the relative high volatility of GER seems to preclude its encapsulation in polymeric or lipid nanoparticulate systems. Lipid-based (SLNs), obtained with compritol, and polymeric (NPs) nanoparticles, based on PLGA, were prepared by melt-emulsification with solvent evaporation and nanoprecipitation techniques, respectively, to obtain particles in the nanometric range. Compritol is composed by glycerol mono, di- and tri-behenate and it was selected for its high biocompatibility [177] as well as PLGA polymer, approved by FDA for formulation development [178]. For GER-loaded nanoparticles drug content was relatively high before freeze-drying, but following this process it appeared negligible, regardless the kind of matrix material. In fact, neither the employment of the non-volatile oils (isopropyl myristate and triacetin) nor the addition of an external coating (chitosan or gelatin) were able to reduce GER escaping during the freeze-drying process. The negligible GER content might be due to GER sublimation during lyophilization. In fact, GER presents a melting point around −15 °C which is exceed during freezing process.

The use of mannitol and trehalose as cryoprotectant was tested (data not shown), in order to prevent potential particle aggregation and fusion and to protect the nanoparticles from the mechanical stress of ice crystals [179]. Unfortunately, this strategy did not avoid GER loss, suggesting that this phenomenon is due to GER volatility.

Differently from GER, the prodrug GER-UDCA is not a volatile compound and it appears semisolid with a very low water solubility. These last properties make difficult its intranasal administration in the free form. Consequently, biocompatible delivery nanocarriers for the nose-to-brain delivery of GER-UDCA were designed and developed with the same procedures and materials used for GER encapsulation. GER-UDCA-SLNs, based on compritol, and GER-UDCA-NPs, based on PLGA, demonstrated an average diameter below 200 nm with a negative charge. The negative zeta potential may be attributed to lipid and polymer nature, which guarantees their physical stability. For a nose-to-brain delivery of nanoparticles, both size and zeta potential influence and determine the brain distribution of drugs. Particles around 100 nm have been demonstrated to increase brain drug concentration compared to other administration routes [180,181]. Regarding the superficial charge, the issue is controversial. The drug absorption is influenced by a large number of different parameters that makes difficult to compare different results. Overall, both negative and positive charged nanoparticles have been established to increase brain drug concentration compared to other routes or to drug solutions [180–182].

High EE% of the lipophilic GER-UDCA in both nanocarriers used in this study were obtained, consistent with the expectative. In fact, during nanoprecipitation lipophilic drugs do not migrate to aqueous phase but interact with the polymeric matrix where they are encapsulated [183]. In the case of SLNs, the evaporation of organic solvent spontaneously occurs in precipitation of lipids along with the drug, since lipophilic compounds generally show higher affinity for the lipid dissolved into organic phase, than for water [184]. Nevertheless, DL% values showed that the use of GER-UDCA was efficient to improve the amount of GER in the freeze-dried nanoparticles, confirming the reduction of GER volatility when conjugated with UDCA.

In vitro release data showed a higher dissolution rate of GER-UDCA from our formulations compared to the free prodrug in its semisolid form. In particular, GER-UDCA-SLNs demonstrated a high and quick burst effect, suggesting the localization of GER-UDCA on the surface of SLNs rather than entrapped in lipid matrix. On the other hand, the ability of NPs to better control the prodrug release, evidences higher core distribution of GER-UDCA than in SLNs. Overall, it is important to remark that the high concentration of surfactants used for SLNs manufacturing may contribute to accelerate drug release from the nanoformulations [185].

Rapid or prolonged therapeutic effects may be therefore obtained by the different release patterns of SLNs and NPs that allow to deliver the prodrug at different rates. SLNs were selected as suitable formulation for nasal administration, due to their ability to promote a prompt dissolution of the prodrug.

Following the administration in the rat nostrils of the GER-UDCA-SLNs suspension, GER and prodrug concentrations in CSF and bloodstream were measured. It was not possible to perform a comparison with raw GER-UDCA, being semisolid and highly adhesive.

SLNs induced the uptake of the prodrug in the CSF, reaching concentrations up to ~5 μg/mL within 30 min after nasal administration. These data confirm the ability of GER-UDCA-SLNs to deliver in the olfactory region prodrug amounts ready to be targeted in the CSF, probably by promoting its dissolution rate. Interestingly, no GER or GER-UDCA amounts were detected in the bloodstream of rats. This result emphasizes the ability of SLNs to promote a selective uptake of GER-UDCA in CSF, indicating a direct nose-to-brain pathway for this prodrug.

Moreover, following the nasal administration of the SLNs, GER-UDCA permanence in CSF appeared sensibly prolonged (about 2 h) in comparison to GER permanence in CSF administered by oral way [159].

It may be intersting to observe that the GER-UDCA AUC value in CSF of rats (736 ± 28 μM·min) obtained after nasal administration of SLNs is significantly higher ($P < 0.001$) than that obtained by the oral administration of 12,5 mg of GER (473 ± 23 μM·min) [159], a dose about 100 times higher, in molar terms, than that of the prodrug nasally administered.

GER absence in CSF, following the nasal administration of GER-UDCA, suggests that the prodrug hydrolysis can be localized in the brain parenchima, as evidenced by the prodrug hydrolysis detected in rat brain homogenates.

Finally, the histopathological examinations of nasal mucosa highlighted the safety of the intranasal administration of GER-UDCA-SLNs in comparison to free GER and isopropyl alcohol (positive control). Indeed, neither mucosa damage nor alteration in the epithelial lining were observed, as the integrity of both the pseudostratified columnar epithelium and the basement membrane was maintained (Fig. 9C). These results indicate the high biocompatibility of GER-UDCA-SLNs with respect the GER nasal formulation.

5. FIRST STRATEGY: CONCLUSIONS

To achieve brain targeting via intranasal administration, we propose lipid nanoparticles containing a new prodrug obtained by the conjugation of GER with UDCA, two natural compounds known to prevent and counteract PD. Even though *in vitro* experiments

demonstrated the ability of the prodrug to be hydrolyzed in physiologic environments, its sticky consistence and very poor solubility hindered its intranasal administration. The encapsulation of GER-UDCA in polymeric or lipid nanoparticles induced a significant increase of its dissolution rate in aqueous solvent. In particular, nasal administration of GER-UDCA-SLNs demonstrated the ability of the SLNs to induce prodrug permeation from nose to CSF of rats, without inducing mucosal irritation. In conclusion, these data suggest the ability of this formulation to provide an effective noninvasive approach to achieve the access of GER and UDCA to the brain for treatment of PD. Future experiments in animal PD models are needed to demonstrate the efficacy of this therapeutic approach.

6. SECOND STRATEGY: MATERIALS AND METHODS

6.1 Materials

Geraniol (GER) (purity: 99%) was purchased from Acros Organics (Geel, Belgium). β-cyclodextrin (βCD) and (2-Hydroxypropyl)-β-cyclodextrin (HPβCD) were obtained from CycloLab (Budapest, Hungary). All the other chemicals were of analytical grade.

6.2 Preparation of the inclusion complexes

The inclusion complexes GER-CD were prepared by solvent evaporation method followed by freeze-drying. βCD or HPβCD were dissolved in water under magnetic stirring until clear solutions were obtained. Then, a solution of GER in acetonitrile (ACN) was added. The mixtures were stirred overnight to remove the organic solvent. Finally, the inclusion complexes formed were freeze-dried for 24 h (Lio 5P, Cinquepascal, Milano, Italy).
The CD concentration in water and the percentage of the organic solvent (ACN) were modified in order to optimize GER inclusion in CDs. Table 4 shows the composition of various batches.

Table 4. Composition of various batches of GER-CD inclusion complexes. Each batch was prepared in triplicate.

Sample	CD in water (mg/mL)	ACN in water (%, V/V)	GER:CD molar ratio	Freezing temperature
GER-βCD-1	17	20	1:1	− 20 °C
GER-βCD-2	17	10	1:1	− 20 °C
GER-HPβCD-1	17	20	1:1	− 20 °C
GER-HPβCD-2	17	10	1:1	− 20 °C
GER-HPβCD-3	34	10	1:1	− 20 °C
GER-HPβCD-4	50	10	1:1	− 20 °C
GER-HPβCD-5	100	10	1:1	− 20 °C

6.3 HPLC analysis

The system consisted of two PU-2080 Plus pumps, an HG-980-30 solvent mixing module and a UV-2075 Plus UV–VIS detector; data were recorded and processed by Hercule Lite Chromatography Interface and Borwin Software, respectively (Jasco Corporation, Tokyo, Japan). Manual injection was performed by a Rheodyne 7725i injection valve (IDEX Corporation, Rohnert Park, CA, USA); the mobile phase was degassed during use by a solvent degasser (Degasys DG- 1210, Uniflows Co., Ltd., Tokyo, Japan). Chromatographic analyses

were performed on InertClone ODS column (150 x 4.6 mm; 5.0 µm) equipped with an ODS guard column (4.0 × 3.0 mm; 5.0 µm) (Phenomenex, Bologna, Italy) with a mobile phase of (A) water and (B) ACN using the following gradient program: 0.0–8 min, isocratic at 55% (B); 8–9 min, linear gradient from 55 to 90% (B); 9 to 15 min, isocratic at 90% (B); 15 to 16 min, linear gradient from 90 to 55% (B). A pre-equilibration period of 14 min was used between each run. The flow rate was 1.0 mL/min and the column temperature was 30 °C. The injection volume was 10.0 µL and the column eluates were monitored at 210 nm.

Plasma and cerebrospinal fluid (CSF) GER concentrations were quantified by HPLC. The chromatographic apparatus consisted of a modular system (model LC-10 AD VD pump and model SPD-10A VP variable wavelength UV−Vis detector; Shimadzu, Kyoto, Japan) and an injection valve with a 20 µL sample loop (model 7725; Rheodyne, IDEX, Torrance, CA, USA). Separations were performed at room temperature on a 5-µm Hypersil BDS C-18 column (150 mm × 4.6 mm *i.d.*; Alltech Italia Srl, Milan, Italy) equipped with a guard column packed with the same Hypersil material. Data acquisition and processing were performed on a personal computer using CLASS-VP Software, version 7.2.1 (Shimadzu Italia, Milan, Italy). The detector was set at 210 nm; the mobile phase consisted of an isocratic mixture of water and acetonitrile at a ratio of 60:40 (v/v). The retention times obtained were 10.5 min for GER and 16.0 min for carbazole, used as internal standard for the quantification of geraniol in blood samples (see below).

The chromatographic precision, represented by relative standard deviations (RSD), was evaluated by repeated analysis (n = 6) of the same sample dissolved in a mixture of acetate buffer 100 mM (pH = 4) and acetonitrile 5:95 (v/v) containing GER at a concentration of 500 µM (77.1 µg/mL). The RSD value was 0.88%. Geraniol was quantified by the peak area correlated with the predetermined standard curve over the range 1 -1000 µM (0.154 -154 µg/mL). The calibration curve was linear (n= 12, r = 0.996, $P < 0.001$).

For CSF simulation, standard aliquots of balanced solution (PBS Dulbecco's without calcium and magnesium) in the presence of 0.45 mg/mL BSA were used [168,169]. For the GER assay in CSF, the chromatographic precision was evaluated by repeated analysis (n = 6) of the same sample solution containing 500 µM (77.1 µg/mL) geraniol (RSD = 0.96 %) in simulated CSF and calibration curves of peak areas *versus* concentration were generated in the range 1 - 1000 µM (0.154 -154 µg/mL) and appeared linear (n = 12, r = 0.995, $P < 0.001$).

Recovery experiments of 500 µg/mL (77.1 µg/mL) GER from rat whole blood were performed by comparing the peak areas extracted from blood test samples (see below) at 4 °C (n = 6) with those obtained by injection of an equivalent concentration of analyte dissolved in its mobile

phase. The average recovery ± SD was 65.2 ± 3.4%. The concentrations of this compound were therefore referred to as peak area ratio with respect to the internal standard carbazole. The precision of the method, evaluated by replicate analyses (n= 6) of rat blood extract containing the internal standard (carbazole) and GER at a level of 77.1 μg/mL, was demonstrated by the RSD value of 1.14%. Calibration standards were prepared by spiking blood extracts with the internal standard (carbazole) and with known amounts of GER corresponding to blood concentrations in the range 10 - 1000 μM, (1.54 -154 μg/mL) at 4°C. These solutions were analyzed by HPLC and the calibration curve of peak area ratios *versus* concentrations was linear (n= 9, r = 0.993, P < 0.001).

A preliminary analysis performed on blank CSF and blood samples showed that their components did not interfere with the GER and carbazole retention times.

6.4 Drug loading and inclusion efficiency

To determine GER amount complexed by CDs, 5 mg of each freeze-dried sample were placed in a tube and dissolved in a ACN:water solution (1:1). The solution was sonicated for 20 min in an ultrasonic bath (USC200TH, VWR collection, VWR Milano, Italy), filtered using a 0.45 μm syringe filter, diluted 1:5 and analyzed by HPLC.

The actual drug loading (DL%) and the inclusion efficiency (IE%) were calculated with the following equations:

$$DL\% = \frac{Incorporated\ GER\ (mg)}{Inclusion\ complex\ (mg)}\ x\ 100$$

$$IE\% = \frac{actual\ DL}{theoretical\ DL}\ x\ 100$$

Theoretical DL is calculated assuming a complete complexation (1:1 GER/CD ratio).

6.5 Phase solubility studies

Phase solubility studies were performed as described by Higuchi and Connors [186]. Briefly, an excess amount of GER (fixed at 16 mM) was added to 5 mL of CDs solutions at different concentrations (0-16 mM). The mixtures were kept at 20 °C under magnetic stirring during 24 h. An aliquot of each solution was withdrawn, filtered through a 0.45 μm syringe filter, diluted 1:1 with ACN, sonicated for 20 min in an ultrasonic bath (USC200TH) and finally analyzed by HPLC. Phase solubility diagrams were obtained by plotting the amount of solubilized GER (mM) as a function of CD concentration.

6.6 Inclusion complex characterization

The optimized inclusion complexes GER-βCD-2 and GER-HPβCD-5 were characterized with different techniques. For all the analyses, the physical mixtures (PMs), GER and the pure CDs were tested as comparison of the inclusion complexes GER-CDs. The PMs were prepared by mixing GER and the pure CD at 1:1 molar ratio.

6.6.1 Thermal Analysis

Thermogravimetry (TGA) and differential thermal analysis (DTA) curves were carried out with a thermobalance model DTG-60 (Shimadzu, Japan). The measurements were performed under dynamic nitrogen atmosphere (50 mL·min^{-1}) at heating rate of 10 °C·min^{-1} over the temperature range of 25–500 °C. About 3 mg of each sample were placed for each analysis into platinum pans.

6.6.2 Infrared Spectroscopy

The attenuated total reflectance-Fourier transform infrared (ATR-FTIR) spectra were obtained using a FT-IR spectrometer Spectrum Two equipped with Universal ATR sampling accessory (Perkin Elmer, Milano, Italy). The acquired spectral range was 4000-450 cm^{-1} with 4 scans and a resolution of 4 cm^{-1}.

6.6.3 Elemental Analysis

Elemental analysis was performed using Flash2000 analyzer (Thermo Fisher Scientific, Milano, Italy). About 2 mg of GER, pure CDs and their inclusion complexes were weighted in tin capsules and introduced into the combustion reactor.

6.6.4 Scanning Electron Microscopy

The morphology of the inclusion complexes was performed using an Environmental Scanning Electron Microscope (ESEM) (Quanta 200, Fei, Hillsboro, Oregon, USA). The pure CDs and their inclusion complexes (GER-HPβCD-5 and GER-βCD-2) were fixed on aluminium stubs using a double-side carbon tape and then vacuum coated with gold-palladium in argon atmosphere for 60 sec (Sputter Coater Emitech K550, Emitech Ltd, Ashford, Kent, UK).

6.6.5 NMR studies

Solution of pure CDs, GER and freeze-dried CD/GER complexes were obtained in D_2O (VWR, Milan, Italy) at the concentration of 1 mM. The solutions were transferred in WILMAD® NMR tube, 5 mm, Ultra-Imperial grade, L 7 in., 528-PP purchased from Sigma-Aldrich (Milan, Italy). All the acquisitions were performed at 25 °C and non-spinning. Spectra were recorded with a Bruker FT-NMR Avance III HD 600 MHz spectrometer (Bruker Biospin GmbH Rheinstetten, Karlsruhe, Germany). Chemical shifts were reported as δH (ppm) relative to 3-(trimethylsilyl) propionic-2,2,3,3-d4 acid sodium salt (TSP) (Sigma-Aldrich, Milan, Italy). ^{1}H NMR data were obtained with acquisition parameters as follow: time domain (number of data-points), 65536; acquisition time, 3.66 s; delay time, 20 s; number of scans, 8; dummy scans, 2; and spectral width, 14.9043 ppm (8944.54 Hz). Two-dimensional (2D) spectra were obtained with a Heteronuclear Single Quantum Correlation (HSQC) in order to confirm proton chemical shifts. The acquisition parameters for HSQC experiments (Bruker sequence "hsqcedetgp") were as follow: time domain, 2048 in the acquisition "or direct HSQC" dimension F2 (^{1}H) and 256 in indirect HSQC dimension F1 (^{13}C); spectral width 12 ppm (7211.54Hz) in F2 (^{1}H) and 70 ppm (10564.095Hz) in F1 (^{13}C);number of scans, 4; dummy scans, 16 acquisition time, 0.14 sec; delay time, 2 s.

The rotating-frame Overhauser effect spectroscopy (ROESY) was performed on GER/CD inclusion complexes with acquisition parameters as follow: pulse sequence "roesyphpr"; time domain, 2048 in F2 (1H) and 256 in indirect dimension F1 (^{1}H); spectral width , 10.01 ppm (6009.62 Hz) in F2 (^{1}H) and F1 (^{1}H) dimension; number of scans, 16; dummy scans, 16 acquisition time, 0.17 sec; delay time, 2 s and 300ms as Roesy spinlock pulse.

6.7 In vivo studies

6.7.1 Nasal administration on rats

Anesthetized adult male Sprague−Dawley rats (200- 250 g body weight) fasted for 24 hours and laid on their backs received a nasal administration of GER. The nasally administered dose was 1 mg/kg, obtained by introducing in each nostril of the rats 50 µL of a water suspension or a water solution containing, respectively the GER-HPβCD-5 or the GER-βCD-2 samples with amounts corresponding to about 100 µg of GER. The amounts were introduced using a semiautomatic pipet which was attached to a short polyethylene tubing inserted approximately 0.6–0.7 cm into each nostril. At the end of administration and at fixed time points, blood samples (100 µL) were collected and CSF samples (50 µL) were withdrawn using the cysternal

puncture method described by van den Berg et al. [166], which requires a single needle stick and allows the collection of serial (40–50 µL) CSF samples that are virtually blood-free [167]. A total volume of approximately 150 µL of CSF was collected during the experimental session. The CSF samples (10 µL) were immediately injected into the HPLC system for geraniol detection. The blood samples were extracted, immediately hemolyzed in Eppendorf tubes prefilled with 500 ml of water (HPLC grade, about 4°C), then 50 µL of 3M sodium hydroxide and 50 µL of internal standard solution (200 µM carbazole dissolved in a H_2O-MeOH mixture 50:50 v/v) were added. The samples were extracted twice with 1 ml of water-saturated ethyl acetate. After centrifugation (10 min at 13,000 x *g*), the organic layer was reduced to dryness by N_2 flow, then 150 µL of a H_2O:CH_3CN mixture (50:50 v/v) were added and, after centrifugation, 10 µl were injected into the HPLC system for GER and carbazole detection. The blood or CSF GER concentrations at the programmed time points were detected with four rats, following each type of nasal administrations.

All in vivo experiments were performed in accordance with the European Communities Council Directive of September 2010 (2010/63/EU). Any effort has been done to reduce the number of the animals and their suffering.

6.7.2 Histopathological examinations of nasal mucosa

The short-term effect of GER, GER-HPβCD-5 and GER-βCD-2 complexes on the structural integrity of nasal mucosa was evaluated on adult male Wistar rats weighing 250–300 g (obtained from the Central Animal Facility at Federal University of Goiás). Animals were acclimatized for a week prior to the beginning of experiments and kept under 12:12 h light-dark cycles at 25°C ± 1°C with food and water ad libitum. GER, GER-HPβCD-5 and GER-βCD-2 complexes, PBS 7.4 (as negative control) and pure isopropyl alcohol (as positive control) were administered intranasally in rats (n=3). Nasal administration was performed by introducing 50 µl of the sample in each nostril using a semiautomatic pipet, by inserting 0.6-0.7 cm of the attached polyethylene tubing into the nostrils. After 2h from the administration, the nasal mucosa was carefully removed. Tissues were washed in PBS, fixed in 10% v/v of formalin solution overnight and paraffin-embedded. Finally, slide samples (5 µm) were prepared using a microtome, stained with hematoxylin–eosin and observed under optical microscope (40x) to evaluate the mucosa integrity.

In vivo experiments were approved by the Federal University of Goiás (UFG) Animal Research Ethics Committee (protocol 38/18). Experimental protocols followed the principles for laboratory animal care and the Brazilian legislation (Law 11,794, October 8, 2008).

6.8 Statistical analysis

Statistical analysis of data was performed by two-way Analysis of Variance (ANOVA) test. Differences between groups were considered to be statistically significant at $p<0.05$.

7. SECOND STRATEGY: RESULTS

7.1 Drug loading and inclusion efficiency of inclusion complexes

The DL% and IE% of all the obtained formulations are displayed in Figure 10.

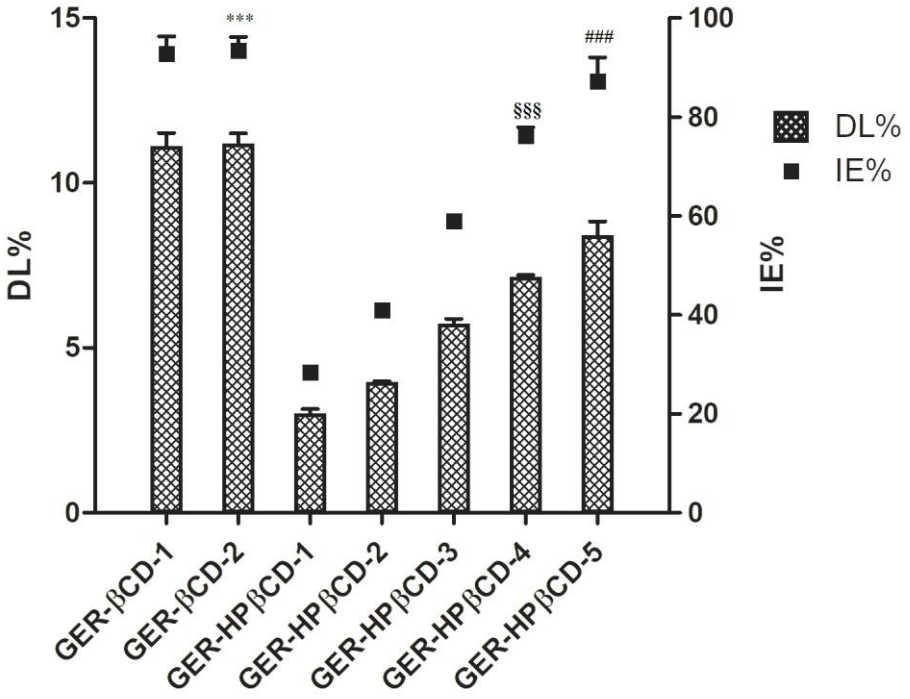

Figure 10. Drug loading (DL%) and Inclusion Efficiency (IE%) of the inclusion complexes prepared. For some points error bars do not exceed symbol size. *** $p<0.001$ *vs* all GER-HPβCD; §§§ $p<0.001$ *vs* GER-HPβCD-1, 2 and 3; ### $p<0.001$ *vs* GER-HPβCD-1, 2, and 3.

After the freeze-drying process, GER was quantified in all the inclusion complexes. The amount of the co-solvent ACN in water was of 10% while 20% was employed only for GER-βCD-1 and GER-HPβCD-1. In the case of βCD, the DL% of GER was not influenced by the amount of ACN employed in the formulation, whereas in the case of its hydrophilic derivative it was increased from 2.99 to 3.93 % for GER-HPβCD 1 and 2, respectively. Differences between the inclusion complexes obtained with the same formulation parameters (10% of ACN and 17

mg/mL of CD) but with different cyclodextrin were observed. In fact, GER-βCD-2 showed a GER content almost 3-fold higher than GER-HPβCD-2. Overall, GER complexation with the more hydrophilic cyclodextrin (HPβCD) demonstrated to be correlated to CD concentration in water. Indeed, a progressive increase of the DL and IE could be observed when greater concentrations of HPβCD was employed. In particular, to reach a similar IE% obtained for GER-βCD-2 an almost 6-fold higher HPβCD concentration was necessary (Table 4, GER-HPβCD-5).

Therefore, GER-βCD-2 and GER-HPβCD-5 resulted the inclusion complexes with the highest DL and IE% and these optimized samples were in depth characterized.

7.2 Phase solubility studies

Phase solubility studies were performed in order to examine the ability of the different CDs to solubilize GER (Figure 11). The intrinsic solubility S_0 of GER in water at room temperature (25°C) resulted of 3.83 mM. The phase solubility diagram showed the great ability of HPβCDs to increase linearly GER solubility, displaying an A_L-type profile [186]. In particular, increasing the concentration of HPβCDs up to16 mM the amount of solubilized GER increased linearly of 284.6%. On the other hand, the phase solubility diagram of GER in the presence of βCD showed the little ability of this CD to improve the solubility of GER, since it demonstrated a B_s-type profile in which the precipitation of the inclusion complex occurred. In particular, GER solubility appeared to be only slightly increased up to 4.6 mM by 0.6 mM βCD, with a solubility increase of 20.1% (Table 5). At further increase of βCD concentration, GER solubility decreased reaching a plateau in correspondence with the precipitation of the GER-βCD inclusion complex. From the initial linear segment of solubility profiles, a slope of 0.6545 and 1.1705 for HPβCD and βCD were calculated, respectively.

Table 5. Slope of linear diagrams from the phase solubility studies and increase solubility of GER in HPβCD and βCD solutions at different concentrations.

Cyclodextrin solution	GER experimental intrinsic solubility (S_0, mM)	Concentration range of cyclodextrin (mM)	Slope	Increase Solubility of GER (%)[a]
HPβCD	3.83	0-16	0.6545	284.6
βCD	3.83	0-0.6	1.1705	20.1

[a] The percentage difference between solubilized GER in observed concentration range of CDs with respect to S_0.

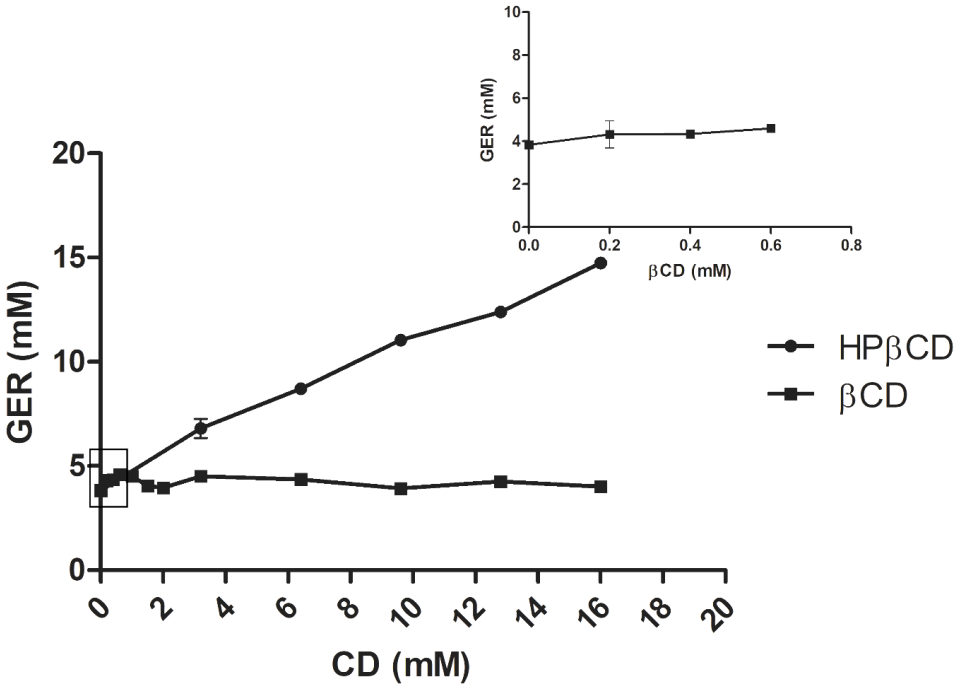

Figure 11. Phase solubility diagrams of βCD and HPβCD. For some points error bars do not exceed symbol size.

7.3 Inclusion complex characterization

TGA and DTA analyses were performed in order to verify both the formation of the inclusion complexes and the thermal stability of GER in the inclusion complexes (Figure 12).

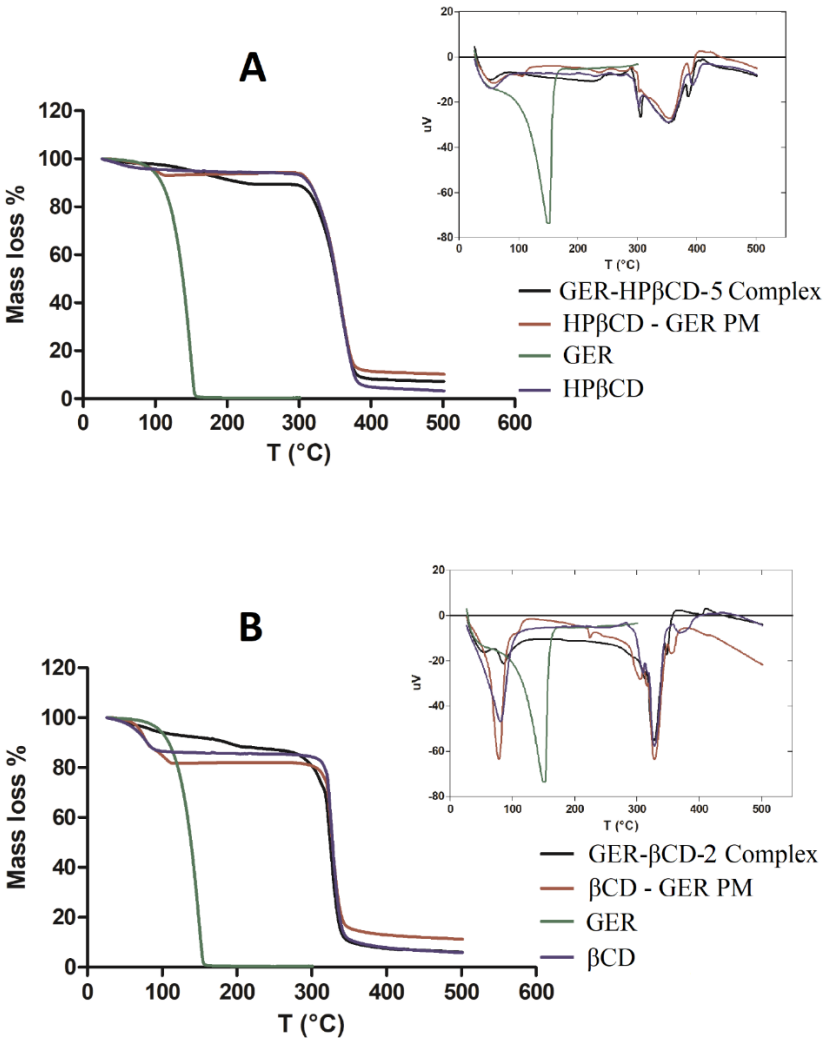

Figure 12. TGA and DTA curves of GER, pure βCD and HPβCD, the inclusion complexes and CDs-GER physical mixtures (PMs). A) HPβCD thermograms, B) βCD thermograms.

In both TGA thermograms of βCD and HPβCD, the mass loss (%) can be divided into two consecutive processes. The initial weight loss at below 100 °C was due to the release of water molecules from CDs cavities and to the evaporation of water on the surfaces. The mass loss was of about 12% and 5% for βCD and HPβCD, respectively. The major weight loss at around 300 °C for both CDs was related to a rapid CDs degradation followed by carbonization. TGA thermogram of GER showed a rapid weight loss from 70 °C to 170 °C. A little mass loss and thermal event (from DTA curve) related to GER could be appreciated for the PMs. In the case of TGA thermogram of the inclusion complexes, three steps of weight losses were observed. The first step was related to water evaporation below 100 °C (more accentuated for βCD complex due to its higher hygroscopicity), followed by the evaporation of complexed GER and CDs degradation at around 300 °C. GER evaporation in the inclusion complexes shifted from 70-170 °C to 170-220 °C due to the host-guest interaction.

FT-IR spectroscopy had been generally applied to prove the inclusion of guests into CDs cavities. The FT-IR spectra of GER, pure βCD and HPβCD and inclusion complexes are reported in Figure 13 A and B. GER spectrum was characterized by principal transmission peaks at 3322 cm^{-1} (free O-H stretching vibration), 2968 cm^{-1} (=C-H stretching vibration), 2916 cm^{-1} and 2857 cm^{-1} (C-H stretching vibrations), 1670 cm^{-1} (C=C stretching vibrations), and 1442 cm^{-1} and 1377 cm^{-1} (C-H bending vibrations). βCD spectrum showed transmission peaks at 3300 cm^{-1} (free O-H stretching vibration), 2918 cm^{-1} (C-H stretching vibrations), 1640 cm^{-1} (H-O-H bending vibrations of pure absorbed water), 1153 cm^{-1} (C-O stretching vibrations) and 1024 cm^{-1} (C-O-C stretching vibrations). HPβCD spectrum showed the characteristic bands at 3323 cm^{-1} (free O-H stretching vibration), 2926 cm^{-1} (C-H stretching vibration), 1641 cm^{-1} (H-O-H bending vibrations of pure absorbed water), 1152 cm^{-1} (C-O stretching vibrations), and 1080 cm^{-1} and 1023 cm^{-1} (C-O-C stretching vibrations). The FT-IR spectra of both GER-βCD-2 and GER-HPβCD-5 inclusion complexes with GER showed no features similar to pure GER.

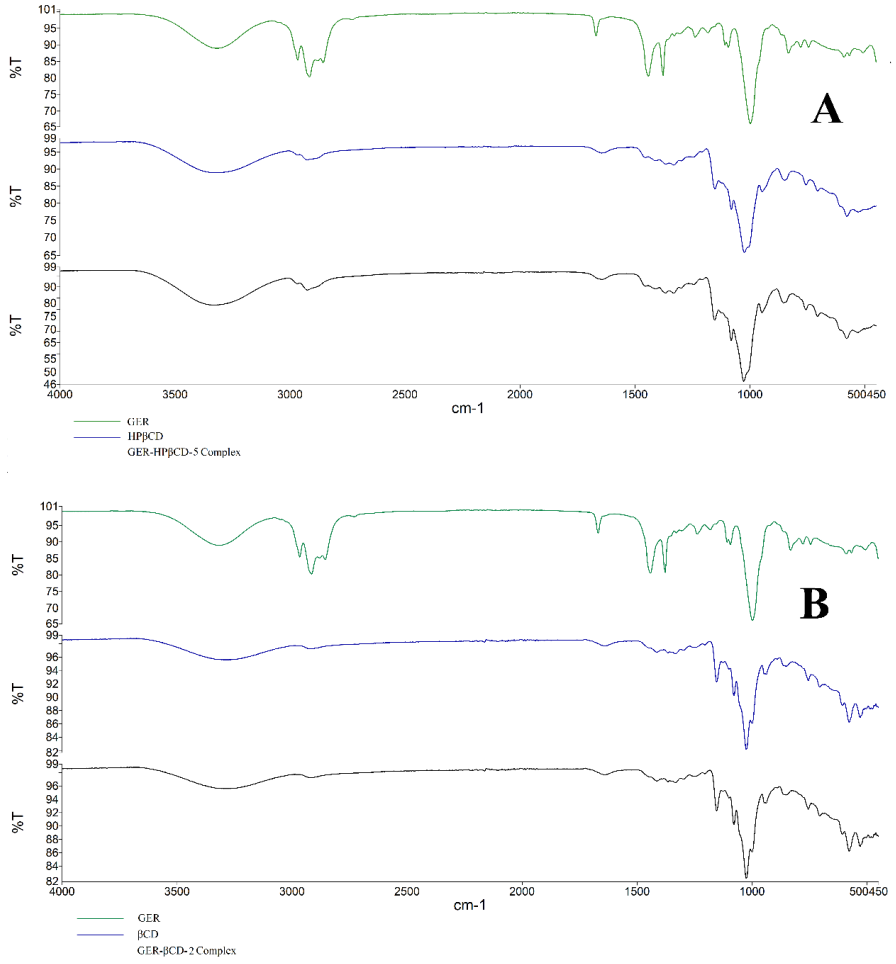

Figure 13. FT-IR spectra of (A) HPβCD, GER-HPβCD-5 complex and GER and (B) βCD, GER-βCD-2 complex and GER.

The elemental analysis was carried out in order to calculate the GER/CDs ratio in the inclusion complexes. The experimental results (expressed as percentage) and the theoretical percentages are reported in Table 6. The theoretical data were obtained by the molecular formula and molecular weight of each sample. For the inclusion complexes, the theoretical percentages were estimated for both 1:1 and 2:1 ratio, in order to understand which inclusion complex order was obtained during the formulations. For all the samples, the experimental percentages found from the analysis resulted to be slightly different to the theoretical ones. Therefore, for both CD inclusion complexes, comparing experimental data with the theoretical ones related to 2:1 and 1:1 ratios a first-order complexation was hypothesized, since the experimental and the calculated percentages of the 1:1 ratio presented the smallest difference.

Table 6. Elemental analysis of pure CDs, their inclusion complexes and GER.

Sample		Molecular formula	Experimental percentages	Theoretical percentages
HPβCD		$C_{63}H_{112}O_{42}$	C: 44.75 % H: 7.45 % N: 0 %	C: 49.09 % H: 7.33 % N: 0 %
βCD		$C_{42}H_{70}O_{35}$	C: 42.48 % H: 6.58 % N: 0 %	C: 44.44 % H: 6.22 % N: 0 %
GER		$C_{10}H_{18}O$	C: 77.38 % H:12.25 % N: 0 %	C: 77.86 % H: 11.76 % N: 0 %
GER-HPβCD-5 Complex	1:1 ratio	$C_{73}H_{130}O_{43}$	C: 44.92 % H: 7.56 % N: 0 %	C: 44.66 % H: 7.73 % N: 0 %
	2:1 ratio	$C_{83}H_{148}O_{44}$		C: 53.93 % H: 8.08 % N: 0 %
GER-βCD-2 Complex	1:1 ratio	$C_{52}H_{88}O_{36}$	C: 44.30 % H: 7.28 % N:0 %	C: 48.44 % H: 6.88 % N: 0 %
	2:1 ratio	$C_{62}H_{106}O_{37}$		C: 51.58 % H: 7.4 % N: 0 %

SEM microphotographs of raw material (HPβCD and βCD) and inclusion complexes solid systems are reported in Figure 14. HPβCD powder was composed of spherical porous particles with amorphous character [187](A), while βCD powder (B) presented large particles with irregular shape. The inclusion of GER into CD cavities induced a drastic change in morphology and shape of particles of both the naked CDs. In fact, GER-HPβCD-5 complex (C-D) exhibited

an big amorphous aggregates with sheet-like morphology, while GER-βCD-2 complex (E-F) showed little sheet-like amorphous structures [188].

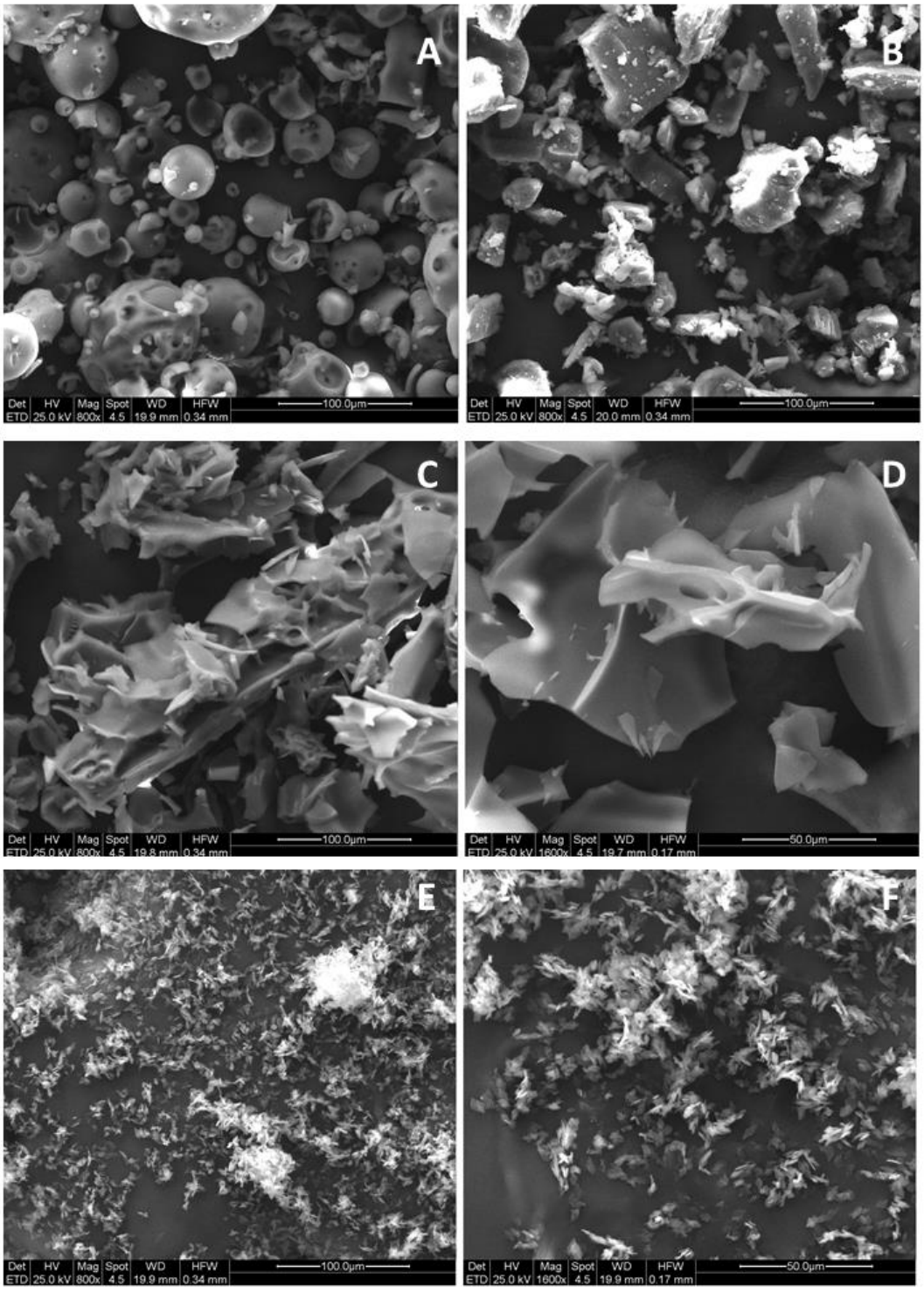

Figure 14. Scanning electron images of raw HPβCD (A) and raw βCD (B) at 800x magnification; GER-HPβCD-5 complex at 800x and 1600x magnification (C and D respectively); GER-βCD-2 complex at 800x and 1600x magnification (E and F respectively).

The formation of the inclusion complexes was also evaluated by NMR studies. ^{1}H NMR and 2D spectra were acquired for GER, HPβCD, βCD and the optimized inclusion complexes (Figure 15B and C). The schematic structure of both the CDs and GER are displayed in Figure 15A.

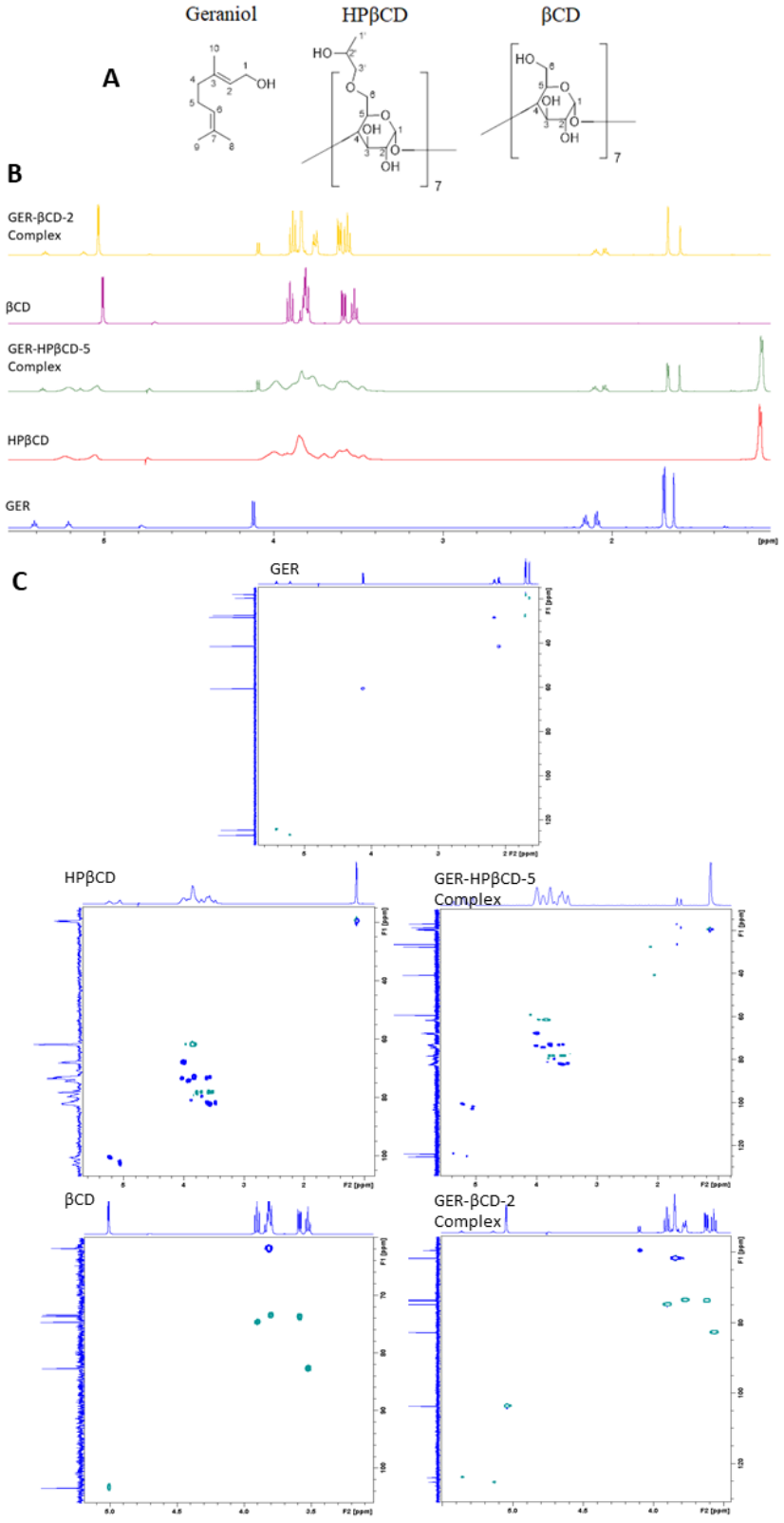

Figure 15. (A) Schematic structure of GER, HPβCD, βCD, (B) ^{1}H NMR spectra and (C) ^{1}H-^{13}C heteronuclear single quantum coherence (HSQC) of GER, HPβCD, GER-HPβCD-5 Complex, βCD and GER-βCD-2 Complex.

2D spectra were used for the correct assignment of each signal (Figure 15C). The chemical shifts in the protonic spectra of GER, HPβCD and βCD alone and in the inclusion complexes are summarized in Table 7 and 8. The induced shift Δδ, defined as the difference in chemical shift in absence and presence of the complexation was calculated by the following equation: $\Delta\delta = \delta_{Complex} - \delta_{Free}$.

Negative and positive signs of Δδ show a upfield and downfield shifts, respectively.

Table 7. Chemical shift of inclusion complexes relative to GER and HPβCD.

H	δ HPβCD	δ HPβCD Complex	Δδ HPβCD	δ GER	δ GER Complex	Δδ GER
1	5.055 5.239	5.058 5.241	0.003 0.002	4.119	4.111	− 0.008
2	3.615 3.560	3.634 3.566	0.019 0.006	5.413	5.382	− 0.031
3	3.919	3.901	− 0.018	-	-	-
4	3.471 3.590	3.493 3.601	0.022 0.011	2.089	2.061	− 0.028
5	3.825	3.778	− 0.047	2.162	2.125	− 0.037
6	3.847	3.851	0.004	5.212	5.161	− 0.051
8	-	-	-	1.637	1.622	− 0.015
9	-	-	-	1.699	1.695	− 0.004
10	-	-	-	1.689	1.687	− 0.002
1'	1.126	1.135	0.009	-	-	-
2'	3.989	4.001	0.012	-	-	-
3'	3.517 3.587 3.697 3.782	3.544 3.593 3.723 3.798	0.027 0.006 0.026 0.016	-	-	-

Table 8. Chemical shift of inclusion complexes relative to GER and βCD.

H	δ βCD	δ βCD Complex	Δδ βCD	δ GER	δ GER complex	Δδ GER
1	5.021	5.039	0.018	4.119	4.098	− 0.021
2	3.596	3.614	0.018	5.413	5.362	− 0.051
3	3.914	3.892	− 0.022	-	-	-
4	3.534	3.566	0.032	2.089	2.041	− 0.048
5	3.810	3.761	− 0.049	2.162	2.104	− 0.058
6	3.834	3.841	0.007	5.212	5.128	− 0.084
7	-	-	-	-	-	-
8	-	-	-	1.637	1.600	− 0.037
9	-	-	-	1.699	1.673	− 0.026
10	-	-	-	1.689	1.673	− 0.016

In presence of GER, for both HPβCD and βCD, all the protons were deshielded except for H3 and H5, which were shielded due to GER intercalation into the hydrophobic cavity. In the case of GER, in presence of both the CDs all the protons were deshielded. In particular, the protons H2, H4, H5 and H6 exhibited the highest Δδ.

The complexation stoichiometry ratio was calculated by comparing the integral area under the H1 peak for the CDs with that of H2 of GER. The intensity of the anomeric peak of CDs was arbitrary assigned to 1 and then the amount of GER was calculated. The stoichiometries of the inclusion complexes were obtained as follow [189]:

HPβCD intensity = 1 (seven protons)

βCD intensity = 1 (seven protons)

GER intensity = 0.1209 and 0.13 (one proton) in HPβCD and βCD Complex, respectively.

Ratio of intensities in HPβCD Complex: (0.1209/1)/(1/7) = 0.85

Ratio of intensities in βCD complex: (0.13/1)/(1/7) = 0.93

In order to obtain a more detailed structure of the complexes and the exact position of GER inside CD cavities, the Nuclear Overhauser Effect (NOE) was also evaluated. For this reason, ROESY pulse sequence was carried out to determine the NOE, which occurs between the protons of GER and those of the CDs [190]. 2D ROESY spectra of HPβCD and βCD complex are displayed in Figure 16.

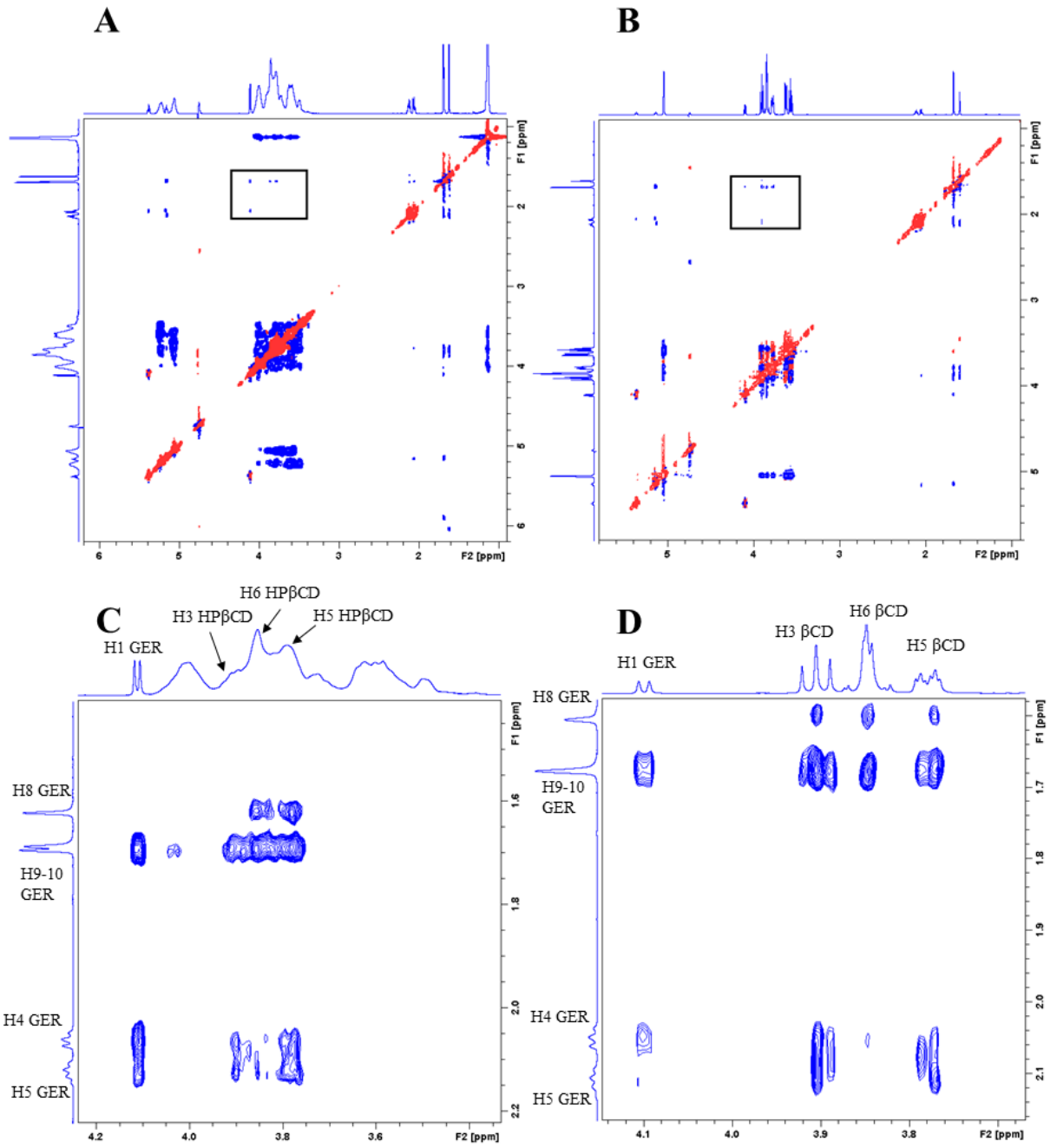

Figure 16. (A) ROESY spectrum of a D_2O solution containing 1 mM GER-HPβCD-5 Complex. (C) Expansion of the ROESY spectrum showing the ROE cross peaks between GER and HPβCD protons. (B) ROESY spectrum of a D_2O solution containing 1 mM GER-βCD-2 Complex. (D) Expansion of the ROESY spectrum showing the ROE cross peaks between GER and βCD protons.

The observed NOE cross correlations were the same for both the inclusion complexes. In particular, H3 and H5 of CDs showed NOE correlations with H4, H5, H8 and H9 or H10 (the signals are overlapped) of GER. Moreover, H6 of both the CDs exhibited cross-peaks only with the methyl groups H8 and H9 or H10. No other signals were highlighted.

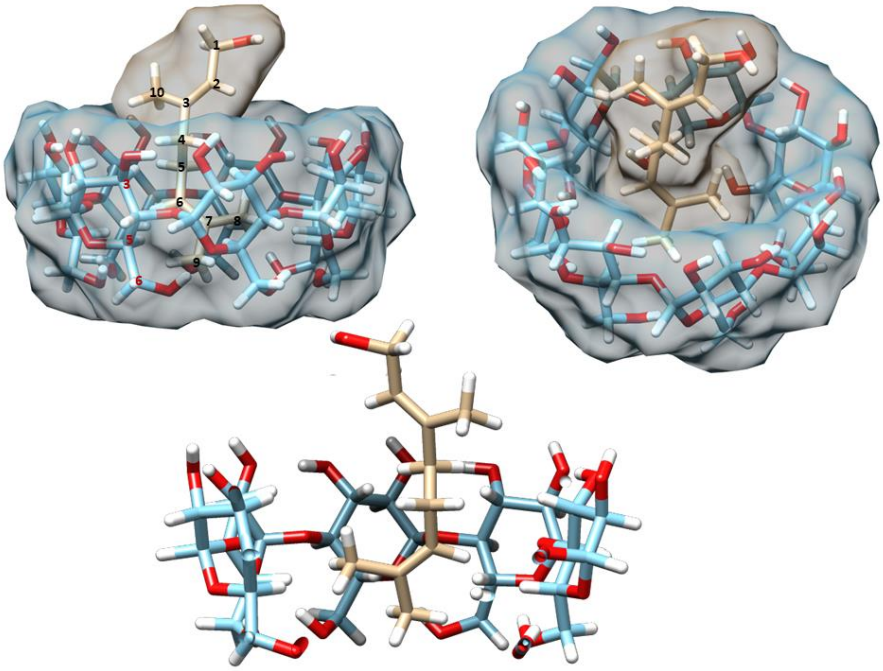

Figure 17. 3D Molecular representation of GER-CD complexes, based on NMR study. Hydrogens and oxygens are represented in white and red, respectively; carbons are represented in blue (CD) or brown (GER). Molecule numbering is represented in black for GER and in red for CD.

7.4 In vivo studies

7.4.1 In vivo GER-HPβCD-5 and GER-βCD-2 Complexes nasal administration

GER was nasally administered at the dose of 1 mg/kg contained in a water solution of GER-HPβCD-5 sample or a water suspension of GER-βCD-2 sample. Figure 18 reports CSF GER concentrations detected during time in rats, following the nasal administration of GER-HPβCD-5 or GER-βCD-2 samples which both allowed to obtain CSF drug uptake in rats. It is remarkable that great differences were evidenced by comparing GER amounts detected following nasal administration of GER-CD samples. In particular, Figure 18 indicates that GER-HPβCD allowed to detect rat CSF GER concentrations ranging from 1.25 ± 0.03 to 0.26 ± 0.03 µg/mL between 30 and 90 min following the nasal administration. On the other hand, GER concentrations detected in the same range of time, following the administration of GER-βCD were included between 12.6 ± 3.3 and 119.0 ± 8.6 µg/mL.

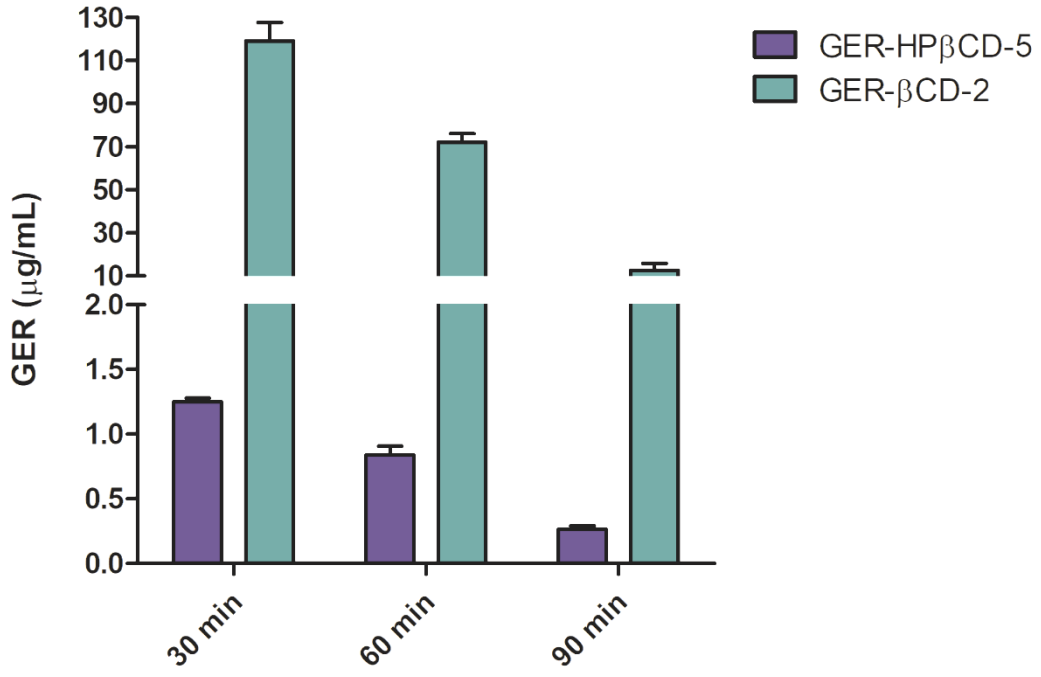

Figure 18. GER concentrations (μg/mL) detected in the CSF of rats after nasal administration of 1 mg/kg dose as water solution GER-HPβCD-5 sample or water suspension of GER-βCD-2 sample. Data are expressed as the mean ± SD of at least four independent experiments.

No plasma GER amounts were detected in rats within 90 min after nasal administration of GER-CD formulations, suggesting their ability to induce a selective uptake if GER in the CNS of rats.

7.4.2 Histopathological examinations of nasal mucosae

The histopathological evaluation of rat nasal mucosae was performed after 2 h from the intranasal administration of GER-HPβCD-5 and GER-βCD-2 Complexes, PBS 7.4 and isopropyl alcohol (Figure. 19). No signs of damage were detected on the nasal mucosa after the administration of PBS 7.4 (negative control, Figure 19A) and both GER-CD complexes (Figures 19 C and D), since a well-preserved epithelial lining of the olfactory region was evident. On the contrary, after the administration of the positive control (isopropyl alcohol, Figure 19B) a partial separation of pseudostratified columnar epithelium from basement membrane was observed.

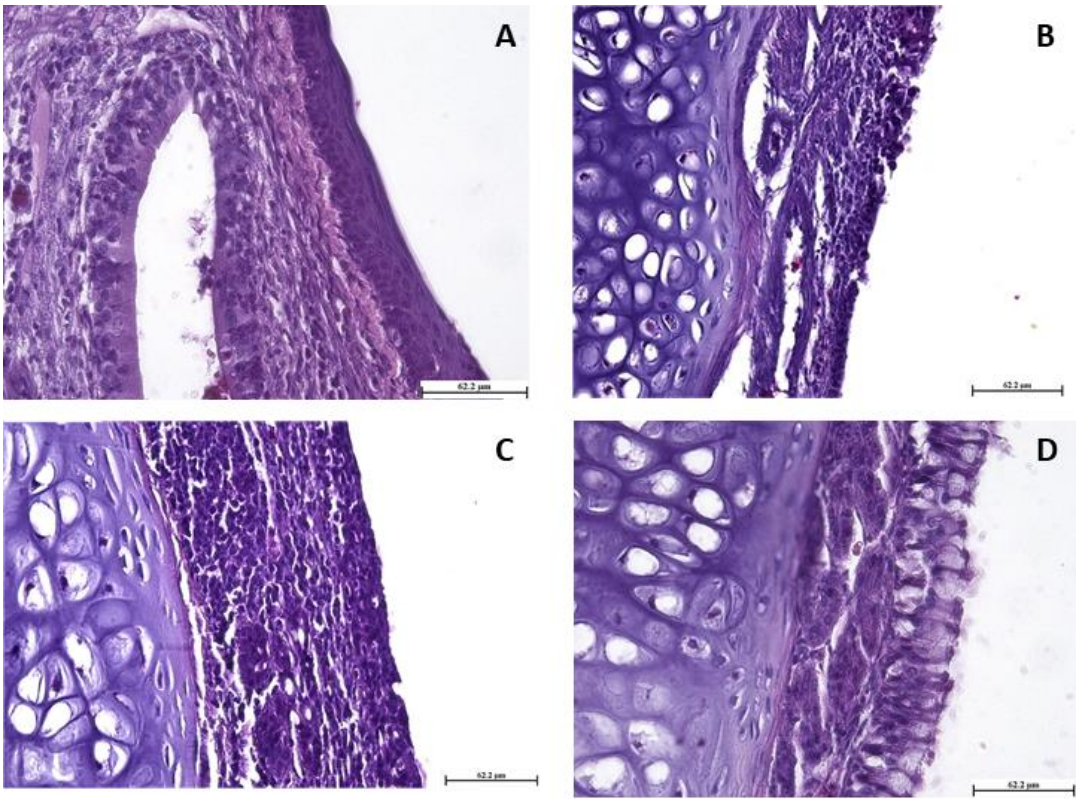

Figure 19. Representative histological sections of nasal mucosae of rats 2 h after intranasal administration of (A) PBS 7.4 (as negative control), (B) isopropyl alcohol (as positive control), (C) GER-HPβCD-5 Complex and (D) GER-βCD-2. Magnification: 40X. Scale bars = 62.2 μm.

8. SECOND STRATEGY: DISCUSSION

The aim the current project was to design and develop a biocompatible delivery carrier as long-term stable freeze-dried powder to deliver GER into the brain via nose-to-brain, without any damage to the nasal mucosa. Thus, inclusion complexes with the native βCD and its water-soluble derivative HPβCD were developed in order to challenge GER volatility. The majority of inclusion complexes with βCD and derivatives are obtained with a 1:1 drug:CD ratio [191]. Therefore, during the preparation, GER and CDs molarities were maintained equal. GER is a poor water-soluble compound and for this reason, ACN was used as co-solvent to enhance the interaction between the monoterpene and cyclodextrin hydrophobic cavities [192]. For βCD inclusion complex, the amount of ACN employed did not influenced the complexation of GER, while for HPβCD the reduction of the percentage of ACN from 20 to 10% increased the DL% from 2.99 to 3.93% (GER-HPβCD-1 and GER-HPβCD-2, respectively). The employment of high amount of co-solvent in the formation of GER-HPβCD inclusion complex probably led to a destabilization of the interaction between the hydrophobic cavity and GER. Therefore, in

HPβCD high percentages of ACN may promote the GER loss by evaporation instead of promoting GER inclusion [193].

GER amount in GER-HPβCD significantly increased by increasing the concentration of HPβCD in water. In fact, moving the concentration of HPβCD from 17 mg/mL to 100 mg/mL, the GER loading doubles from 3.9% to 7.6% (Figure 10). Therefore, CDs concentration in water solution is fundamental to obtain high complexation of the drug, since the excess of water in the preparation might reduce the contact between the guest and the host [194]. The concentration of HPβCD in water was not further increased due to the excessive solution viscosity. To explain why the optimized inclusion complex with HPβCD (GER-HPβCD-5) showed a lower drug loading compared to the optimized complex with βCD (GER-βCD-2), it is necessary keep in mind that HPβCD has higher molecular weight respect to βCD (1541.6 vs 1134.987 g/mol) and also that the steric hindrance given by the external hydroxypropyl chains determines a less inclusion complexation capability [195,196]. The phase solubility studies were performed following Higuchi and Connors method [186]. Through this analysis, several information regarding the inclusion complexes can be obtained, such as the molar ratio, the type of complex and the ability of CDs to increase the water drug solubility. Higuchi and Connors classified the complexes based on how the apparent solubility of a compound changes with increasing concentration of CDs. In particular, in aqueous solution A-type profiles are achieved when an increase of the compound solubility is obtained with increasing CD concentration through the formation of a soluble inclusion complex. On the contrary, B-type profiles are obtained when the compound solubility does not increase with increasing CD concentration, indicating the formation of poor soluble inclusion complexes. From the linear portion of the diagrams, the slope can be calculated. Generally, slope value less than 1 indicates the formation of a first-order complex, (i.e. 1:1 molar ratio inclusion complex). On the contrary, slope higher than 1 suggests the formation of higher-order complexes with respect to the compound, where more than one molecule of compound combines with the CD [186,197]. In this work, the solubility study of HPβCD with GER formed an A_L-type profile, suggesting that drug solubility linearly increased as a function of CD concentration, through the formation of a soluble inclusion complex. Moreover, the calculated slope from the linear portion of the diagram was less than 1 indicating the formation of a 1:1 first-order complex. In the case of βCD, a B_s-type profile was obtained, suggesting the formation of an insoluble inclusion complex from a concentration of CD 1mM. This result indicated the poor solubilizing effect of βCD on GER. A similar behavior was observed in phase solubility studies of βCD with several essential oils [198,199]. B-type profiles are mainly observed when the native CDs form

complexes with poorly-soluble compound. In the plateau region of the diagram, GER solubility is constant even when βCD concentration was increased, indicating the formation of an inclusion complex with a solubility lower than the pure CD [197]. The slope was calculated from the first part of the diagram where a linear increase of GER solubility was displayed, from 0 to 0.6 mM. The slope value resulted higher than 1 (1.1705), which is usually related to the formation of a higher order-complex [197]. However, slope higher than one can be observed also when the solubility of a compound is increased by the formation of non-inclusion complexes. In fact, the drug/CD complexes, particularly those of natural CDs (such as βCD), have tendency to self-assemble in aqueous solutions to give rise to aggregates. The formation of CD aggregates in aqueous solutions through non-inclusion complexation have been reported indicating that the aggregates can act as drug reservoirs which are able to enhance aqueous solubility of lipophilic drugs [200]. These aggregates at high CD concentrations can become large and precipitate as solid, as we observed in phase solubility study. A slope higher than one was also observed by Magnusdottir *et al.* for ibuprofen complexed with HPβCD. The higher-order complexation was excluded by complementary characterization methods, thus the formation of non-inclusion complexes was supposed [201]. Regarding GER/βCD interaction, we excluded the formation of a higher-order complex with a 2:1 (GER:CD) ratio by the results obtained from the elemental analysis, which suggested a 1:1 ratio. In fact, the elemental analysis demonstrated the formation of a first-order complexation. The experimental percentages of the elements were closed to the theoretical ones related to a 1:1 inclusion complex. In particular for βCD, this result excluded the possibility of a higher-order complexation. Therefore, we can suppose that in aqueous solution βCD forms with GER both inclusion complexes and non-inclusion complexes. The solubilized GER by the non-inclusion complexes is then lost by the freeze-drying process, due to the extreme volatility of GER. For all the samples analyzed, little differences between the experimental and the theoretical percentages could be appreciated. In the case of HPβCD, the differences were more marked due to the random substitution process of the external hydroxyl groups of βCD during HPβCD synthesis (manufacturer information). Thus, the exact molecular weight and the elemental percentage composition of HPβCD is not certain, leading to an approximated theoretical composition. For βCD, the differences might be imputable to the presence of residual humidity and crystallized water molecules. In fact, Wang *et. al* in their work demonstrated the presence of crystallized water molecules in βCD complexes crystals [202]. Moreover, the existence of humidity was also confirmed by TGA analysis. From the TGA thermograms, a weight loss for all the CDs and the complexes below the 100 °C was evident, supporting this hypothesis. TGA thermograms of βCD and HPβCD

showed the same profile with a little difference in the initial weight loss related to water loss, which is higher for βCD. This occurrence is might due to the higher hygroscopicity of βCD compared to its water-soluble derivative [203]. Furthermore, TGA results highlighted other important information in support of the real GER inclusion and the benefits related to the complexation. Differences among naked cyclodextrins (βCD and HPβCD), inclusion complexes and the physical mixtures (PMs) clearly demonstrated the formation of inclusion complexes. In fact, in TGA thermograms the weight loss related to GER shifted from 70-170 °C to 170-220 °C, highlighting CD ability to protect GER from thermal events. The same results were obtained with other volatile compounds and different kind of CDs [204–206]. No differences between the two types of CDs in GER protection were appreciated.

Finally, IR analysis also demonstrated the GER intercalation into CD cavities. In fact, the representative transmission peaks (1442 cm^{-1} and 1377 cm^{-1}) of GER were not detected in IR spectra of both βCD and HPβCD.

NMR spectroscopy is often used to characterize inclusion complexes since it can provide information regarding the effective presence of a guest into CD cavities. H3 and H5 protons of glucose units of CDs are facing the internal cavity, H6 is located in CD rim, whereas all the other protons are outside the cavity. Overall, if the chemical environment is affected by the inclusion of a guest in CD, the chemical shift of H3 and H5 will change significantly [207]. In order to confirm the occurrence of the inclusion complexes, ^{1}H NMR spectra of pure HPβCD, βCD, GER and their inclusion complexes were acquired. The results demonstrated a significant induced chemical shift in both HPβCD and βCD of H3 and H5, which moved upfield due to a shielding effect caused by the intercalation of GER and formation of Van der Waals interactions [208]. Moreover, Δδ of H5 was higher than Δδ H3, suggesting a complete insertion of GER into CD cavities [209]. An induced chemical shift was observed also for GER, in particular for the protons H2, H4, H5 and H6 confirming a variation of the chemical environment. The stoichiometry of the inclusion complexes, determined from the integral area, agreed closely with the IE% from the HPLC studies. Indeed, IE% was calculated considering the theoretical GER entrapment with a 1:1 CD:GER molar ratio.

A more detailed structure of the complexes was obtained by proton-proton NOE experiment. The presence of NOE cross correlation peaks between GER protons and CD protons indicated space coupling and confirmed the actual proximity of the two molecules (distance lower than 4 Å). First, the absence of any NOE cross correlation peaks between GER protons and H1, H2 and H4 protons of HPβCD demonstrated that no interaction between GER and the external surface of the CD occurred, not even with the isopropyl chain. The same result was obtained

for βCD, where GER protons did not display any cross correlation. On the contrary, for both the inclusion complexes intermolecular cross-peaks were observed for H3 and H5 of CDs and several GER protons (H4, H5 and H9 or H10).

^{1}H NMR and ROESY experiments were in agreement with GER intercalation into the CD cavities. In fact, the induced chemical shift was observed only for the internal protons of the CDs, demonstrating the absence of interactions between GER and the external surface of CDs. GER H9 or H10 cross-peak with H6 of CDs confirmed GER in-depth location into the cavities, near the narrow rim of the host. H9 and H10 signals could not be identified due to the peaks overlapping. However, considering the other NOE cross-peaks (H4, H5 of GER with both H3 and H5), H9 might be located near CD H6. This hypothesis is confirmed by the absence of cross-peaks and induced chemical shift for GER H1, indicating its distance from all the internal protons of CDs. Therefore, all these data suggest that GER is fully included into both CDs with its hydroxyl group located on the wide rim side, probably outside in close contact with water.

All these results demonstrated the formation after freeze-drying process of inclusion complexes between GER and CDs as well as the absence of GER on CDs surfaces. The certain of the absence of GER onto inclusion complex surfaces, was also given by our previous results. In fact, the incapability of nanoparticles in retaining GER after freeze-drying process was demonstrated (section 3.3). These results highlighted the suitability of CDs in protecting and avoiding the escape of volatile compounds in recovered formulation with the freeze-drying technique. The differences within the nanoparticles and the inclusion complexes could be attributed to the guest-host interactions able to molecularly separate GER molecules. Therefore, the non-included GER present in the freshly prepared formulation was simply removed by freeze-drying process owing to the high GER volatility. On the contrary, no evaporation of CD included-GER occurred since guest-host interactions molecularly separate GER molecules from each other [210].

Finally, the in vivo studies demonstrated the ability of both GER-CD complexes to directly deliver GER into the brain, avoiding the systemic circulation. Therefore, a direct nose-to-brain pathway could be supposed, through a transcellular transport from the olfactory epithelium to CSF, being GER a small and lipophilic molecule [211]. Moreover, the histopathological examinations confirmed the safety of the intranasal administration of both the inclusion complexes, in comparison to the positive control and free GER (Figure 19D, first strategy). However, the results highlighted huge differences in GER permeation in the CSF when administered with the two CD complexes. In particular, the amount of detected GER in the CSF after GER-βCD-2 complex administration was 100-fold higher than GER amount after GER-

HPβCD-5 complex administration. This dissimilarity can be explained by the different solubility of the two GER complexes. Natural CDs, such as βCD, due to their poor solubility in water lead to poor-water soluble complexes with the ability to self-assemble and precipitate as nano- or micro-aggregates [212]. This βCD behaviour was highlighted in the phase solubility study, where a slope higher than one suggested the formation of non-inclusion complexes, alongwith 1:1 GER-βCD inclusion comlexes. The non-inclusion complexes led to a self-aggregation of the inclusion complexes increasing GER water-solubility. βCD aggregates have been demonstrated to be able to quickly penetrate the hydrophilic mucosal layer [213]. On the contrary, hydrophilic CDs, such as HPβCD, poorly self-assemble showing a slow permeation of mucus layers, due to its high solubility in aqueous environments [214–216]. In fact, from the phase solubility studies, HPβCD-complexes did not demonstrate any self-assembly behaviour. In that, the differences in GER absorption might be explained by the fast mucus-penetration of GER-βCD-2 complex followed by GER release on epithelium surface, and by the clearance of the non-penetrated GER-HPβCD-5 complex from the mucosa.

9. SECOND STRATEGY: CONCLUSIONS

Two different cyclodextrins were employed to efficiently incorporate GER into inclusion complexes. Both the optimizes inclusion complexes (GER-HPβCD-5 and GER-βCD-2) were fully characterized under the physical-chemical point of view before the in vivo studies and demonstrated to beable to arise long-term stable powders, preventing GER loss during the freeze-drying process. After the nasal administration to rats, both the inclusion complexes demonstrated the ability to directly deliver GER into the CSF without inducing damage to the nasal mucosa. However, the higher GER concentration observed in cerebrospinal fluid after the administration of GER-βCD seems to be related to the different water solubility of the two complexes. Therefore, further studies are needed to clarify the mechanism of permeation of GER from the olfactory epithelium to the CSF and the cyclodextrin role as delivery systems.

CONCLUSIONS

This research project investigated the potentiality of biocompatible and biodegradable carriers for the delivery of different active compounds. Dealing with the safety concept, the materials employed in the formulation of the DDS are well-known and commonly used in pharmaceutical field.

The several lipid-based nanoparticles and cyclodextrin inclusion complexes developed demonstrated to be promising tool for the administration of drugs, through different routes: oral, pulmonary and intranasal. In fact, the developed carriers proved to be suitable for the delivery of both organic and inorganic active compounds, solid or liquid drugs. The technologies employed are appropriate for scale-up development.

In conclusion, lipid-based nanoparticles and inclusion complexes are valid “devices” for clinical application.

ACKNOWLEDGMENTS

This PhD thesis was performed in "Drug Delivery and Targeting Laboratory", at the Department of Life Sciences, University of Modena and Reggio Emilia, under the supervision of Prof. Eliana Leo. Part of this project was carried out in “FarmaTec Laboratory”, at the School of Pharmacy, Federal University of Goiás in Brazil, under the supervision of Prof. Eliana Martin Lima.

Excellent support and supervision were also offered by other members of the research groups: Dr. Valentina Iannuccelli, Prof. Gilberto Coppi and Dr. Eleonora Maretti from the University of Modena and Reggio Emilia; Dr. Thais Leite Nascimento and Edilson Ribeiro de Oliveira Junior from Federal University of Goiás.

This PhD thesis would not be so completed without the help and support of:

- Dr. Cecilia Rustichelli (Department of Life Sciences, University of Modena and Reggio Emilia);
- Dr. Maria Antonietta Croce, Dr. Monica Montanari (Cell-Lab Paola Buffa, Department of Life Sciences, University of Modena and Reggio Emilia);
- Dr. Maria Cecilia Rossi, Dr. Mauro Zapparoli and Dr. Massimo Tonelli (Inter-Departmental Great Instruments Centre, University of Modena and Reggio Emilia);
- Dr. Fiorella Meneghetti (Department of Pharmaceutical Sciences, University of Milan), Dr. Carlo Castellano (Chemistry Department, University of Milan), Angela Capocefalo (Physic Department, Sapienza University) and Dr. Fabio Domenici (Department of chemical sciences and technologies, Rome Tor Vergata University);
- Prof. Alessandro Dalpiaz, Dr. Marco Fogagnolo (Department of Life Sciences and Biotechnology, University of Ferrara), Dr. Barbara Pavan (Department of Biomedical and Specialist Surgical Sciences, University of Ferrara) and Luca Ferraro (Department of Chemical and Pharmaceutical Sciences, University of Ferrara);
- Prof. Elena Vismara and Chiara Bongio (Department of Chemistry, Materials and Chemical Engineering “G. Natta”).

I would like to thank all the above-mentioned people for their precious contribution.

REFERENCES

[1] A.M. Hillery, A.W. Lloyd, J. Swarbrick, Drug Delivery and Targeting for Pharmacists and Pharmaceutical Scientists, 1st ed., Taylor & Francis Group, 2001.

[2] M. Geszke-Moritz, M. Moritz, Solid lipid nanoparticles as attractive drug vehicles : Composition , properties and therapeutic strategies, Mater. Sci. Eng. C. 68 (2016) 982–994. doi:10.1016/j.msec.2016.05.119.

[3] T. Haponiuk, S. Thomas, S. Gopi, J. Jacob, Biopolymer based nanomaterials in drug delivery systems : A review, Mater. Today Chem. 9 (2018) 43–55. doi:10.1016/j.mtchem.2018.05.002.

[4] S. Doktorovova, E.B. Souto, A.M. Silva, Nanotoxicology applied to solid lipid nanoparticles and nanostructured lipid carriers - A systematic review of in vitro data, Eur. J. Pharm. Biopharm. 87 (2014) 1–18. doi:10.1016/j.ejpb.2014.02.005.

[5] G. Crini, Review: A history of cyclodextrins, Chem. Rev. 114 (2014) 10940–10975. doi:10.1021/cr500081p.

[6] S.S. Jambhekar, P. Breen, Cyclodextrins in pharmaceutical formulations I: Structure and physicochemical properties, formation of complexes, and types of complex, Drug Discov. Today. 21 (2016) 356–362. doi:10.1016/j.drudis.2015.11.017.

[7] I. Mourtzinos, N. Kalogeropoulos, S.E. Papadakis, K. Konstantinou, V.T. Karathanos, Encapsulation of nutraceutical monoterpenes in β-cyclodextrin and modified starch, J. Food Sci. 73 (2008) 89–94. doi:10.1111/j.1750-3841.2007.00609.x.

[8] L. Szente, J. Szejtli, Cyclodextrins as food ingredients, Trends Food Sci. Technol. 15 (2004) 137–142. doi:10.1016/J.TIFS.2003.09.019.

[9] M. Singh, R. Sharma, U.C. Banerjee, Biotechnological applications of cyclodextrins, Biotechnol. Adv. 20 (2002) 341–359. doi:10.1016/S0734-9750(02)00020-4.

[10] E. Medicines Agency, Committee for Human Medicinal Products (CHMP), 2017. www.ema.europa.eu/contact.

[11] M. Ghadiri, P.M. Young, D. Traini, Strategies to enhance drug absorption via nasal and pulmonary routes, Pharmaceutics. 11 (2019) 1–20. doi:10.3390/pharmaceutics11030113.

[12] N.G.M. Schipper, J. Verhoef, S.G. Romeijn, F.W.H.M. Merkus, Absorption enhancers in nasal insulin delivery and their influence on nasal ciliary functioning, J. Control. Release. 21 (1992) 173–185. doi:10.1016/0168-3659(92)90019-N.

[13] L.B. Salem, C. Bosquillon, L.A. Dailey, L. Delattre, G.P. Martin, B. Evrard, B. Forbes, Sparing methylation of β-cyclodextrin mitigates cytotoxicity and permeability

induction in respiratory epithelial cell layers in vitro, J. Control. Release. 136 (2009) 110–116. doi:10.1016/j.jconrel.2009.01.019.

[14] L. Matilainen, T. Toropainen, H. Vihola, J. Hirvonen, T. Järvinen, P. Jarho, K. Järvinen, In vitro toxicity and permeation of cyclodextrins in Calu-3 cells, J. Control. Release. 126 (2008) 10–16. doi:10.1016/j.jconrel.2007.11.003.

[15] A. Wretlind, Development of fat emulsions, JPEN. J. Parenter. Enteral Nutr. 5 (1981) 230–5. doi:10.1177/0148607181005003230.

[16] A.D. Bangham, R.W. Horne, Negative staining of phospholipids and their structural modification by surface-active agents as observed in the electron microscope, J. Mol. Biol. 8 (1964) IN2–IN10. doi:10.1016/S0022-2836(64)80115-7.

[17] A. Laouini, C. Jaafar-Maalej, I. Limayem-Blouza, S. Sfar, C. Charcosset, H. Fessi, Preparation, Characterization and Applications of Liposomes: State of the Art, J. Colloid Sci. Biotechnol. 1 (2012) 147–168. doi:10.1166/jcsb.2012.1020.

[18] U. Bulbake, S. Doppalapudi, N. Kommineni, W. Khan, Liposomal formulations in clinical use: An updated review, Pharmaceutics. 9 (2017) 1–33. doi:10.3390/pharmaceutics9020012.

[19] Y. Rahimpour, H. Hamishehkar, Liposomes in cosmeceutics, Expert Opin. Drug Deliv. 9 (2012) 443–455. doi:10.1517/17425247.2012.666968.

[20] C. Schwarz, W. Mehnert, J.S. Lucks, R.H. Müller, Solid lipid nanoparticles (SLN) for controlled drug delivery. I. Production, characterization and sterilization, J. Control. Release. 30 (1994) 83–96. doi:10.1016/0168-3659(94)90047-7.

[21] S. Weber, A. Zimmer, J. Pardeike, Solid Lipid Nanoparticles (SLN) and Nanostructured Lipid Carriers (NLC) for pulmonary application: A review of the state of the art, Eur. J. Pharm. Biopharm. 86 (2014) 7–22. doi:10.1016/J.EJPB.2013.08.013.

[22] R.H. Müller, M. Radtke, S.A. Wissing, Solid lipid nanoparticles (SLN) and nanostructured lipid carriers (NLC) in cosmetic and dermatological preparations, in: Adv. Drug Deliv. Rev., 2002. doi:10.1016/S0169-409X(02)00118-7.

[23] S. Chaudhary, T. Garg, R.S.R. Murthy, G. Rath, A.K. Goyal, Recent approaches of lipid-based delivery system for lymphatic targeting via oral route., J. Drug Target. 22 (2014) 871–82. doi:10.3109/1061186X.2014.950664.

[24] S.A. Wissing, O. Kayser, R.H. Müller, Solid lipid nanoparticles for parenteral drug delivery., Adv. Drug Deliv. Rev. 56 (2004) 1257–72. doi:10.1016/j.addr.2003.12.002.

[25] I. Singh, R. Swami, W. Khan, R. Sistla, Lymphatic system: a prospective area for advanced targeting of particulate drug carriers., Expert Opin. Drug Deliv. 11 (2014)

211–29. doi:10.1517/17425247.2014.866088.

[26] H.J. Cho, J.W. Park, I.S. Yoon, D.D. Kim, Surface-modified solid lipid nanoparticles for oral delivery of docetaxel: Enhanced intestinal absorption and lymphatic uptake, Int. J. Nanomedicine. 9 (2014) 495–504. doi:10.2147/IJN.S56648.

[27] M.R. Aji Alex, A.J. Chacko, S. Jose, E.B. Souto, Lopinavir loaded solid lipid nanoparticles (SLN) for intestinal lymphatic targeting, Eur. J. Pharm. Sci. 42 (2011) 11–18. doi:10.1016/j.ejps.2010.10.002.

[28] S. Rao, A. Tan, N. Thomas, C.A. Prestidge, Perspective and potential of oral lipid-based delivery to optimize pharmacological therapies against cardiovascular diseases., J. Control. Release. 193 (2014) 174–87. doi:10.1016/j.jconrel.2014.05.013.

[29] K. Pantel, R.H. Brakenhoff, Dissecting the metastatic cascade., Nat. Rev. Cancer. 4 (2004) 448–56. doi:10.1038/nrc1370.

[30] A. Ali Khan, J. Mudassir, N. Mohtar, Y. Darwis, Advanced drug delivery to the lymphatic system: lipid-based nanoformulations., Int. J. Nanomedicine. 8 (2013) 2733–44. doi:10.2147/IJN.S41521.

[31] N.L. Trevaskis, W.N. Charman, C.J.H. Porter, Lipid-based delivery systems and intestinal lymphatic drug transport: A mechanistic update, Adv. Drug Deliv. Rev. 60 (2008) 702–716. doi:10.1016/j.addr.2007.09.007.

[32] C.J.H. Porter, N.L. Trevaskis, W.N. Charman, Lipids and lipid-based formulations: optimizing the oral delivery of lipophilic drugs., Nat. Rev. Drug Discov. 6 (2007) 231–48. doi:10.1038/nrd2197.

[33] W.N.A. Charman, V.J. Stella, Estimating the maximal potential for intestinal lymphatic transport of lipophilic drug molecules, Int. J. Pharm. 34 (1986) 175–178. doi:10.1016/0378-5173(86)90027-X.

[34] M.K. Shah, P. Madan, S. Lin, Preparation, in vitro evaluation and statistical optimization of carvedilol-loaded solid lipid nanoparticles for lymphatic absorption via oral administration, Pharm. Dev. Technol. 19 (2014) 475–485. doi:doi:10.3109/10837450.2013.795169.

[35] J.D. Clogston, A.K. Patri, Zeta Potential Measurement, in: 2011: pp. 63–70. doi:10.1007/978-1-60327-198-1_6.

[36] H. Arami, A. Khandhar, D. Liggitt, K.M. Krishnan, In vivo delivery, pharmacokinetics, biodistribution and toxicity of iron oxide nanoparticles., Chem. Soc. Rev. 44 (2015) 8576–607. doi:10.1039/c5cs00541h.

[37] V.I. Shubayev, T.R. Pisanic, S. Jin, Magnetic nanoparticles for theragnostics., Adv.

Drug Deliv. Rev. 61 (2009) 467–77. doi:10.1016/j.addr.2009.03.007.

[38] A.K. Gupta, M. Gupta, Synthesis and surface engineering of iron oxide nanoparticles for biomedical applications., Biomaterials. 26 (2005) 3995–4021. doi:10.1016/j.biomaterials.2004.10.012.

[39] T. Neuberger, B. Schöpf, H. Hofmann, M. Hofmann, B. von Rechenberg, Superparamagnetic nanoparticles for biomedical applications: Possibilities and limitations of a new drug delivery system, J. Magn. Magn. Mater. 293 (2005) 483–496. doi:10.1016/j.jmmm.2005.01.064.

[40] S. Mornet, S. Vasseur, F. Grasset, E. Duguet, Magnetic nanoparticle design for medical diagnosis and therapy, J. Mater. Chem. 14 (2004) 2161. doi:10.1039/b402025a.

[41] E. Vismara, A. Valerio, A. Coletti, G. Torri, S. Bertini, G. Eisele, R. Gornati, G. Bernardini, Non-covalent synthesis of metal oxide nanoparticle-heparin hybrid systems: a new approach to bioactive nanoparticles., Int. J. Mol. Sci. 14 (2013) 13463–13481. doi:10.3390/ijms140713463.

[42] G. Bendas, L. Borsig, Cancer cell adhesion and metastasis: selectins, integrins, and the inhibitory potential of heparins., Int. J. Cell Biol. 2012 (2012) 676731. doi:10.1155/2012/676731.

[43] S.M. Smorenburg, R.J. Hettiarachchi, R. Vink, H.R. Büller, The effects of unfractionated heparin on survival in patients with malignancy--a systematic review., Thromb. Haemost. 82 (1999) 1600–4. http://www.ncbi.nlm.nih.gov/pubmed/10613641 (accessed February 1, 2017).

[44] B. Casu, A. Naggi, G. Torri, Re-visiting the structure of heparin, Carbohydr. Res. 403 (2015) 60–68. doi:10.1016/j.carres.2014.06.023.

[45] M. Licciardi, C. Scialabba, C. Fiorica, G. Cavallaro, G. Cassata, G. Giammona, Polymeric Nanocarriers for Magnetic Targeted Drug Delivery: Preparation, Characterization, and in Vitro and in Vivo Evaluation, Mol. Pharm. 10 (2013) 4397–4407. doi:10.1021/mp300718b.

[46] Y. Jiao, N. Ubrich, V. Hoffart, M. Marchand-Arvier, C. Vigneron, M. Hoffman, P. Maincent, Anticoagulant activity of heparin following oral administration of heparin-loaded microparticles in rabbits., J. Pharm. Sci. 91 (2002) 760–8. http://www.ncbi.nlm.nih.gov/pubmed/11920761 (accessed February 6, 2017).

[47] S. Mahajan, V. Koul, V. Choudhary, G. Shishodia, A.C. Bharti, Preparation and in vitro evaluation of folate-receptor-targeted SPION-polymer micelle hybrids for MRI contrast enhancement in cancer imaging., Nanotechnology. 24 (2013) 015603.

doi:10.1088/0957-4484/24/1/015603.

[48] K.A. Min, F. Yu, V.C. Yang, X. Zhang, G.R. Rosania, Transcellular Transport of Heparin-coated Magnetic Iron Oxide Nanoparticles (Hep-MION) Under the Influence of an Applied Magnetic Field., Pharmaceutics. 2 (2010) 119–135. doi:10.3390/pharmaceutics2020119.

[49] S.M. Caliph, W.N. Charman, C.J. Porter, Effect of short-, medium-, and long-chain fatty acid-based vehicles on the absolute oral bioavailability and intestinal lymphatic transport of halofantrine and assessment of mass balance in lymph-cannulated and non-cannulated rats., J. Pharm. Sci. 89 (2000) 1073–84. http://www.ncbi.nlm.nih.gov/pubmed/10906731 (accessed February 8, 2017).

[50] K. Turcheniuk, A. V. Tarasevych, V.P. Kukhar, R. Boukherroub, S. Szunerits, Recent advances in surface chemistry strategies for the fabrication of functional iron oxide based magnetic nanoparticles, Nanoscale. 5 (2013) 10729. doi:10.1039/c3nr04131j.

[51] P. Gershkovich, A. Hoffman, Uptake of lipophilic drugs by plasma derived isolated chylomicrons: linear correlation with intestinal lymphatic bioavailability., Eur. J. Pharm. Sci. 26 (2005) 394–404. doi:10.1016/j.ejps.2005.07.011.

[52] C. Olbrich, R.H. Müller, Enzymatic degradation of SLN-effect of surfactant and surfactant mixtures., Int. J. Pharm. 180 (1999) 31–9. http://www.ncbi.nlm.nih.gov/pubmed/10089289 (accessed February 2, 2017).

[53] S.L. Shimpi, K.R. Mahadik, A.R. Paradkar, Study on mechanism for amorphous drug stabilization using gelucire 50/13., Chem. Pharm. Bull. (Tokyo). 57 (2009) 937–42. http://www.ncbi.nlm.nih.gov/pubmed/19721253 (accessed January 4, 2017).

[54] A.A. Date, N. Vador, A. Jagtap, M.S. Nagarsenker, Lipid nanocarriers (GeluPearl) containing amphiphilic lipid Gelucire 50/13 as a novel stabilizer: fabrication, characterization and evaluation for oral drug delivery., Nanotechnology. 22 (2011) 275102. doi:10.1088/0957-4484/22/27/275102.

[55] O. Dubray, V. Jannin, F. Demarne, Y. Pellequer, A. Lamprecht, A. Béduneau, In-vitro investigation regarding the effects of Gelucire 44/14 and Labrasol ALF on the secretory intestinal transport of P-gp substrates, Int. J. Pharm. 515 (2016) 293–299. doi:10.1016/j.ijpharm.2016.10.012.

[56] K. Sachs-Barrable, A. Thamboo, S.D. Lee, K.M. Wasan, Lipid excipients Peceol and Gelucire 44/14 decrease P-glycoprotein mediated efflux of rhodamine 123 partially due to modifying P-glycoprotein protein expression within Caco-2 cells., J. Pharm. Pharm. Sci. 10 (2007) 319–31. http://www.ncbi.nlm.nih.gov/pubmed/17727795 (accessed

February 1, 2017).

[57] N.L. Trevaskis, L.M. Kaminskas, C.J.H. Porter, From sewer to saviour - targeting the lymphatic system to promote drug exposure and activity., Nat. Rev. Drug Discov. 14 (2015) 781–803. doi:10.1038/nrd4608.

[58] B. Chatterjee, S. Hamed Almurisi, A. Ahmed Mahdi Dukhan, U.K. Mandal, P. Sengupta, Controversies with self-emulsifying drug delivery system from pharmacokinetic point of view., Drug Deliv. 23 (2016) 3639–3652. doi:10.1080/10717544.2016.1214990.

[59] V. Valdiglesias, N. Fernández-Bertólez, G. Kiliç, C. Costa, S. Costa, S. Fraga, M.J. Bessa, E. Pásaro, J.P. Teixeira, B. Laffon, Are iron oxide nanoparticles safe? Current knowledge and future perspectives, J. Trace Elem. Med. Biol. 38 (2016) 53–63. doi:10.1016/j.jtemb.2016.03.017.

[60] S.J.H. Soenen, M. De Cuyper, Assessing cytotoxicity of (iron oxide-based) nanoparticles: An overview of different methods exemplified with cationic magnetoliposomes, Contrast Media Mol. Imaging. 4 (2009) 207–219. doi:10.1002/cmmi.282.

[61] T.R. Pisanic, J.D. Blackwell, V.I. Shubayev, R.R. Fiñones, S. Jin, Nanotoxicity of iron oxide nanoparticle internalization in growing neurons, Biomaterials. 28 (2007) 2572–2581. doi:10.1016/j.biomaterials.2007.01.043.

[62] World Health Organization, Global Tuberculosis Report 2018, Geneva, 2018.

[63] S. Claus, C. Weiler, J. Schiewe, W. Friess, How can we bring high drug doses to the lung?, Eur. J. Pharm. Biopharm. 86 (2014) 1–6. doi:10.1016/j.ejpb.2013.11.005.

[64] L.-O. Larsson, New approaches in drug treatment for tuberculosis: Inhalation using liposomes only a future vision or soon in clinical practice?, Int. J. Mycobacteriology. 5 (2016) S29–S30. doi:10.1016/j.ijmyco.2016.09.032.

[65] V. Iannuccelli, E. Maretti, Inhaled Micro-or Nanoparticles: Which are the Best for Intramacrophagic Antiinfectious Therapies? Intramacrophagic Anti-infectious therapies, J Infect Dis Diagn. (2015). doi:10.4172/2576-389X.1000e102.

[66] P.J. Brennan, D.B. Young, Isoniazid, Tuberculosis. 88 (2008) 112–116. doi:10.1016/S1472-9792(08)70011-8.

[67] P.J. Brennan, D.B. Young, Rifampicin, Tuberculosis. 88 (2008) 151–154. doi:10.1016/S1472-9792(08)70024-6.

[68] C. Grabielle-Madelmont, S. Lesieur, M. Ollivon, Characterization of loaded liposomes by size exclusion chromatography, J. Biochem. Biophys. Methods. 56 (2003) 189–217.

doi:10.1016/S0165-022X(03)00059-9.

[69] J. Costa-Gouveia, E. Pancani, S. Jouny, A. Machelart, V. Delorme, G. Salzano, R. Iantomasi, C. Piveteau, C.J. Queval, O.-R. Song, M. Flipo, B. Deprez, J.-P. Saint-André, J. Hureaux, L. Majlessi, N. Willand, A. Baulard, P. Brodin, R. Gref, Combination therapy for tuberculosis treatment: pulmonary administration of ethionamide and booster co-loaded nanoparticles, Sci. Rep. 7 (2017) 5390. doi:10.1038/s41598-017-05453-3.

[70] L. Fanzani, F. Porta, F. Meneghetti, S. Villa, A. Gelain, A.P. Lucarelli, E. Parisini, Mycobacterium tuberculosis Low Molecular Weight Phosphatases (MPtpA and MPtpB): From Biological Insight to Inhibitors., Curr. Med. Chem. 22 (2015) 3110–32. doi:10.2174/0929867322666150812150036.

[71] F. Meneghetti, S. Villa, A. Gelain, D. Barlocco, L.R. Chiarelli, M.R. Pasca, L. Costantino, Iron Acquisition Pathways as Targets for Antitubercular Drugs., Curr. Med. Chem. 23 (2016) 4009–4026. doi:10.2174/0929867323666160607223747.

[72] V. Singh, V. Mizrahi, Identification and validation of novel drug targets in Mycobacterium tuberculosis, Drug Discov. Today. 22 (2017) 503–509. doi:10.1016/J.DRUDIS.2016.09.010.

[73] L. D'Ambrosio, R. Centis, S. Tiberi, M. Tadolini, M. Dalcolmo, A. Rendon, S. Esposito, G.B. Migliori, Delamanid and bedaquiline to treat multidrug-resistant and extensively drug-resistant tuberculosis in children: a systematic review., J. Thorac. Dis. 9 (2017) 2093–2101. doi:10.21037/jtd.2017.06.16.

[74] N. Kučerka, M.-P. Nieh, J. Pencer, T. Harroun, J. Katsaras, The study of liposomes, lamellae and membranes using neutrons and X-rays, Curr. Opin. Colloid Interface Sci. 12 (2007) 17–22. doi:10.1016/J.COCIS.2006.11.006.

[75] N. Kučerka, J.F. Nagle, J.N. Sachs, S.E. Feller, J. Pencer, A. Jackson, J. Katsaras, Lipid Bilayer Structure Determined by the Simultaneous Analysis of Neutron and X-Ray Scattering Data, Biophys. J. 95 (2008) 2356–2367. doi:10.1529/biophysj.108.132662.

[76] E. Di Cola, I. Grillo, S. Ristori, Small Angle X-ray and Neutron Scattering: Powerful Tools for Studying the Structure of Drug-Loaded Liposomes., Pharmaceutics. 8 (2016) 10. doi:10.3390/pharmaceutics8020010.

[77] Institut Laue-Langevin, Small-angle neutron scattering diffractometer, Grenoble, Fr. (n.d.).

[78] L.A. Feigin, D.I. Svergun, Structure Analysis by Small-Angle X-Ray and Neutron

Scattering, Springer US, Boston, MA, 1987. doi:10.1007/978-1-4757-6624-0.

[79] F. Sacchetti, D. D'Arca, F. Genovese, S. Pacifico, E. Maretti, M. Hanuskova, V. Iannuccelli, M.P. Costi, E. Leo, Conveying a newly designed hydrophilic anti-human thymidylate synthase peptide to *cisplatin* resistant cancer cells: are pH-sensitive liposomes more effective than conventional ones?, Drug Dev. Ind. Pharm. 43 (2017) 465–473. doi:10.1080/03639045.2016.1262870.

[80] M. Tilinca, G. Hancu, E. Mircia, D. Iriminescu, A. Rusu, R.A. Vlad, E. Barabás, Simultaneous determination of isoniazid and rifampicin by UV spectrophotometry, Farmacia. 65 (2017) 219–224.

[81] A. Gürsoy, E. Kut, S. Özkirimli, Co-encapsulation of isoniazid and rifampicin in liposomes and characterization of liposomes by derivative spectroscopy, Int. J. Pharm. 271 (2004) 115–123. doi:10.1016/j.ijpharm.2003.10.033.

[82] M.R.C. Marques, R. Loebenberg, M. Almukainzi, Simulated Biological Fluids with Possible Application in Dissolution Testing, Dissolution Technol. 18 (2011) 15–28. doi:10.14227/DT180311P15.

[83] V. Ramakrishnan, A Treatment of Instrumental Smearing Effects in Circularly Symmetric Small-Angle Scattering, J. Appl. Cryst. 18 (1985) 42–46. doi:10.1107/S0021889885009748.

[84] B. Cabane, Small Angle Scattering Methods, in: M.D. R. Zana (Ed.), Surfactant Solut. New Methods Investig., Surfactant, 1987.

[85] F. Domenici, C. Castellano, A. Congiu, G. Pompeo, R. Felici, Ordering and lyotropic behavior of a silicon-supported cationic and neutral lipid system studied by neutron reflectivity, Appl. Phys. Lett. 92 (2008) 193901. doi:10.1063/1.2917807.

[86] S. Bhattacharjee, DLS and zeta potential - What they are and what they are not?, J. Control. Release. 235 (2016) 337–351. doi:10.1016/j.jconrel.2016.06.017.

[87] J. Gallová, D. Uhríková, A. Islamov, A. Kuklin, P. Balgavý, Effect of cholesterol on the bilayer thickness in unilamellar extruded DLPC and DOPC liposomes: SANS contrast variation study., Gen. Physiol. Biophys. 23 (2004) 113–28.

[88] S. Labana, R. Pandey, S. Sharma, G.K. Khuller, Chemotherapeutic activity against murine tuberculosis of once weekly administered drugs (isoniazid and rifampicin) encapsulated in liposomes., Int. J. Antimicrob. Agents. 20 (2002) 301–4. doi:10.1016/S0924-8579(02)00175-9.

[89] N. Changsan, H.-K. Chan, F. Separovic, T. Srichana, Physicochemical characterization and stability of rifampicin liposome dry powder formulations for inhalation., J. Pharm.

Sci. 98 (2009) 628–39. doi:10.1002/jps.21441.

[90] C. Rodrigues, P. Gameiro, M. Prieto, B. De Castro, Interaction of rifampicin and isoniazid with large unilamellar liposomes: Spectroscopic location studies, Biochim. Biophys. Acta - Gen. Subj. 1620 (2003) 151–159. doi:10.1016/S0304-4165(02)00528-7.

[91] A.V. Marques, P. Marengo Trindade, S. Marques, T. Brum, E. Harte, M.O. Rodrigues, M.G.M. D'Oca, P.A. da Silva, A.R. Pohlmann, I.D. Alves, V.R. de Lima, Isoniazid interaction with phosphatidylcholine-based membranes, J. Mol. Struct. 1051 (2013) 237–243. doi:10.1016/J.MOLSTRUC.2013.08.029.

[92] F. Domenici, F. Dell'Unto, D. Triggiani, C. Olmati, C. Castellano, F. Bordi, A. Tiezzi, A. Congiu, Vertical ordering sensitivity of solid supported DPPC membrane to alamethicin and the related loss of cell viability., Biochim. Biophys. Acta. 1850 (2015) 759–68. doi:10.1016/j.bbagen.2015.01.006.

[93] J. Li, X. Wang, T. Zhang, C. Wang, Z. Huang, X. Luo, Y. Deng, A review on phospholipids and their main applications in drug delivery systems, Asian J. Pharm. Sci. 10 (2015) 81–98. doi:10.1016/j.ajps.2014.09.004.

[94] P. Deol, G.K. Khuller, K. Joshi, Therapeutic efficacies of isoniazid and rifampin encapsulated in lung-specific stealth liposomes against Mycobacterium tuberculosis infection induced in mice., Antimicrob. Agents Chemother. 41 (1997) 1211–4.

[95] J.D. Johnson, W.L. Hand, J.B. Francis, N. King-Thompson, R.W. Corwin, Antibiotic uptake by alveolar macrophages, J. Lab. Clin. Med. 95 (1980) 429–439. doi:10.5555/URI:PII:0022214380904643.

[96] K. Hirota, T. Hasegawa, T. Nakajima, H. Inagawa, C. Kohchi, G.-I. Soma, K. Makino, H. Terada, Delivery of rifampicin–PLGA microspheres into alveolar macrophages is promising for treatment of tuberculosis, J. Control. Release. 142 (2010) 339–346. doi:10.1016/j.jconrel.2009.11.020.

[97] W.-H. Lee, C.-Y. Loo, D. Traini, P.M. Young, Nano- and micro-based inhaled drug delivery systems for targeting alveolar macrophages., Expert Opin. Drug Deliv. 12 (2015) 1009–26. doi:10.1517/17425247.2015.1039509.

[98] A.J. Hickey, H.M. Mansour, Inhalation Aerosols: Physical and Biological Basis for Therapy, 2nd edition., Respir. Care. 52 (2007) 1238–1239.

[99] E. Maretti, L. Costantino, F. Buttini, C. Rustichelli, E. Leo, E. Truzzi, V. Iannuccelli, Newly synthesized surfactants for surface mannosylation of respirable SLN assemblies to target macrophages in tuberculosis therapy, Drug Deliv. Transl. Res. 9 (2019) 298–

310. doi:10.1007/s13346-018-00607-w.

[100] D.-D. Pham, E. Fattal, N. Tsapis, Pulmonary drug delivery systems for tuberculosis treatment, Int. J. Pharm. 478 (2015) 517–529. doi:10.1016/j.ijpharm.2014.12.009.

[101] N.P. Chaturvedi, H. Solanki, Pulmonary Drug Delivery System: Review, Int. J. Appl. Pharm. 5 (2013) 7–10.

[102] M. Pinheiro, R. Ribeiro, A. Vieira, F. Andrade, S. Reis, Design of a nanostructured lipid carrier intended to improve the treatment of tuberculosis, Drug Des. Devel. Ther. Volume 10 (2016) 2467–2475. doi:10.2147/DDDT.S104395.

[103] S.K. Katiyar, S. Bihari, S. Prakash, Low-dose inhaled versus standard dose oral form of anti-tubercular drugs: concentrations in bronchial epithelial lining fluid, alveolar macrophage and serum., J. Postgrad. Med. 54 (2008) 245–6. doi:10.4103/0022-3859.41823.

[104] M. Paranjpe, C.C. Müller-Goymann, Nanoparticle-mediated pulmonary drug delivery: A review, Int. J. Mol. Sci. 15 (2014) 5852–5873. doi:10.3390/ijms15045852.

[105] E. Rostami, S. Kashanian, A.H. Azandaryani, H. Faramarzi, J.E.N. Dolatabadi, K. Omidfar, Drug targeting using solid lipid nanoparticles, Chem. Phys. Lipids. 181 (2014) 56–61. doi:10.1016/j.chemphyslip.2014.03.006.

[106] R. Sharma, P. Muttil, A.B. Yadav, S.K. Rath, V.K. Bajpai, U. Mani, A. Misra, Uptake of inhalable microparticles affects defence responses of macrophages infected with Mycobacterium tuberculosis H37Ra., J. Antimicrob. Chemother. 59 (2007) 499–506. doi:10.1093/jac/dkl533.

[107] V. Iannuccelli, E. Maretti, Inhaled Micro- or Nanoparticles: Which are the Best for Intramacrophagic Antiinfectious Therapies?, J. Infect. Dis. Diagnosis. 01 (2016). doi:10.4172/2576-389X.1000e102.

[108] M. Takenaga, Y. Ohta, Y. Tokura, A. Hamaguchi, R. Igarashi, A. Disratthakit, N. Doi, Lipid microsphere formulation containing rifampicin targets alveolar macrophages., Drug Deliv. 15 (2008) 169–75. doi:10.1080/10717540801952530.

[109] E. Maretti, T. Rossi, M. Bondi, M.A. Croce, M. Hanuskova, E. Leo, F. Sacchetti, V. Iannuccelli, Inhaled Solid Lipid Microparticles to target alveolar macrophages for tuberculosis., Int. J. Pharm. 462 (2014) 74–82. doi:10.1016/j.ijpharm.2013.12.034.

[110] N. Nimje, A. Agarwal, G.K. Saraogi, N. Lariya, G. Rai, H. Agrawal, G.P. Agrawal, Mannosylated nanoparticulate carriers of rifabutin for alveolar targeting., J. Drug Target. 17 (2009) 777–87. doi:10.3109/10611860903115308.

[111] S.M. Moghimi, L. Parhamifar, D. Ahmadvand, P.P. Wibroe, T.L. Andresen, Z.S.

Farhangrazi, A.C. Hunter, Particulate systems for targeting of macrophages: Basic and therapeutic concepts, J. Innate Immun. 4 (2012) 509–528. doi:10.1159/000339153.

[112] E. Maretti, C. Rustichelli, M.L. Gualtieri, L. Costantino, C. Siligardi, P. Miselli, F. Buttini, M. Montecchi, E. Leo, E. Truzzi, V. Iannuccelli, The Impact of Lipid Corona on Rifampicin Intramacrophagic Transport Using Inhaled Solid Lipid Nanoparticles Surface-Decorated with a Mannosylated Surfactant, Pharmaceutics. 11 (2019) 508. doi:10.3390/pharmaceutics11100508.

[113] R.K. Verma, J. Kaur, K. Kumar, A.B. Yadav, A. Misra, Intracellular time course, pharmacokinetics, and biodistribution of isoniazid and rifabutin following pulmonary delivery of inhalable microparticles to mice, Antimicrob. Agents Chemother. 52 (2008) 3195–3201. doi:10.1128/AAC.00153-08.

[114] M. Geiser, Update on macrophage clearance of inhaled micro- and nanoparticles, J. Aerosol Med. Pulm. Drug Deliv. 23 (2010) 207–217. doi:10.1089/jamp.2009.0797.

[115] A.J. Thorley, P. Ruenraroengsak, T.E. Potter, T.D. Tetley, Critical determinants of uptake and translocation of nanoparticles by the human pulmonary alveolar Epithelium, ACS Nano. 8 (2014) 11778–11789. doi:10.1021/nn505399e.

[116] M.R. Miller, J.B. Raftis, J.P. Langrish, S.G. McLean, P. Samutrtai, S.P. Connell, S. Wilson, A.T. Vesey, P.H.B. Fokkens, A.J.F. Boere, P. Krystek, C.J. Campbell, P.W.F. Hadoke, K. Donaldson, F.R. Cassee, D.E. Newby, R. Duffin, N.L. Mills, Inhaled Nanoparticles Accumulate at Sites of Vascular Disease, ACS Nano. 11 (2017) 4542–4552. doi:10.1021/acsnano.6b08551.

[117] I.M. El-Sherbiny, N.M. El-Baz, M.H. Yacoub, Inhaled nano- and microparticles for drug delivery, Glob. Cardiol. Sci. Pract. 2015 (2015) 2. doi:10.5339/gcsp.2015.2.

[118] R.R. Mercer, J.F. Scabilloni, L. Wang, L.A. Battelli, J.M. Antonini, J.R. Roberts, Y. Qian, J.D. Sisler, V. Castranova, D.W. Porter, A.F. Hubbs, The Fate of Inhaled Nanoparticles: Detection and Measurement by Enhanced Dark-field Microscopy, Toxicol. Pathol. 46 (2018) 28–46. doi:10.1177/0192623317732321.

[119] L. Aragao-Santiago, H. Hillaireau, N. Grabowski, S. Mura, T.L. Nascimento, S. Dufort, J.-L. Coll, N. Tsapis, E. Fattal, Compared *in vivo* toxicity in mice of lung delivered biodegradable and non-biodegradable nanoparticles, Nanotoxicology. 10 (2016) 292–302. doi:10.3109/17435390.2015.1054908.

[120] K. Ganguly, D. Ettehadieh, S. Upadhyay, S. Takenaka, T. Adler, E. Karg, F. Krombach, W.G. Kreyling, H. Schulz, O. Schmid, T. Stoeger, Early pulmonary response is critical for extra-pulmonary carbon nanoparticle mediated effects:

comparison of inhalation versus intra-arterial infusion exposures in mice, Part. Fibre Toxicol. 14 (2017) 19. doi:10.1186/s12989-017-0200-x.

[121] Y.-B. Wang, A.B. Watts, J.I. Peters, R.O. Williams, The impact of pulmonary diseases on the fate of inhaled medicines—A review, Int. J. Pharm. 461 (2014) 112–128. doi:10.1016/j.ijpharm.2013.11.042.

[122] S. Hakkimane, V.P. Shenoy, S. Gaonkar, I. Bairy, B.R. Guru, Antimycobacterial susceptibility evaluation of rifampicin and isoniazid benz-hydrazone in biodegradable polymeric nanoparticles against Mycobacterium tuberculosis H37Rv strain, Int. J. Nanomedicine. 13 (2018) 4303–4318. doi:10.2147/IJN.S163925.

[123] C. Zhang, L. Long, C. Shi, Mitochondria-Targeting IR-780 Dye and Its Derivatives: Synthesis, Mechanisms of Action, and Theranostic Applications, Adv. Ther. 1 (2018) 1800069. doi:10.1002/adtp.201800069.

[124] O.S. Usmani, M.F. Biddiscombe, P.J. Barnes, Regional Lung Deposition and Bronchodilator Response as a Function of β_2-Agonist Particle Size, Am. J. Respir. Crit. Care Med. 172 (2005) 1497–1504. doi:10.1164/rccm.200410-1414OC.

[125] J.A. Champion, S. Mitragotri, Role of target geometry in phagocytosis, Proc. Natl. Acad. Sci. 103 (2006) 4930–4934. doi:10.1073/pnas.0600997103.

[126] A. Remmerie, C.L. Scott, Macrophages and lipid metabolism, Cell. Immunol. 330 (2018) 27–42. doi:10.1016/j.cellimm.2018.01.020.

[127] C. Odaka, T. Mizuochi, Role of macrophage lysosomal enzymes in the degradation of nucleosomes of apoptotic cells., J. Immunol. 163 (1999) 5346–52.

[128] E. Goldstein, Hydrolytic Enzymes of Alveolar Macrophages, Rev. Infect. Dis. 5 (n.d.) 1078–1092. doi:10.2307/4453228.

[129] C. Olbrich, O. Kayser, R.H. Müller, Enzymatic degradation of Dynasan 114 SLN - Effect of surfactants and particle size, J. Nanoparticle Res. 4 (2002) 121–129. doi:10.1023/A:1020159331420.

[130] W. Vogelhuber, E. Magni, A. Gazzaniga, A. Göpferich, Monolithic glyceryl trimyristate matrices for parenteral drug release applications., Eur. J. Pharm. Biopharm. 55 (2003) 133–8. doi:10.1016/S0939-6411(02)00137-6.

[131] C.G. Alves, R. Lima-Sousa, D. de Melo-Diogo, R.O. Louro, I.J. Correia, IR780 based nanomaterials for cancer imaging and photothermal, photodynamic and combinatorial therapies, Int. J. Pharm. 542 (2018) 164–175. doi:10.1016/j.ijpharm.2018.03.020.

[132] S.K. Rajendrakumar, N.-C. Chang, A. Mohapatra, S. Uthaman, B.-I. Lee, W.-B. Tsai, I.-K. Park, A Lipophilic IR-780 Dye-Encapsulated Zwitterionic Polymer-Lipid

Micellar Nanoparticle for Enhanced Photothermal Therapy and NIR-Based Fluorescence Imaging in a Cervical Tumor Mouse Model., Int. J. Mol. Sci. 19 (2018). doi:10.3390/ijms19041189.

[133] M.S. Boshra, A.G. Almeldien, R.S. Eldin, A.A. Elberry, N.S. Abdelwahab, M.N. Salem, H. Rabea, M.E.A. Abdelrahim, Inhaled salbutamol from aerolizer and diskus at different inhalation flows, inhalation volume and number of inhalations in both healthy subjects and COPD patients., Exp. Lung Res. 45 (2019) 84–91. doi:10.1080/01902148.2019.1621408.

[134] M.S. Boshra, A.G. Almeldien, R. Salah Eldin, A.A. Elberry, N.S. Abdelwahab, M. Nabil Salem, H. Rabea, M.E.A. Abdelrahim, Total emitted dose of salbutamol sulphate at different inhalation flows and inhalation volumes through different types of dry powder inhalers, Exp. Lung Res. 44 (2018) 211–216. doi:10.1080/01902148.2018.1489015.

[135] M. Abadelah, H. Chrystyn, G. Bagherisadeghi, G. Abdalla, H. Larhrib, Study of the Emitted Dose After Two Separate Inhalations at Different Inhalation Flow Rates and Volumes and an Assessment of Aerodynamic Characteristics of Indacaterol Onbrez Breezhaler® 150 and 300 μg, AAPS PharmSciTech. 19 (2018) 251–261. doi:10.1208/s12249-017-0841-y.

[136] M. Semmler-Behnke, S. Takenaka, S. Fertsch, A. Wenk, J. Seitz, P. Mayer, G. Oberdörster, W.G. Kreyling, Efficient elimination of inhaled nanoparticles from the alveolar region: Evidence for interstitial uptake and subsequent reentrainment onto airways epithelium, Environ. Health Perspect. 115 (2007) 728–733. doi:10.1289/ehp.9685.

[137] B. del Rosal, I. Villa, D. Jaque, F. Sanz-Rodríguez, *In vivo* autofluorescence in the biological windows: the role of pigmentation, J. Biophotonics. 9 (2016) 1059–1067. doi:10.1002/jbio.201500271.

[138] A. Patti C., Zeidler-Erdely James M., M. Terence G., Y. Shih-Houng, E. Tracy J., H. Mary Ann, E. Aaron, Comparison of cell counting methods in rodent pulmonary toxicity studies: automated and manual protocols and considerations for experimental design, Inhal. Toxicol. 28 (2016) 410–420. doi:10.1080/08958378.2016.1189985.

[139] D.B. Warheit, M.A. Hartsky, M.S. Stefaniak, Comparative physiology of rodent pulmonary macrophages: in vitro functional responses., J. Appl. Physiol. 64 (1988) 1953–9. doi:10.1152/jappl.1988.64.5.1953.

[140] K. Sapru, P.K. Stotland, M.M. Stevenson, Quantitative and qualitative differences in

bronchoalveolar inflammatory cells in Pseudomonas aeruginosa-resistant and -susceptible mice., Clin. Exp. Immunol. 115 (1999) 103–9. doi:10.1046/j.1365-2249.1999.00762.x.

[141] R.E. Crowell, E. Heaphy, Y.E. Valdez, C. Mold, B.E. Lehnert, Alveolar and interstitial macrophage populations in the murine lung., Exp. Lung Res. 18 (1992) 435–46.

[142] M. Geiser, A.L. Serra, L.M. Cruz-Orive, M. Baumann, V.I. Hof, P. Gehr, Efficiency of airway macrophage recovery by bronchoalveolar lavage in hamsters: a stereological approach, Eur. Respir. J. 8 (1995) 1712–1718. doi:10.1183/09031936.95.08101712.

[143] J.L. Tan, W. Liu, C.M. Nelson, S. Raghavan, C.S. Chen, Simple Approach to Micropattern Cells on Common Culture Substrates by Tuning Substrate Wettability, Tissue Eng. 10 (2004) 865–872. doi:10.1089/1076327041348365.

[144] T. Rawal, L. Kremer, I. Halloum, S. Butani, Dry-Powder Inhaler Formulation of Rifampicin: An Improved Targeted Delivery System for Alveolar Tuberculosis, J. Aerosol Med. Pulm. Drug Deliv. 30 (2017) 388–398. doi:10.1089/jamp.2017.1379.

[145] X. Xu, Q. Xie, Y. Shen, G. Lu, H. Yao, Y. Chen, J. Zhou, Involvement of mannose receptor in the preventive effects of mannose in lipopolysaccharide-induced acute lung injury, Eur. J. Pharmacol. 641 (2010) 229–237. doi:10.1016/j.ejphar.2010.05.021.

[146] M. Chieppa, G. Bianchi, A. Doni, A. Del Prete, M. Sironi, G. Laskarin, P. Monti, L. Piemonti, A. Biondi, A. Mantovani, M. Introna, P. Allavena, Cross-Linking of the Mannose Receptor on Monocyte-Derived Dendritic Cells Activates an Anti-Inflammatory Immunosuppressive Program, J. Immunol. 171 (2003) 4552–4560. doi:10.4049/jimmunol.171.9.4552.

[147] J. Zhang, S.D. Tachado, N. Patel, J. Zhu, A. Imrich, P. Manfruelli, M. Cushion, T.B. Kinane, H. Koziel, Negative regulatory role of mannose receptors on human alveolar macrophage proinflammatory cytokine release in vitro, J. Leukoc. Biol. 78 (2005) 665–674. doi:10.1189/jlb.1204699.

[148] J. Ragusa, D. Gonzalez, S. Li, S. Noriega, M. Skotak, G. Larsen, Glucosamine/L-lactide copolymers as potential carriers for the development of a sustained rifampicin release system using Mycobacterium smegmatis as a tuberculosis model, Heliyon. 5 (2019) e01539. doi:10.1016/J.HELIYON.2019.E01539.

[149] A. Woods, A. Patel, D. Spina, Y. Riffo-Vasquez, A. Babin-Morgan, R.T.M. de Rosales, K. Sunassee, S. Clark, H. Collins, K. Bruce, L.A. Dailey, B. Forbes, In vivo biocompatibility, clearance, and biodistribution of albumin vehicles for pulmonary drug delivery, J. Control. Release. 210 (2015) 1–9. doi:10.1016/j.jconrel.2015.05.269.

[150] N.K. Dutta, P.B. Illei, C.A. Peloquin, M.L. Pinn, K.E. Mdluli, E.L. Nuermberger, J.H. Grosset, P.C. Karakousis, Rifapentine is not more active than rifampin against chronic tuberculosis in guinea pigs., Antimicrob. Agents Chemother. 56 (2012) 3726–31. doi:10.1128/AAC.00500-12.

[151] R. Nau, A. Wellmer, A. Soto, K. Koch, O. Schneider, H. Schmidt, J. Gerber, U. Michel, W. Brück, Rifampin Reduces Early Mortality in Experimental Streptococcus pneumoniae Meningitis , J. Infect. Dis. 179 (1999) 1557–1560. doi:10.1086/314760.

[152] J. Parkinson, An essay on the shaking palsy. 1817., J. Neuropsychiatry Clin. Neurosci. 14 (2002) 223–36; discussion 222.

[153] L. V Kalia, A.E. Lang, Parkinson's disease, Lancet. 6736 (2015) 1–17. doi:10.1016/S0140-6736(14)61393-3.

[154] S.H. Mehta, C.M. Tanner, Role of Neuroinflammation in Parkinson Disease: The Enigma Continues, Mayo Clin. Proc. 91 (2016) 1328–1330. doi:10.1016/j.mayocp.2016.08.010.

[155] C. Perier, M. Vila, Mitochondrial Biology and Parkinson's Disease, (2012) 1–19.

[156] K.R. Rekha, G.P. Selvakumar, Gene expression regulation of Bcl2 , Bax and cytochrome-C by geraniol on chronic MPTP / probenecid induced C57BL / 6 mice model of Parkinson ' s disease, Chem. Biol. Interact. 217 (2014) 57–66. doi:10.1016/j.cbi.2014.04.010.

[157] K.R. Rekha, G.P. Selvakumar, K. Santha, R. Inmozhi, Geraniol attenuates a -synuclein expression and neuromuscular impairment through increase dopamine content in MPTP intoxicated mice by dose dependent manner, Biochem. Biophys. Res. Commun. 440 (2013) 664–670. doi:10.1016/j.bbrc.2013.09.122.

[158] K.R. Rekha, G.P. Selvakumar, Geraniol Ameliorates the Motor Behavior and Neurotrophic Factors Inadequacy in MPTP-Induced Mice Model of Parkinson ' s Disease, (2013) 851–862. doi:10.1007/s12031-013-0074-9.

[159] B. Pavan, A. Dalpiaz, L. Marani, S. Beggiato, L. Ferraro, D. Canistro, M. Paolini, F. Vivarelli, M.C. Valerii, A. Comparone, L.D. De Fazio, E. Spisni, Geraniol pharmacokinetics, bioavailability and its multiple effects on the liver antioxidant and xenobiotic-metabolizing enzymes, Front. Pharmacol. 9 (2018) 1–14. doi:10.3389/fphar.2018.00018.

[160] L. De Fazio, E. Spisni, E. Cavazza, A. Strillacci, M. Candela, M. Centanni, C. Ricci, F. Rizzello, M. Campieri, M.C. Valerii, Dietary Geraniol by Oral or Enema Administration Strongly Reduces Dysbiosis and Systemic Inflammation in Dextran

Sulfate Sodium-Treated Mice., Front. Pharmacol. 7 (2016) 38. doi:10.3389/fphar.2016.00038.

[161] M. Cho, I. So, J.N. Chun, J.H. Jeon, The antitumor effects of geraniol: Modulation of cancer hallmark pathways (Review), Int. J. Oncol. 48 (2016) 1772–1782. doi:10.3892/ijo.2016.3427.

[162] F. Sonvico, A. Clementino, F. Buttini, G. Colombo, S. Pescina, S.S. Guterres, A.R. Pohlmann, S. Nicoli, Surface-modified nanocarriers for nose-to-brain delivery: From bioadhesion to targeting, Pharmaceutics. 10 (2018) 1–34. doi:10.3390/pharmaceutics10010034.

[163] H. Mortiboys, R. Furmston, G. Bronstad, J. Aasly, C. Elliott, O. Bandmann, UDCA exerts beneficial effect on mitochondrial dysfunction in LRRK2(G2019S) carriers and in vivo., Neurology. 85 (2015) 846–52. doi:10.1212/WNL.0000000000001905.

[164] H. Mortiboys, J. Aasly, O. Bandmann, Ursocholanic acid rescues mitochondrial function in common forms of familial Parkinson's disease, Brain. 136 (2013) 3038–3050. doi:10.1093/brain/awt224.

[165] O.H. Lowry, N.J. Rosebrough, A.L. Farr, R.J. Randall, Protein measurement with the Folin phenol reagent., J. Biol. Chem. 193 (1951) 265–75. doi:10.1016/0922-338X(96)89160-4.

[166] M.P. van den Berg, S.G. Romeijn, J.C. Verhoef, F.W.H.M. Merkus, Serial cerebrospinal fluid sampling in a rat model to study drug uptake from the nasal cavity., J. Neurosci. Methods. 116 (2002) 99–107. http://www.ncbi.nlm.nih.gov/pubmed/12007987 (accessed July 5, 2019).

[167] A. Dalpiaz, L. Ferraro, D. Perrone, E. Leo, V. Iannuccelli, B. Pavan, G. Paganetto, S. Beggiato, S. Scalia, Brain uptake of a zidovudine prodrug after nasal administration of solid lipid microparticles, Mol. Pharm. 11 (2014) 1550–1561. doi:10.1021/mp400735c.

[168] K. Felgenhauer, Protein size and cerebrospinal fluid composition., Klin. Wochenschr. 52 (1974) 1158–64.

[169] A. Madu, C. Cioffe, U. Mian, M. Burroughs, E. Tuomanen, M. Mayers, E. Schwartz, M. Miller, Pharmacokinetics of fluconazole in cerebrospinal fluid and serum of rabbits: validation of an animal model used to measure drug concentrations in cerebrospinal fluid., Antimicrob. Agents Chemother. 38 (1994) 2111–5. doi:10.1128/aac.38.9.2111.

[170] A. Dalpiaz, G. Paganetto, B. Pavan, M. Fogagnolo, A. Medici, S. Beggiato, D. Perrone, Zidovudine and Ursodeoxycholic Acid Conjugation: Design of a New Prodrug Potentially Able To Bypass the Active Efflux Transport Systems of the Central

Nervous System, Mol. Pharm. 9 (2012) 957–968. doi:10.1021/mp200565g.

[171] G.J. Parry, C.M.P. Rodrigues, M.M. Aranha, S.J. Hilbert, C. Davey, P. Kelkar, W.C. Low, C.J. Steer, Safety, Tolerability, and Cerebrospinal Fluid Penetration of Ursodeoxycholic Acid in Patients With Amyotrophic Lateral Sclerosis, Clin. Neuropharmacol. 33 (2010) 17–21. doi:10.1097/WNF.0b013e3181c47569.

[172] M.C. Bonferoni, L. Ferraro, B. Pavan, S. Beggiato, E. Cavalieri, P. Giunchedi, A. Dalpiaz, Uptake in the central nervous system of geraniol oil encapsulated in chitosan oleate following nasal and oral administration, Pharmaceutics. 11 (2019). doi:10.3390/pharmaceutics11030106.

[173] Y. Yang, H. Aloysius, D. Inoyama, Y. Chen, L. Hu, Enzyme-mediated hydrolytic activation of prodrugs, Acta Pharm. Sin. B. 1 (2011) 143–159. doi:10.1016/J.APSB.2011.08.001.

[174] B. Pavan, A. Dalpiaz, Prodrugs and Endogenous Transporters: Are They Suitable Tools for Drug Targeting into the Central Nervous System?, Curr. Pharm. Des. 17 (2011) 3560–3576. doi:10.2174/138161211798194486.

[175] B. Pavan, G. Paganetto, D. Rossi, A. Dalpiaz, Multidrug resistance in cancer or inefficacy of neuroactive agents: Innovative strategies to inhibit or circumvent the active efflux transporters selectively, Drug Discov. Today. 19 (2014) 1563–1571. doi:10.1016/j.drudis.2014.06.004.

[176] Y. Jin, L. Xing, Y. Tian, M. Li, C. Gao, L. Du, J. Dong, H. Chen, Self-assembled drug delivery systems. Part 4. In vitro/in vivo studies of the self-assemblies of cholesteryl-phosphonyl zidovudine., Int. J. Pharm. 381 (2009) 40–8. doi:10.1016/j.ijpharm.2009.07.024.

[177] M.H. Aburahma, S.M. Badr-Eldin, Compritol 888 ATO: a multifunctional lipid excipient in drug delivery systems and nanopharmaceuticals, Expert Opin. Drug Deliv. 11 (2014) 1865–1883. doi:10.1007/s12598-013-0015-3.

[178] M.J. Gomes, C. Fernandes, S. Martins, F. Borges, B. Sarmento, Tailoring Lipid and Polymeric Nanoparticles as siRNA Carriers towards the Blood-Brain Barrier – from Targeting to Safe Administration, J. Neuroimmune Pharmacol. 12 (2017) 107–119. doi:10.1007/s11481-016-9685-6.

[179] W. Abdelwahed, G. Degobert, S. Stainmesse, H. Fessi, Freeze-drying of nanoparticles: Formulation, process and storage considerations, Adv. Drug Deliv. Rev. 58 (2006) 1688–1713. doi:10.1016/j.addr.2006.09.017.

[180] T. Musumeci, R. Pellitteri, M. Spatuzza, G. Puglisi, Nose-to-brain delivery: Evaluation

of polymeric nanoparticles on olfactory ensheathing cells uptake, J. Pharm. Sci. 103 (2014) 628–635. doi:10.1002/jps.23836.

[181] O. Gartziandia, S.P. Egusquiaguirre, J. Bianco, J.L. Pedraz, M. Igartua, R.M. Hernandez, V. Préat, A. Beloqui, Nanoparticle transport across in vitro olfactory cell monolayers, Int. J. Pharm. 499 (2016) 81–89. doi:10.1016/j.ijpharm.2015.12.046.

[182] Y.M. Gabal, A.O. Kamel, O.A. Sammour, A.H. Elshafeey, Effect of surface charge on the brain delivery of nanostructured lipid carriers in situ gels via the nasal route, Int. J. Pharm. 473 (2014) 442–457. doi:10.1016/j.ijpharm.2014.07.025.

[183] J.M. Barichello, M. Morishita, K. Takayama, T. Nagai, Encapsulation of Hydrophilic and Lipophilic Drugs in PLGA Nanoparticles by the Nanoprecipitation Method, Drug Dev. Ind. Pharm. 25 (1999) 471–476. doi:10.1081/DDC-100102197.

[184] P. Ghasemiyeh, S. Mohammadi-Samani, Solid lipid nanoparticles and nanostructured lipid carriers as novel drug delivery systems: applications, advantages and disadvantages, Res. Pharm. Sci. 13 (2018) 288. doi:10.4103/1735-5362.235156.

[185] A. zur Mühlen, C. Schwarz, W. Mehnert, Solid lipid nanoparticles (SLN) for controlled drug delivery – Drug release and release mechanism, Eur. J. Pharm. Biopharm. 45 (1998) 149–155. doi:10.1016/S0939-6411(97)00150-1.

[186] T. Higuchi, K.A. Connors, Phase solubility techniques, Adv. Anal. Chem. Instrum. 4 (1965) 117–212.

[187] A. Figueiras, R.A. Carvalho, L. Ribeiro, J.J. Torres-Labandeira, F.J.B. Veiga, Solid-state characterization and dissolution profiles of the inclusion complexes of omeprazole with native and chemically modified β-cyclodextrin, Eur. J. Pharm. Biopharm. 67 (2007) 531–539. doi:10.1016/J.EJPB.2007.03.005.

[188] S.C.-S. Hu, Y.-C. Lai, C.-L. Lin, W.-S. Tzeng, F.-L. Yen, Inclusion complex of saikosaponin-d with hydroxypropyl-β-cyclodextrin: Improved physicochemical properties and anti-skin cancer activity, Phytomedicine. 57 (2019) 174–182. doi:10.1016/J.PHYMED.2018.11.012.

[189] S. Gao, J.-Y. Jiang, Y.-Y. Liu, Y. Fu, L.-X. Zhao, C.-Y. Li, F. Ye, Enhanced Solubility, Stability, and Herbicidal Activity of the Herbicide Diuron by Complex Formation with β-Cyclodextrin, Polymers (Basel). 11 (2019) 1396. doi:10.3390/polym11091396.

[190] M. Kfoury, D. Landy, S. Ruellan, L. Auezova, H. Greige-Gerges, S. Fourmentin, Determination of formation constants and structural characterization of cyclodextrin inclusion complexes with two phenolic isomers: Carvacrol and thymol, Beilstein J.

Org. Chem. 12 (2016) 29–42. doi:10.3762/bjoc.12.5.

[191] T. Loftsson, D. Hreinsdóttir, M. Másson, Evaluation of cyclodextrin solubilization of drugs, Int. J. Pharm. 302 (2005) 18–28. doi:10.1016/j.ijpharm.2005.05.042.

[192] T. Loftsson, M.E. Brewster, Cyclodextrins as Functional Excipients: Methods to Enhance Complexation Efficiency, J. Pharm. Sci. 101 (2012) 3019–3032. doi:10.1002/JPS.23077.

[193] H. Viernstein, P. Weiss-Greiler, P. Wolschann, Solubility enhancement of low soluble biologically active compounds--temperature and cosolvent dependent inclusion complexation., Int. J. Pharm. 256 (2003) 85–94.

[194] E.M.M. Del Valle, Cyclodextrins and their uses: A review, Process Biochem. 39 (2004) 1033–1046. doi:10.1016/S0032-9592(03)00258-9.

[195] M.P. di Cagno, The Potential of Cyclodextrins as Novel Active Pharmaceutical Ingredients: A Short Overview., Molecules. 22 (2016). doi:10.3390/molecules22010001.

[196] Q. Geng, T. Li, X. Wang, W. Chu, M. Cai, J. Xie, H. Ni, The mechanism of bensulfuron-methyl complexation with β-cyclodextrin and 2-hydroxypropyl-β-cyclodextrin and effect on soil adsorption and bio-activity, Sci. Rep. 9 (2019) 1882. doi:10.1038/s41598-018-38234-7.

[197] P. Saokham, C. Muankaew, P. Jansook, T. Loftsson, Solubility of cyclodextrins and drug/cyclodextrin complexes, Molecules. 23 (2018) 1–15. doi:10.3390/molecules23051161.

[198] F. Tao, L.E. Hill, Y. Peng, C.L. Gomes, Synthesis and characterization of β-cyclodextrin inclusion complexes of thymol and thyme oil for antimicrobial delivery applications, LWT - Food Sci. Technol. 59 (2014) 247–255. doi:10.1016/J.LWT.2014.05.037.

[199] K.. Waleczek, H.M.C. Marques, B. Hempel, P.. Schmidt, Phase solubility studies of pure (−)-α-bisabolol and camomile essential oil with β-cyclodextrin, Eur. J. Pharm. Biopharm. 55 (2003) 247–251. doi:10.1016/S0939-6411(02)00166-2.

[200] P. Jansook, N. Ogawa, T. Loftsson, Cyclodextrins: structure, physicochemical properties and pharmaceutical applications, Int. J. Pharm. 535 (2018) 272–284. doi:10.1016/j.ijpharm.2017.11.018.

[201] A. Magnusdottir, M. Másson, T. Loftsson, Self association and cyclodextrin solubilization of NSAIDs, J. Incl. Phenom. 44 (2002) 213–218. doi:10.1023/A:1023079322024.

[202] E.-J. Wang, Z.-X. Lian, J. Cai, The crystal structure of the 1:1 inclusion complex of β-cyclodextrin with benzamide, Carbohydr. Res. 342 (2007) 767–771. doi:10.1016/J.CARRES.2006.12.004.

[203] J.C. de Miranda, T.E.A. Martins, F. Veiga, H.G. Ferraz, Cyclodextrins and ternary complexes: Technology to improve solubility of poorly soluble drugs, Brazilian J. Pharm. Sci. 47 (2011) 665–681. doi:10.1590/S1984-82502011000400003.

[204] F. Kayaci, H.S. Sen, E. Durgun, T. Uyar, Functional electrospun polymeric nanofibers incorporating geraniol – cyclodextrin inclusion complexes : High thermal stability and enhanced durability of geraniol Food Research International Functional electrospun polymeric nano fi bers incorporating gera, FRIN. 62 (2014) 424–431. doi:10.1016/j.foodres.2014.03.033.

[205] K. Feng, P. Wen, H. Yang, N. Li, W.Y. Lou, M.H. Zong, H. Wu, Enhancement of the antimicrobial activity of cinnamon essential oil-loaded electrospun nanofilm by the incorporation of lysozyme, RSC Adv. 7 (2017) 1572–1580. doi:10.1039/C6RA25977D.

[206] S. Nascimento, A. Araújo, R. Brito, M. Serafini, P. Menezes, J. DeSantana, W. Júnior, P. Alves, A. Blank, R. Oliveira, A. Oliveira, R. Albuquerque-Júnior, J. Almeida, L. Quintans-Júnior, Cyclodextrin-Complexed Ocimum basilicum Leaves Essential Oil Increases Fos Protein Expression in the Central Nervous System and Produce an Antihyperalgesic Effect in Animal Models for Fibromyalgia, Int. J. Mol. Sci. 16 (2014) 547–563. doi:10.3390/ijms16010547.

[207] F.B. T. Pessine, A. Calderini, G. L., Review: Cyclodextrin Inclusion Complexes Probed by NMR Techniques, Magn. Reson. Spectrosc. 1 (2012). doi:10.5772/32029.

[208] M. Chen, G. Diao, E. Zhang, Study of inclusion complex of β-cyclodextrin and nitrobenzene, Chemosphere. 63 (2006) 522–529. doi:10.1016/j.chemosphere.2005.08.033.

[209] D. Greatbanks, R. Pickford, Cyclodextrins as chiral complexing agents in water, and their application to optical purity measurements, Magn. Reson. Chem. 25 (1987) 208–215. doi:10.1002/mrc.1260250306.

[210] H.M.C. Marques, A review on cyclodextrin encapsulation of essential oils and volatiles, Flavour Fragr. J. 25 (2010) 313–326. doi:10.1002/ffj.2019.

[211] Z. Patel, B. Patel, S. Patel, C. Pardeshi, Nose to brain targeted drug delivery bypassing the blood-brain barrier: An overview, Drug Invent. Today. 4 (2012) 610–615.

[212] T. Loftsson, A. Magnúsdóttir, M. Másson, J.F. Sigurjónsdóttir, Self-association and

cyclodextrin solubilization of drugs, J. Pharm. Sci. 91 (2002) 2307–2316. doi:10.1002/jps.10226.

[213] A. Ryzhakov, T. Do Thi, J. Stappaerts, L. Bertoletti, K. Kimpe, A.R. Sá Couto, P. Saokham, G. Van den Mooter, P. Augustijns, G.W. Somsen, S. Kurkov, S. Inghelbrecht, A. Arien, M.I. Jimidar, K. Schrijnemakers, T. Loftsson, Self-Assembly of Cyclodextrins and Their Complexes in Aqueous Solutions, J. Pharm. Sci. 105 (2016) 2556–2569. doi:10.1016/j.xphs.2016.01.019.

[214] N.G.M. Schipper, W.A.J.J. Hermens, S.G. Romeyn, J. Verhoef, F.W.H.M. Merkus, Nasal absorption of 17-beta-estradiol and progesterone from a dimethyl-cyclodextrin inclusion formulation in rats, Int. J. Pharm. 64 (1990) 61–66. doi:10.1016/0378-5173(90)90179-8.

[215] H.M. Cabral Marques, J. Hadgraft, I.W. Kellaway, G. Taylor, Studies of cyclodextrin inclusion complexes. III. The pulmonary absorption of β-, DM-β- and HP-β-cyclodextrins in rabbits, Int. J. Pharm. 77 (1991) 297–302. doi:10.1016/0378-5173(91)90330-Q.

[216] G. González-Gaitano, P. Rodríguez, J.R. Isasi, M. Fuentes, G. Tardajos, M. Sánchez, The aggregation of cyclodextrins as studied by photon correlation spectroscopy, in: J. Incl. Phenom., 2002: pp. 101–105. doi:10.1023/A:1023065823358.